THERMAL CONDUCTIVITY OF METAL OXIDE NANOFLUIDS

A Thesis
Presented to
The Academic Faculty

by

Michael Peter Beck

In Partial Fulfillment
of the Requirements for the Degree
Doctor of Philosophy in the
School of Chemical and Biomolecular Engineering

Georgia Institute of Technology
December 2008

THERMAL CONDUCTIVITY OF METAL OXIDE NANOFLUIDS

Approved by:

Dr. Amyn S. Teja, Advisor
School of Chemical and Biomolecular Engineering
Georgia Institute of Technology

Dr. Carson Meredith
School of Chemical and Biomolecular Engineering
Georgia Institute of Technology

Dr. Said I. Abdel-Khalik
School of Mechanical Engineering
Georgia Institute of Technology

Dr. Sankar Nair
School of Chemical and Biomolecular Engineering
Georgia Institute of Technology

Dr. Ganesh Skandan
CEO
NEI Corporation

Date Approved: August 12, 2008

Dedicated to the memory of

my mother

Linda S. Beck
(August 24, 1947 – October 25, 2000)

ACKNOWLEDGEMENTS

I would like to thank all of the people that have helped me throughout my studies here at Georgia Tech. First, I would like to acknowledge my advisor Dr. Amyn Teja for his support and guidance in my research. I would also like to acknowledge my committee members, Dr. Nair, Dr. Meredith, Dr. Abdel-Khalik, and Dr. Skandan for their help and advice over the years.

I would also like to thank the past and present members of the Teja research group. Dr. Sun, Kerry, Ibrahim, Shutaro, Izumi, Chunbao, Nan, James, Anu, Pei Yoong, Angel, Yanhui, Pramod, and Nelson have all been very helpful and have been great friends. Dr. Sun taught me how to perform my experiments and was instrumental in the initial stages of my research. I am grateful to Chunbao, Pei Yoong, Yanhui, and Pramod who spent their time helping me through various stages of my work.

I would also like to thank Chris Gill of the Jones group for his help with the TEM imaging of my samples and Jason Ward of the Koros group for his help with surface area measurements. I appreciate the efforts of Brad and Jeff in the ChBE machine shop and the technicians in the Mechanical Engineering electronics shop for their help during the construction of my measurement apparatus.

I would also like to acknowledge my family for all of the encouragement and support they have provided throughout my education. Most importantly, I would like to thank my wife, Nan. Her love and support have helped me through many obstacles and have allowed me to accomplish my goals. I would not be where I am today without her.

TABLE OF CONTENTS

LIST OF TABLES

LIST OF FIGURES

Page

LIST OF SYMBOLS

a	radius of dispersed spheres
A	heat transfer area
A_1	adjustable parameter in Eq. 6.4
b	inside diameter of cell
b	radius of spherical volume (Eq. 5.8)
B	radiation parameter in Eq. 3.12
c	cell constant in Eq. 3.1
C_1	proportionality constant in Eq. 5.20
d	diameter of particle
d_f	diameter of fluid molecule
D	diffusivity
D	pipe diameter (Eq. 1.2)
f	empirical factor in Eq. 5.16
g_v	roots of J_0
G	temperature gradient
h	heat transfer coefficient
h	thickness of ordered liquid molecular layer (Eq. 5.27)
H	overall heat transfer coefficient
I	electric current
J_0	zero-order Bessel function of the first kind
k	thermal conductivity
k_1	thermal conductivity of liquid
k_2	thermal conductivity of solid

k_B	Boltzmann constant
k_{bulk}	thermal conductivity of bulk solid
k_{eff}	effective thermal conductivity of dispersion
k_{layer}	thermal conductivity of ordered liquid molecules
L	wire length
L	pipe length (Eq. 1.2)
m	mass
n	empirical shape factor in Eq. 5.10
n_S	number of spheres
q	heat dissipated per unit length
P_1	one dimensional porosity
Q	heat flow
r	radial distance from heat source
r_i	inner radius of capillary
r_o	outer radius of capillary
R_1, R_2	electric resistance of fixed resistors
R_B	interfacial thermal resistance (Kapitza resistance)
R_D	electric resistance of decade resistor
R_W	electric resistance of wire
t	time
T	temperature
T_{id}	ideal temperature of wire
V	electric potential across Wheatstone bridge
V	electric potential (Eq. 3.2)
V	specific volume (Eq. 2.1)

V_S	source electric potential
Y_0	zero-order Bessel function of the second kind

Greek Symbols

α	ratio of solid to liquid thermal conductivity
α	thermal diffusivity (Chapter 3)
γ	exponent of Euler's constant
ε	constant related to Kapitza resistance in Eq. 5.20
κ	temperature coefficient of mercury resistivity
μ	viscosity
μ_b	viscosity of fluid at bulk temperature
μ_0	viscosity of fluid at wall temperature
ρ	density
σ	standard deviation of P_1
τ	relaxation time constant
ϕ	particle volume fraction
ψ	sphericity

Subscripts

G	borosilicate glass
Hg	mercury

SUMMARY

The focus of this work is on nanofluids containing metal oxides. The specific goals were the determination of the effects of temperature and particle size on the thermal conductivity of nanofluids, the elucidation of the mechanism of conduction, and the development of a predictive thermal conductivity model.

Thermal conductivity measurements were performed with a liquid metal transient hot wire apparatus, which made possible measurements of electrically conducting fluids at elevated temperature. The nanofluid samples consisted of either alumina, titania, or ceria particles dispersed in deionized water, ethylene glycol, or a mixture of the two. Thermal conductivity measurements were performed at room temperature and at other temperatures up to 422 K that is over the largest temperature range that has been hitherto reported in the literature. Additionally, measurements were performed on nanofluids containing seven sizes of alumina particles with average diameters ranging from 8 to 282 nm, which is the largest number of sizes than previously considered.

The results of the thermal conductivity measurements at elevated temperatures revealed that the thermal conductivity relationship with temperature mimics the temperature relationship for the base liquid. The results of the thermal conductivity measurements of nanofluids containing different sizes of particles revealed that the addition of the smaller nanoparticles yielded lower thermal conductivity. The thermal conductivity measurements of dispersions containing larger particles (> 50 nm) yielded values that were well represented by predictions from the volume fraction – weighted geometric mean, which display agreement with measurements than predictions from

theoretical models for solid – liquid dispersions. These results also suggest that the thermal conductivity of the solid nanoparticles is less than the thermal conductivity of the bulk solid due to phonon scattering at the solid – liquid interface.

A predictive model has been developed for the thermal conductivity of nanofluids containing alumina. The model incorporates the particle size dependence of the thermal conductivity of solids in the volume fraction – weighted geometric mean. The model was fit to the experimental data for aqueous nanofluids containing alumina by adjusting a single parameter. The resulting model was capable of predicting the thermal conductivity of nanofluids containing ethylene glycol and alumina at various temperatures and containing various particle sizes from this work (within 2.3 %) and from the literature (within 5.0 %). Lastly, the model was used to evaluate the consistency of published data on the thermal conductivity of nanofluids.

CHAPTER 1

INTRODUCTION

The advent of high heat flow processes has created significant demand for new technologies to enhance heat transfer. For example, microprocessors have continually become smaller and more powerful, and as a result heat flow demands have steadily increased over time leading to new challenges in thermal management. Furthermore, there is increasing interest in improving the efficiency of existing heat transfer processes. An example is in automotive systems where improved heat transfer could lead to smaller heat exchangers for cooling resulting in reduced weight of the vehicle.

Many methods are available to improve heat transfer in processes. The flow of heat in a process can be calculated using,

$$Q = hA\Delta T \tag{1.1}$$

where Q is the heat flow, h is the heat transfer coefficient, A is the heat transfer area, and ΔT is the temperature difference that results in heat flow [1]. We can see from this equation that increased heat transfer can be achieved by:

(i) increasing ΔT

(ii) increasing A

(iii) increasing h

A greater temperature difference ΔT can lead to increased the heat flow, but ΔT is often limited by process or materials constraints. For example, the maximum temperature in a nuclear reactor must be kept below a certain value to avoid runaway reactions and meltdown. Therefore, increased ΔT can only be achieved by decreasing the

the temperature of the coolant. However, this would reduce the rate of the nuclear reaction and decrease the efficiency of the process.

Maximizing the heat transfer area A is a common strategy to improve heat transfer, and many heat exchangers such as radiators and plate-and-frame heat exchangers are designed to maximize the heat transfer area [2]. However, this strategy cannot be employed in microprocessors and microelectromechanical systems (MEMS) because the area can not be increased. In aerospace and automotive systems, increasing the heat transfer area can only be achieved by increasing the size of the heat exchanger which can lead to unwanted increases in weight.

Heat transfer improvements can also be achieved by increasing the heat transfer coefficient h either by using more efficient heat transfer methods, or by improving the transport properties of the heat transfer material. For example, heat transfer systems which employ forced convection of a gas exhibit a greater heat transfer coefficient than systems which employ free convection of a gas. Alternatively, the heat transfer coefficient can be increased by enhancing the properties of the coolant for a given method of heat transfer. Additives are often added to liquid coolants to improve specific properties. For example, glycols are added to water to depress its freezing point and to increase its boiling point. The heat transfer coefficient can be improved via the addition of solid particles to the liquid coolant. In the case of nanosized particles, the resulting dispersion is known as a nanofluid [3]. Xuan and Li [4] studied the forced convective heat transfer of an aqueous nanofluid containing 2 % (v/v) copper nanoparticles in a horizontal tube and observed a 39 % increase in heat transfer coefficient over that of the pure coolant. Similarly, Wen and Ding [5] performed a pool boiling heat transfer

experiment with an aqueous nanofluid containing 1.25 % (v/v) alumina nanoparticles on a polished stainless steel surface and observed a 40 % enhancement of the heat transfer coefficient compared to that of pure water. Based on these results, the addition of nanoparticles to a coolant appears to significantly enhance the heat transfer coefficient.

The relationship between the heat transfer coefficient and transport and thermodynamic properties of the coolant can be ascertained from heat transfer correlations. For example, in laminar flow through a pipe, the heat transfer coefficient is obtained from the Nusselt number *Nu* via the Sieder and Tate correlation [1],

$$Nu = \frac{hD}{k} = 1.86\left(\mathrm{Re}\,\mathrm{Pr}\frac{D}{L}\right)^{1/3}\left(\frac{\mu_b}{\mu_0}\right)^{0.14} \tag{1.2}$$

where D is the diameter of the pipe, k is the thermal conductivity of the fluid, Re is the Reynolds number, Pr is the Prandtl number, L is the length of the pipe, and μ_b and μ_0 are the viscosities of the fluid at the bulk temperature and the wall temperature, respectively. Equation 1.2 shows the relationship between the heat transfer coefficient and the thermal conductivity of the coolant. Increases in thermal conductivity therefore relate directly to increases in the heat transfer coefficient. It is not surprising therefore that nanofluids exhibit enhanced heat transfer since they also exhibit enhanced thermal conductivity [6].

The thermal conductivity of a liquid coolant can be increased with the addition of a more thermally conductive liquid or with the addition of solids, which are inherently more thermally conductive than liquids. Whereas a highly thermally conductive liquid, such as water, has a thermal conductivity that is 4 – 6 times greater than that of a less conductive liquid, solid thermal conductivity can be as much as three orders of magnitude

greater than liquid thermal conductivity. Thus, much research has been dedicated to nanofluids containing solid nanoparticles [6].

The thermal conductivities of nanofluids containing solid particles are generally greater than values predicted by theories of transport in heterogeneous materials. Existing models predict no more than 6 % enhancement of the thermal conductivity of poly (α-olefin) oil containing dispersed 1 % carbon nanotubes. However, Choi et al. [7] observed that the thermal conductivity of this nanofluid was 150 % greater than that of the oil alone. Thermal conductivities for a variety of nanofluids are discussed in chapter 2, and it can be seen that many of these nanofluids exhibit significant thermal conductivity enhancement. However, most of the studies are limited to nanofluids containing a single size of nanoparticles at room temperature [6]. The few studies focusing on the effect of temperature on the thermal conductivity of nanofluids have produced seemingly conflicting results. Some have observed increasing thermal conductivity with increasing temperature [8, 9], while others have reported the opposite [10, 11]. Similar discrepancies have arisen as to the effect of particle size on the thermal conductivity of nanofluids [12, 13]. Based on these data, several theories have been proposed to explain the anomalous thermal conductivity behavior. The most prevalent theories involve the Brownian motion of particles to create a microconvective effect, or the ordering of liquid molecules at the solid interface to enhance conduction through those molecules, or the clustering of nanoparticles to form pathways of lower thermal resistance [14].

Semi-empirical thermal conductivity models have been developed based on these mechanisms as detailed in Chapter 3. These models are effective in fitting some of the

thermal conductivity data from the literature. However, they are ineffective in predicting the general behavior of the thermal conductivity of nanofluids. Thus, the mechanisms for thermal conduction in nanofluids remain to be resolved. Furthermore, it remains unclear how parameters such as temperature and particle size affect the thermal conductivity of nanofluids.

This work focuses on the effects of various parameters on the thermal conductivity of nanofluids and the development of a new model for predictive purposes. A systematic experimental study has been performed in which thermal conductivity has been measured for nanofluids containing metal oxides over a wider temperature range than previously studied, and for more particle sizes than previously considered. The measurements have been performed using a liquid metal transient hot wire method described in Chapter 3. The resulting data are presented in Chapter 4 and are used to resolve discrepancies in the temperature dependence of the thermal conductivity and particle size dependence of the thermal conductivity.

The data are also used to rigorously test the prediction of published models for the thermal conductivity of nanofluids and thereby identify (or eliminate) mechanisms for heat transport in these fluids. Based on these tests, a new model for thermal transport in nanofluids is proposed and is described in Chapter 6. The predictive capabilities of the model are outlined, so that new nanofluids and/or new thermal management options can be explained for different applications that require enhanced heat transfer fluids.

CHAPTER 2

BACKGROUND - EXPERIMENTAL

Nanofluids can be considered to be composite materials consisting of a solid discrete phase and a liquid continuous phase, and the behavior of their thermal conductivity can best be understood by considering the thermal conductivity of the individual phases. This chapter provides a review of thermal conductivity data for liquids, solids, and solid – liquid dispersions.

2.1 Thermal Conductivity of Liquids

The thermal conductivity of liquids is generally greater than that of gases but much less than that of solids. Values range from 0.06 W m^{-1} K^{-1} for fluorocarbons (FC-72 from 3M) to 0.6 W m^{-1} K^{-1} for water. Associating liquids such as water and ethylene glycol exhibit greater thermal conductivity than nonpolar liquids such as hexane. Table 2.1 displays the thermal conductivity of several solids and liquids that have been used in nanofluid investigations.

Heat conduction occurs in liquids through the interactions between vibrating molecules in a temperature gradient. As liquid molecules vibrate around their equilibrium positions, their force fields overlap with their nearest neighbors. The molecules at a greater temperature vibrate at a higher frequency and transfer heat through these vibrationss to the molecules vibrating at a lower frequency due to their lower temperature [15]. Liquids such as water, ammonia, or glycols have greater thermal conductivity than non-polar liquids such as alkanes because of the stronger intermolecular force between polar molecules [16].

Table 2.1 Thermal conductivity of some solids and liquids at 25 ºC

Material	Thermal Conductivity (W m^{-1} K^{-1})
Carbon Nanotubes	2000 [7]
Diamond	900 – 2320 [17]
SiC	490 [2]
Silver	424 [2]
Copper	398 [2]
Gold	315 [2]
Aluminum	273 [2]
Graphite	119 – 165 [7]
Iron	80 [2]
Cupric Oxide	77 [18]
Alumina	40 [19]
Zinc Oxide	29 [13]
Carbon Nanofibers	13 [20]
Titania	8.4 [13]
Iron (II, III) Oxide	7.0 [21]
Bismuth Telluride	5.0 [22]
Carbon (amorphous)	1.59 [17]
Silica	1.34 [2]
$C_{60} – C_{70}$ (Fullerenes)	0.4 [18]
Water	0.608 [23]
Glycerol	0.285 [2]
Ethylene Glycol	0.257 [2]
Ethanol	0.172 [2]
Decene	0.14 [24]
Toluene	0.133 [2]
Perfluorotriethylamine	0.13 [25]
Hexane	0.126 [26]
Poly (α-olefin) oil	0.117 [27]
Perfluorohexane (FC-72)	0.057 [10]

2.1.1 Temperature and Pressure Dependence

The thermal conductivity of liquids generally exhibits a linearly decreasing relationship with increasing temperature due to thermal expansion. As the density decreases, the thermal conductivity also decreases. This is demonstrated by the following relationship between the temperature coefficient of thermal conductivity and the coefficient of thermal expansion,

$$\frac{1}{k}\left(\frac{\partial k}{\partial T}\right) \propto -\frac{1}{V}\left(\frac{\partial V}{\partial T}\right) = \frac{1}{\rho}\left(\frac{\partial \rho}{\partial T}\right) \tag{2.1}$$

Thus, the relative change of thermal conductivity with temperature is directly proportional to the relative change of density [28]. The temperature dependence is relatively weak when compared to that for the viscosity. For example, the thermal conductivity of hexane decreases 22.6 % when heated from 235 K to 335 K at atmospheric pressure, but the viscosity decreases 68.7 % for the same temperature change [26]. The difference arises from kinetic theory, which yields an exponential decreasing of viscosity with increasing temperature. The pressure has an even weaker effect on the thermal conductivity of liquids. The thermal conductivity of hexane increases just 4.8 % when pressurized from 1 to 101 bar at 298 K [26]. The pressure dependence also arises from the relationship between thermal conductivity and density. These temperature and pressure trends are illustrated in Figure 2.1, which displays a corresponding – states plot for the reduced thermal conductivity of liquids. Note the relationship between the thermal conductivity and temperature is linear except near the critical point. The plot was developed from the thermal conductivity of several monatomic liquids, and is often used to estimate the thermal conductivity of many polyatomic liquids as well [1].

However, this plot is insufficient when estimating the thermal conductivity of polar or associating liquids such as water and ethylene glycol. For these liquids, there may exist a maximum on the thermal conductivity versus temperature curve, as is the case for water and glycols [23, 29]. This phenomenon for water and other associating liquids is due to changes in the local structure of the hydrogen bonding network with changes in temperature. At lower temperatures, a portion of the energy being transferred becomes stored in the hydrogen bonds as they form a network. With increasing temperature, less energy is captured by the structural changes of the hydrogen bonding network leading to increased thermal conductivity [30]. This phenomenon competes with the typical relationship between thermal conductivity and temperature, where the thermal conductivity continually decreases with increasing temperature due to thermal expansion. Figure 2.2 displays the effect of temperature and pressure on the thermal conductivity water. The maximum thermal conductivity occurs at approximately 404 K for saturated water.

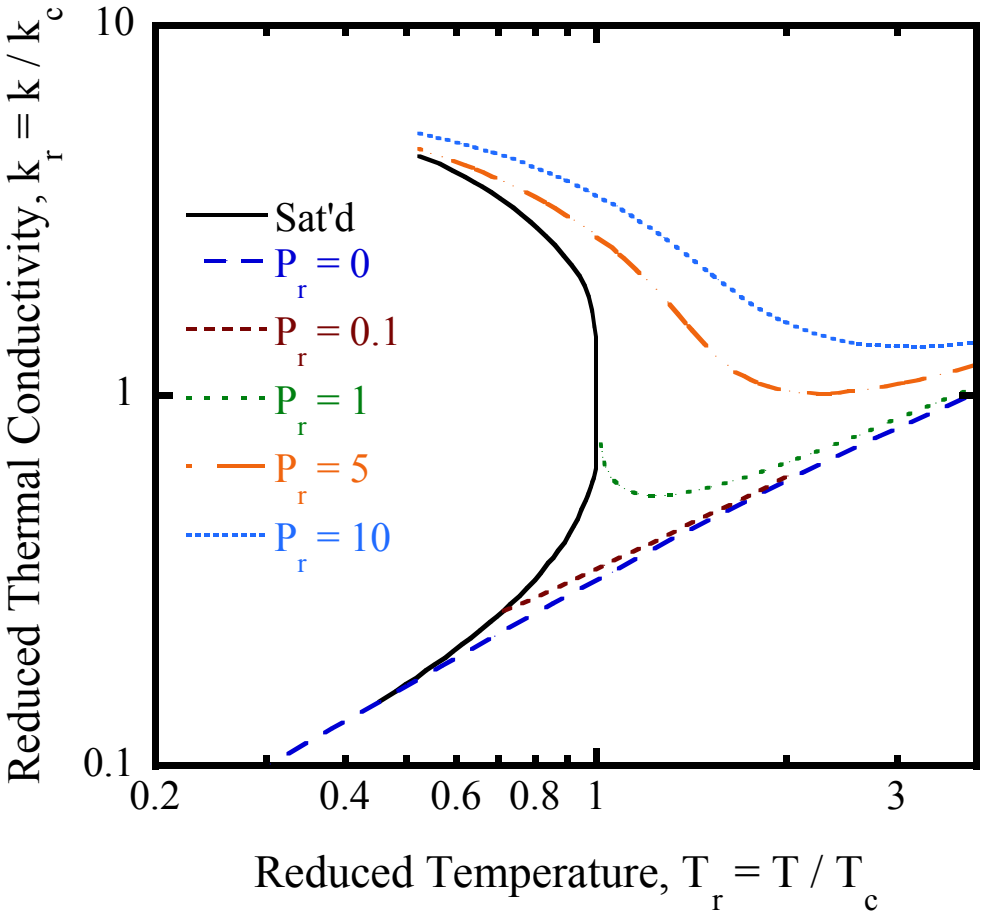

Figure 2.1 Reduced thermal conductivity of diatomic fluids as a function of reduced temperature and pressure adapted from Bird et al. [1]. The solid line represents a saturated fluid. The reduced values are defined as the absolute values normalized by the critical values.

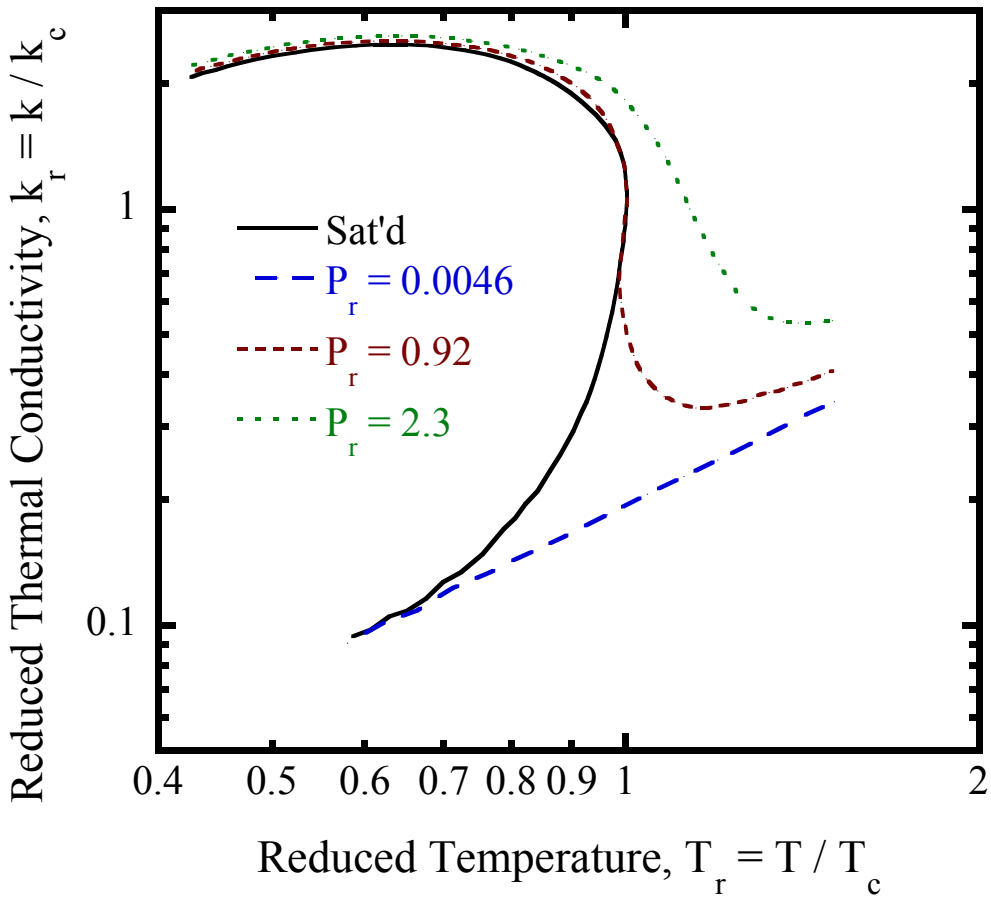

Figure 2.2 Reduced thermal conductivity of water as a function of reduced temperature and pressure [23]. The solid line represents saturated water. The reduced values are defined as the absolute values normalized by the critical values.

2.2 Thermal Conductivity of Solids

Heat can be conducted through solids by several different excitations. In metals, the primary heat carriers are free electrons. In insulators and in some semiconductors, lattice waves (phonons) are primarily responsible for heat transfer. Thermal conduction by electrons is more effective than conduction by phonons, which is demonstrated by the orders of magnitude difference between the thermal conductivity of metals and insulators in Table 2.1. As a rule of thumb materials that exhibit greater electrical conductivity also exhibit greater thermal conductivity. Thus, copper is a better conductor of electricity than aluminum and also exhibits a greater thermal conductivity. There are some notable exceptions to this rule such as diamond, which is an excellent electrical insulator (10^{17} Ω m^{-1} [31]), but has a thermal conductivity of 900 W m^{-1} K^{-1} [32].

The thermal conductivity is greatly dependent on the structure of the solid, even when the solids have identical chemical formulas. For example, amorphous carbon has a thermal conductivity of approximately 1.6 W m^{-1} K^{-1} [17], but diamond and carbon nanotubes can exhibit thermal conductivities as high as 900 W m^{-1} K^{-1} [32] and 2000 W m^{-1} K^{-1} [7], respectively. Crystalline solids typically conduct heat more readily than amorphous solids and therefore their thermal conductivities are higher than those of amorphous solids. In crystalline solids, the phase, crystallite size, and impurities affect the thermal conductivity. In amorphous solids, the degree of molecular order is the dominant variable in heat conduction [1] This work focuses on insulators, so the following discussion is limited to conduction by phonons, which gives rise to lattice thermal conductivity [33].

2.2.1 Lattice Thermal Conductivity

Phonons are defined as quantized modes of vibration in a solid crystalline lattice, which arise from the vibrations of atoms within the lattice. Due to the proximity of atoms, their vibrations are strongly coupled with those of neighboring atoms. Since chemical bonds between atoms are generally not rigid and are similar to springs, the displacement of an atom from its equilibrium position also affects neighboring atoms. The oscillating motion of these coupled atoms is analogous to acoustic waves moving through the lattice. In the presence of a temperature gradient, energy is propagated through the lattice by these phonon waves [34], as illustrated in Figure 2.3. If the atoms oscillated harmonically, the velocity of phonon waves would be the speed of sound in a crystal. However, anharmonicity is caused by higher order interactions among atoms, known as phonon scattering, which lead to a change in direction of the phonon wave [35]. Phonon scattering can be divided into elastic phonon scattering, where phonon momentum is conserved, and inelastic scattering, where it is not. Inelastic scattering creates resistance to thermal transport and lowers the thermal conductivity. Scattering can result from collisions of phonons with each other (Umklapp scattering) or defects in the crystal structure such as impurities and grain boundaries.

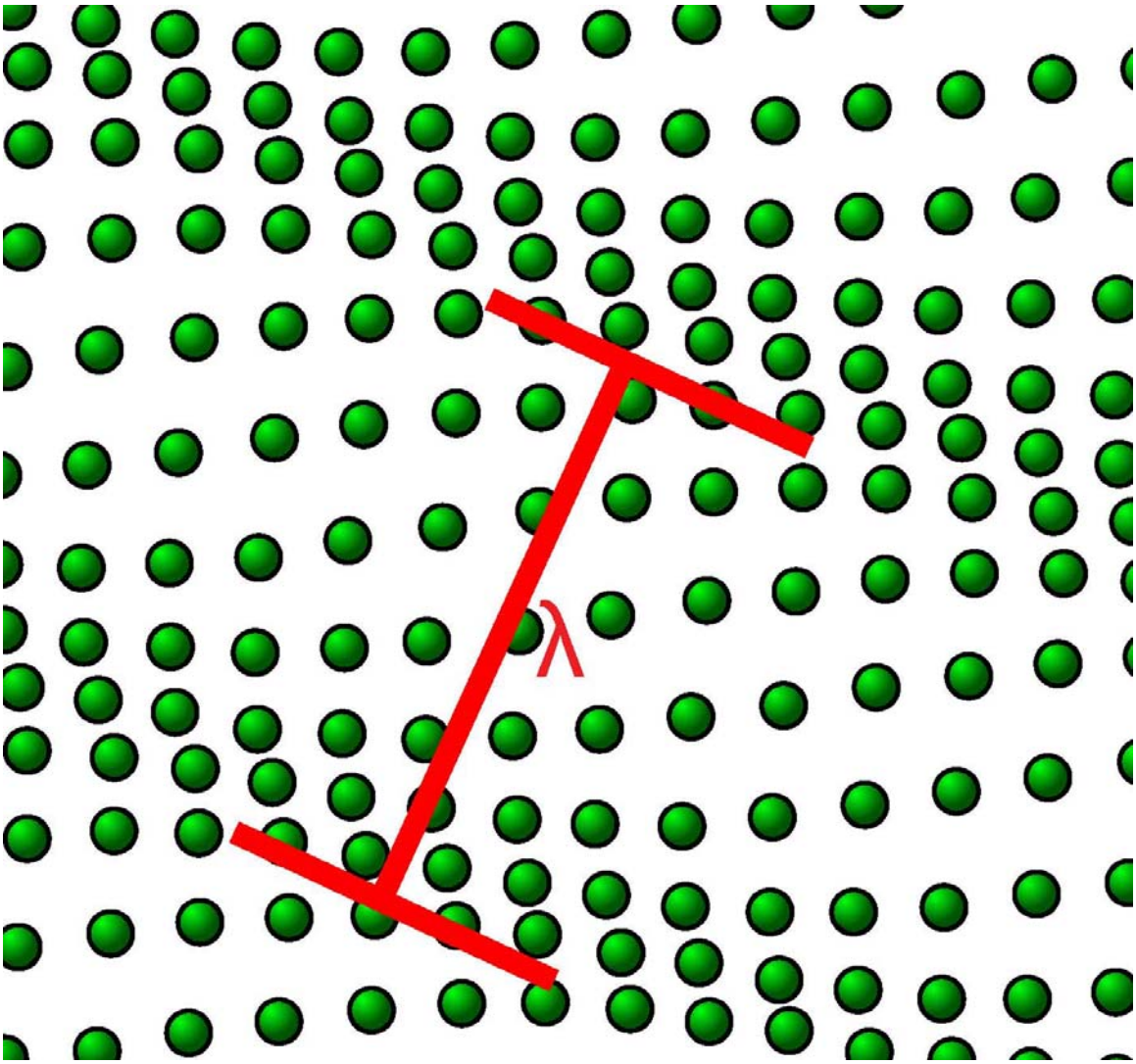

Figure 2.3 Illustration of a phonon wave [36]

2.2.2 Temperature Dependence

The thermal conductivities generally increase for nonmetals and decrease for metals as temperature increases [1]. An exception to this rule is alumina, which despite being a nonmetal, exhibits a decreasing thermal conductivity with increasing temperature (Figure 2.4). The thermal conductivity of alumina decreases 25 % when heated from 300 to 400 K. The magnitude of this reduction is similar to that generally exhibited by liquids such as hexane. The thermal conductivity of hexane decreases 22.6 % when it is heated from 235 to 335 K.

The decrease in thermal conductivity with increasing temperature for alumina and other crystalline solids arises from the temperature dependence of Umklapp scattering, which is the dominant source of heat transfer resistance at ambient and higher temperatures. The mean free path for phonons (l) is limited by Umklapp scattering and exhibits the following relationship:

$$l \propto T^{-n} \tag{2.2}$$

where n is typically greater than 1.

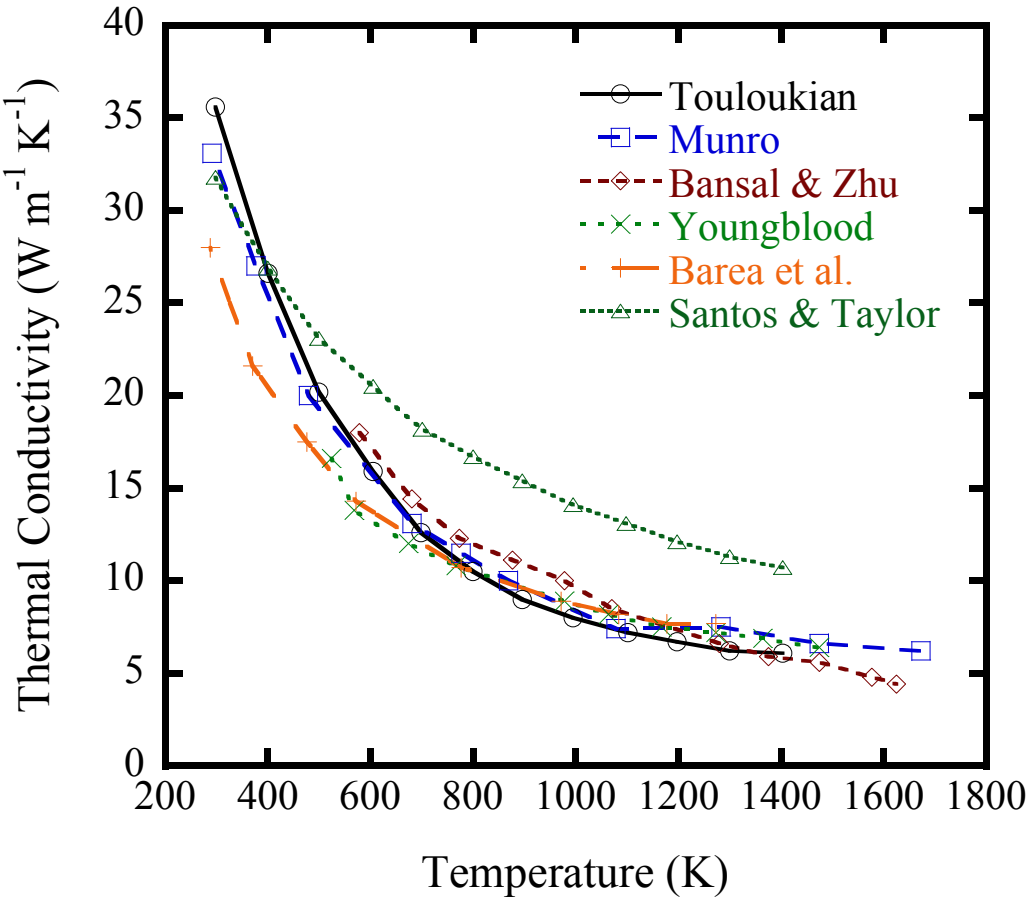

Figure 2.4 Thermal conductivity of alumina from various studies. Adapted from Bansal & Zhu [37].

2.2.3 Thermal Conductivity of Solids as a Function of Size and Dimension

Several recent studies have focused on thermal conduction in nanoscale thin films due to their use in microelectronics [38-40]. Thermal conductivities of submicron films were measured and shown to decrease as the thickness of the film decreased. For example, Liu et al. [40] found that for a 20 nm thick silicon film, the out-of-plane thermal conductivity was nearly an order of magnitude less than the bulk value. Figure 2.5 displays their data along with those of others for the out-of-plane thermal conductivity of thin silicon films. They suggested that phonon scattering at the interface of the solid becomes the dominant source of thermal resistance in solid nanomaterials because of their large specific surface area. A less substantial decrease of the in-plane thermal conductivity (~10 % at 300 K) was observed by Yu et al. [41] in a superlattice with a 70 nm periodic structure.

Phonon-interface scattering is not as well understood as other phonon scattering processes (such as boundary scattering or phonon-phonon scattering), and it is seldom incorporated into predictive methods for the thermal conductivity of solids. This could be the reason why most methods are unable to predict the reduced thermal conductivity of nanostructured materials [42]. Ziambaras and Hyldgaard [43] examined the thermal conductivity of nanoscale films and wires using the Boltzmann transport equation and including the effect of phonon-interface scattering. Their results indicate that the axial thermal conductivity of a wire is less than the in-plane thermal conductivity of a film of the same thickness. They suggested this effect is caused by confinement of the phonon wave since the thickness of the nanomaterial is similar to the phonon mean free path, similar to Knudsen diffusion. Thus, nanowires, which are confined in two dimensions,

should exhibit a lower thermal conductivity than nanofilms which are only confined in one dimension. Li et al. [44] demonstrated this effect when they measured axial heat conduction in silicon wires as small as 22 nm in diameter, and found the thermal conductivity to be more than two orders of magnitude less than the bulk value. The axial thermal conductivity of a 22 nm diameter Si nanowire is approximately 6 W m^{-1} K^{-1}, while the out-of-plane thermal conductivity for a 20 nm thick Si film is 22 W m^{-1} K^{-1} [40].

Nanoparticles should exhibit an even lower thermal conductivity than nanowires or nanofilms because they are confined in three dimensions. Fang et al. [45] came to the same conclusion using their molecular dynamic simulations to estimate the thermal conductivity of silicon nanoparticles. They found that below 8 nm, silicon nanoparticles exhibited a two order of magnitude decrease in thermal conductivity (~ 2 W m^{-1} K^{-1}) compared to the bulk material (237 W m^{-1} K^{-1}). This decreased thermal conductivity of nanoparticles should be considered in the study of the thermal conductivity of nanofluids.

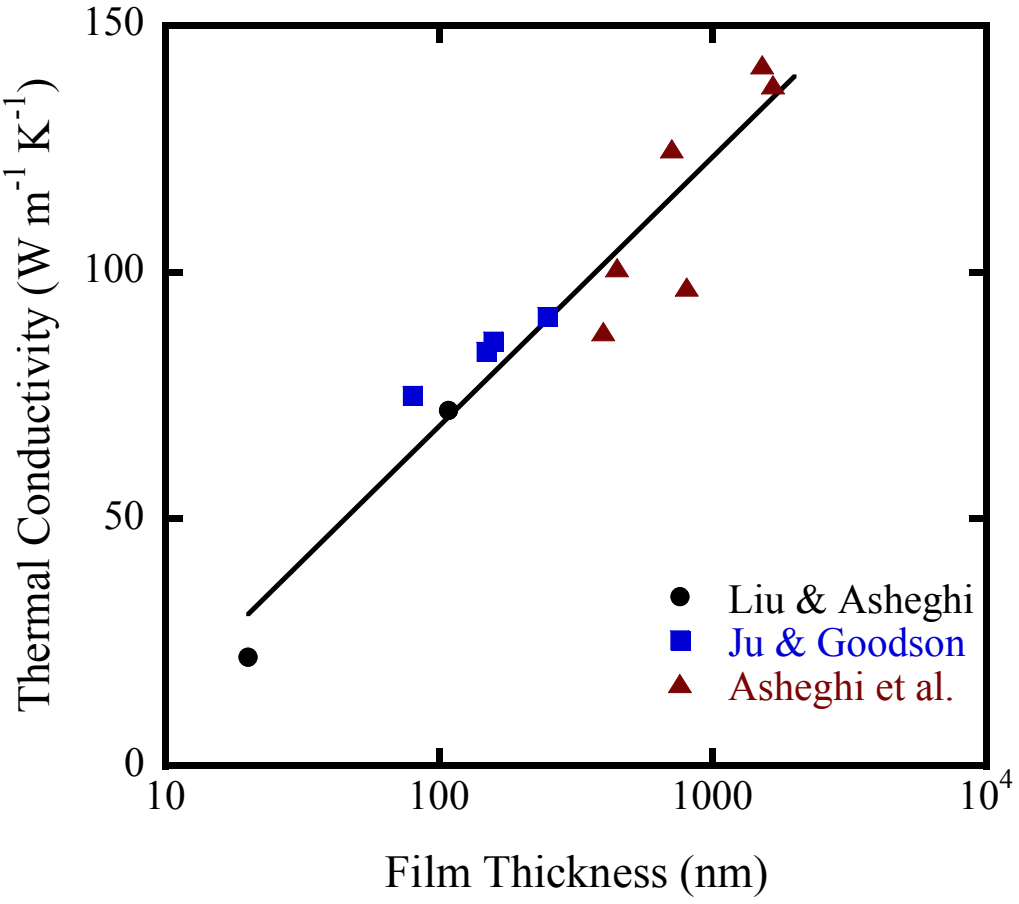

Figure 2.5 Out-of-plane thermal conductivity at room temperature for silicon films. Adapted from Liu & Asheghi [40]. A linear fit is provided as a visual aid.

2.3 Thermal Conductivity of Heterogeneous Systems

Thermal transport in heterogeneous systems has been studied extensively due to their wide range of industrial applications. Some examples include the modeling of transport in packed beds and the freezing and thawing of food products. Nanofluids represent a subset of heterogeneous materials. Consequently, a comparison of the thermal conductivity behavior of nanofluids and of other heterogeneous materials should provide insight into the effect of decreasing particle size on the conduction mechanism.

2.3.1 Thermal Conductivity of Microparticle Dispersions

Shin and Lee [46] measured the thermal conductivity of polyethylene and polypropylene particles suspended in mixtures of silicon oil and kerosene. The particle diameters ranged from 25 to 300 μm. At 10 % (v/v) particles, all suspensions exhibited a 13 % thermal conductivity enhancement. Thermal conductivity enhancement is defined as the relative difference in thermal conductivity of the dispersion (k_{eff}) and the pure liquid (k_1), $\left(k_{eff} - k_1\right)/k_1$. Shin and Lee observed a linear relationship between the thermal conductivity and volume fraction of particles, but they did not observe any dependence on the particle size. Bjorneklett et al. [47] reported measurements of the thermal conductivity of epoxy containing silver particles for various volume fractions of silver. The epoxy containing 6.25 % (v/v) silver particles exhibited a 160 % thermal conductivity enhancement due to the large thermal conductivity difference between the silver and epoxy. The thermal conductivity varied linearly with volume fraction up to 6.25 % volume fraction. At volume fractions greater than 6.25 %, the slope increased

until the thermal conductivity of epoxy containing 23.1 % (v/v) silver particles was 790 % greater than the pure epoxy.

Turian et al. [48] measured the thermal conductivity of a number of fluids containing as much as 50 % (v/v) suspended coal, glass, gypsum, and silica particles. The ratios of the thermal conductivities of these solids to liquids (k_2 / k_1) were relatively small (< 14). For example, silica has a thermal conductivity of approximately 1.3 W m^{-1} K^{-1} while for water it is 0.6 W m^{-1} K^{-1} giving a thermal conductivity ratio of 2.2. Consequently, the thermal conductivity enhancement for such suspensions was found to be small, 18 % enhancement in the case of an aqueous dispersion containing 12 % (v/v) silica particles. Turian et al. also observed a linear relationship between thermal conductivity and volume fraction at dilute concentrations, although beyond 10 % (v/v) of particles, the slope increased as the concentration increased.

2.3.2 Thermal Conductivity of Nanofluids

The thermal conductivity of nanofluids has drawn increasing attention since Choi [3] first postulated that heat transfer could be improved through the addition of metallic nanoparticles to the heat transfer fluid. He addressed the limitation in thermal conductivity of typical heat transfer fluids and suggested the addition of more conductive solid particles would enhance the fluid thermal conductivity beyond that suggested by conventional models. The advantages of using nanoparticles are that they are more easily suspended in the fluid, they may be used in microchannels, and the small size causes less wear to machinery. However, aggregation of particles must be minimized in order to benefit from these effects of small particle size.

Eastman et al. [49] measured the thermal conductivity of nanofluids, and found that an aqueous nanofluid containing 5 % (v/v) CuO nanoparticles exhibited a thermal conductivity 60 % greater than that of water. Additionally, they reported a 40 % greater thermal conductivity compared to water for an aqueous nanofluid containing 5 % volume fraction of Al_2O_3 nanoparticles [49]. Subsequently, many authors have presented data for a wide variety of nanofluids. A list of nanofluid systems for which the thermal conductivity has been measured is presented in Table 2.2. Some of these nanofluids exhibit thermal conductivities that are in good agreement with the conventional models described in Chapter 5 (within 10 %), while other nanofluids exhibit anomalous thermal conductivities which are greater than predicted (> 25% deviation). The reasons for these discrepancies remain unknown, but they may arise from experimental error in the measurement technique or differences in sample preparation.

Table 2.2 List of references containing thermal conductivity data of nanofluids

Nanoparticle	k_2 / k_1	Fluid
Al_2O_3	66	Water [8, 9, 11-13, 49-60]
	156	Ethylene Glycol [12, 13, 53, 57-59]
	140	Glycerol [59]
	342	Oil [12, 53, 59, 61]
CuO	127	Water [8, 9, 11, 18, 49, 51, 53, 57, 60, 62, 63]
	300	Ethylene Glycol [18, 53, 57, 62, 64, 65]
TiO_2	14	Water [11, 13, 51, 56, 66, 67]
	33	Ethylene Glycol [13, 68]
Fe_3O_4	11.5	Water [69]
ZrO_2		Water [51]
WO_3		Ethylene Glycol [56]
ZnO	48	Water [13]
	113	Ethylene Glycol [13]
SiO_2	2.2	Water [18, 32, 62, 67]
	5.2	Ethylene Glycol [32, 67]
	7.8	Ethanol [67]
SiC	806	Water [70]
	1910	Ethylene Glycol [70]
Cu	655	Water [71-73]
	1550	Ethylene Glycol [60, 74, 75]
		Water + Ethylene Glycol [76]
	3400	Oil [49, 71]
	3060	Perfluorotriethylamine [25]
Ag	697	Water [32, 77]
		Water + Ammonia [77]
		Water + Ethylene Glycol [77]
Au	518	Water [61, 73]
	1830	Ethanol [78]
	2370	Toluene [11, 54, 78]
Fe	132	Water [68]
	311	Ethylene Glycol [55, 56, 79, 80]
Al_xCu_y		Water [81, 82]
		Ethylene Glycol [81, 82]
Ag_xCu_y		Oil [83]
Ag_xAl_y		Water [82]
		Ethylene Glycol [82]
Bi_2Te_3	42.7	Oil [10]
	87.7	Perfluorohexane [10]

Table 2.2 (continued)

Carbon Nanotubes	3290 7780 17100 14300	Water [11, 18, 24, 62, 73, 75, 84-89] Ethylene Glycol [24, 62, 75, 90, 91] Antifreeze [87] Oil [7, 18, 27, 75, 90, 92, 93] Decene [24]
Carbon Nanofibers	21.4 111	Water [54] Oil [27]
C_{60}-C_{70} (Fullerenes)	0.66 3.01 3.42	Water [18] Toluene [78] Oil [18]
Graphite	196 1020	Water [94] Oil [27]
Diamond	3500	Ethylene Glycol [32]

The following examples are some of the more notable thermal conductivity results for nanofluids. Choi et al. [7] reported a 150 % thermal conductivity enhancement of poly (α-olefin) oil with the addition of multiwalled carbon nanotubes (MWCNT) at 1 % volume fraction. Similarly, Yang et al. [93] reported a 200 % thermal conductivity enhancement for poly (α-olefin) oil containing 0.35 % (v/v) MWCNT. It is important to note that this thermal conductivity enhancement was accompanied by a three order of magnitude increase in viscosity. Eastman et al. [74] found a 40 % thermal conductivity enhancement for ethylene glycol with 0.3 % (v/v) copper nanoparticles (10 nm diameter), although the authors added about 1 % (v/v) thioglycolic acid to aid in the dispersion of the nanoparticles. The addition of this dispersant yielded a greater thermal conductivity than the same concentration of nanoparticles in the ethylene glycol without the dispersant. Jana et al. [73] measured the thermal conductivity of a similar copper containing nanofluid, except the base fluid was water and laurate salt was used as a dispersant. They observed a 70 % thermal conductivity enhancement for 0.3 % (v/v) Cu

nanoparticles in water. Kang et al. [32] reported a 75 % thermal conductivity enhancement for ethylene glycol with 1.2 % (v/v) diamond nanoparticles between 30 and 50 nm in diameter. Despite these remarkable results, some researchers have measured the thermal conductivity of nanofluids and have found no anomalous results. Also, those results can often be predicted by conventional thermal conductivity models [11, 51, 54, 58]. It is therefore unclear why certain nanofluids exhibit anomalous thermal conductivity enhancement while other nanofluids do not.

2.3.2.1 Effect of Volume Fraction

Most of the nanofluid thermal conductivity data in the literature exhibit a linear relationship with the volume fraction of particles as shown in Figure 2.6. However, some exceptions have shown a non-linear relationship especially at low volume fraction (< 1 %) [66, 69]. In these studies, the slope of the thermal conductivity versus volume fraction can be divided into two linear regimes. At low concentrations, the slope was greater than at high concentrations. This typically occurred around 1 % (v/v) as seen in Figure 2.7.

Some researchers have observed anomalous thermal conductivity enhancement for dilute suspensions (< 1 % by volume) of metallic nanoparticles [72-74, 83]. In addition to the aforementioned results of Eastman et al. [74] and Jana et al. [73], Ceylan et al. [83] measured a thermal conductivity enhancement of 33 % for 0.006 % (v/v) Ag – Cu alloy nanoparticles in pump oil. Yet others have reported no anomalous enhancement for similar systems [54, 78]. Limited data are available for these ultra dilute metal nanofluids, but there does not seem to be any explanations for the large differences in results (Figure 2.8).

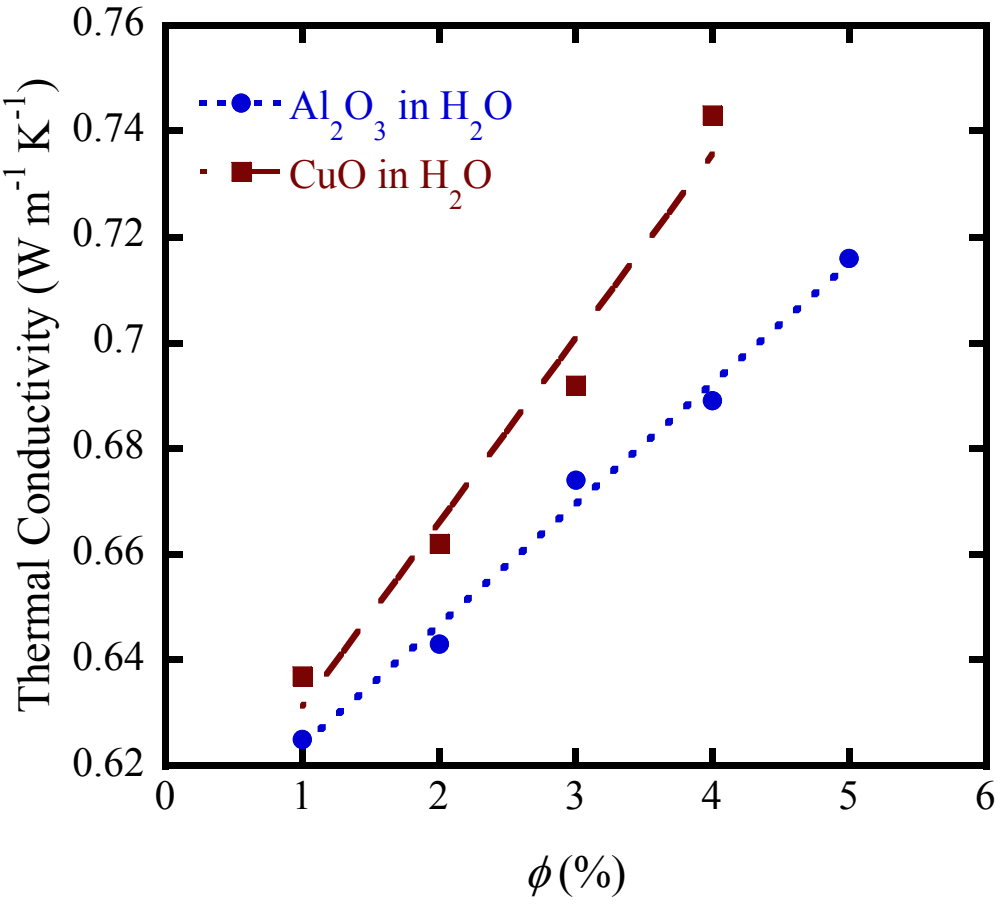

Figure 2.6 Thermal conductivity of aqueous nanofluids containing metal oxides as measured by Eastman et al. [60]. The dashed lines represent linear fits of the data.

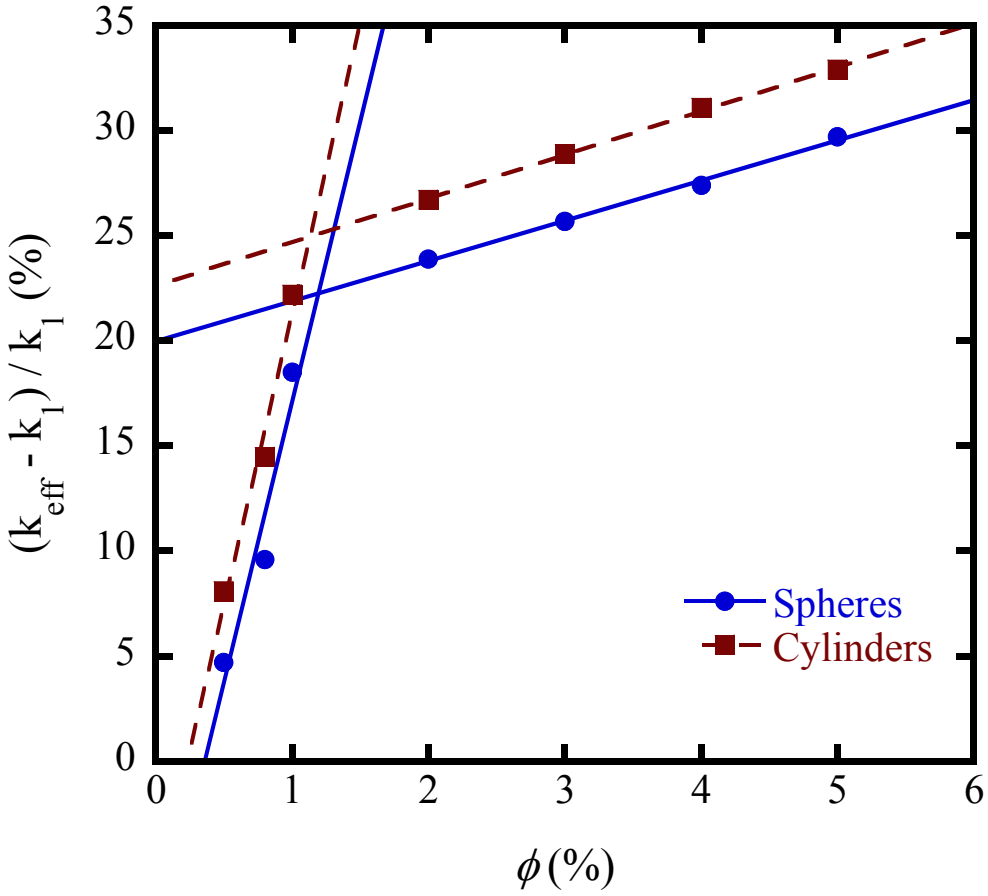

Figure 2.7 Thermal conductivity enhancement of nanofluids containing TiO_2 in water for both spherical and rod shaped nanoparticles as measured by Murshed et al. [66]. The lines represent fits of each linear regime.

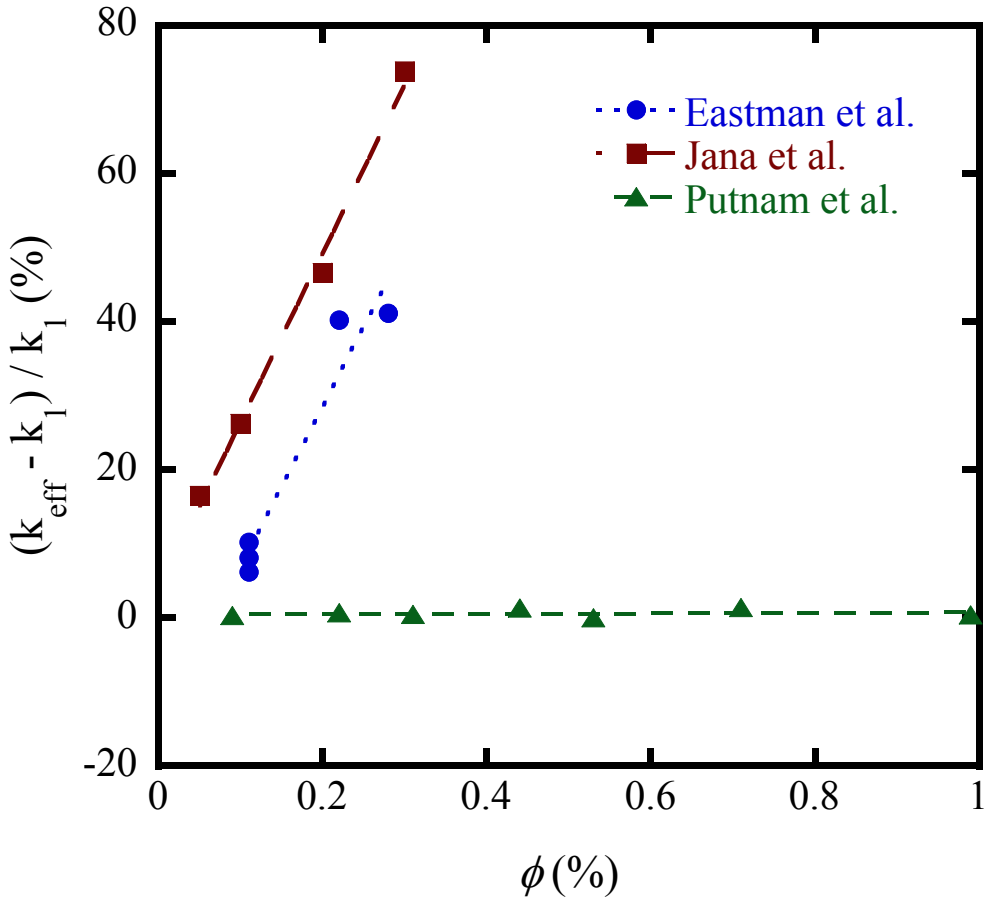

Figure 2.8 Thermal conductivity enhancement for dilute metal nanofluids. The circles (●) represent the measurements by Eastman et al. [74] of Cu (10 nm) in ethylene glycol + 1 % (v/v) thioglycolic acid. The squares (■) represent the measurements by Jana et al. [73] of Cu (35 – 50 nm) in water + laurate salt. The triangles (▲) represent measurements by Putnam et al. [78] of alkanethiolate – stabilized Au (2 – 4 nm) in toluene.

2.3.2.2 Effect of Particle Size

Xie et al [12] measured the thermal conductivity of nanofluids containing different sizes of alumina nanoparticles with diameters between 12 nm (124 m^2 g^{-1}) and 304 nm (5 m^2 g^{-1}). With the exception of the largest particles, the thermal conductivity decreased as particle size decreased as seen in Figure 2.9. They concluded that there is an optimal particle size which yields the greatest thermal conductivity enhancement. However, Kim et al. [13] measured the thermal conductivity of nanofluids containing different sizes of Al_2O_3, TiO_2, and ZnO in water and in ethylene glycol. They observed greater thermal conductivity for nanofluids containing the smaller nanoparticles. For nanofluids containing 3 % (v/v) TiO_2 in ethylene glycol, the thermal conductivity enhancement for the 10 nm sample (16 %) was approximately double the enhancement for the 70 nm sample. Li and Peterson [52] also observed up to 8 % greater thermal conductivity enhancement for aqueous nanofluids containing 36 nm Al_2O_3 particles compared to nanofluids containing 47 nm Al_2O_3 particles.

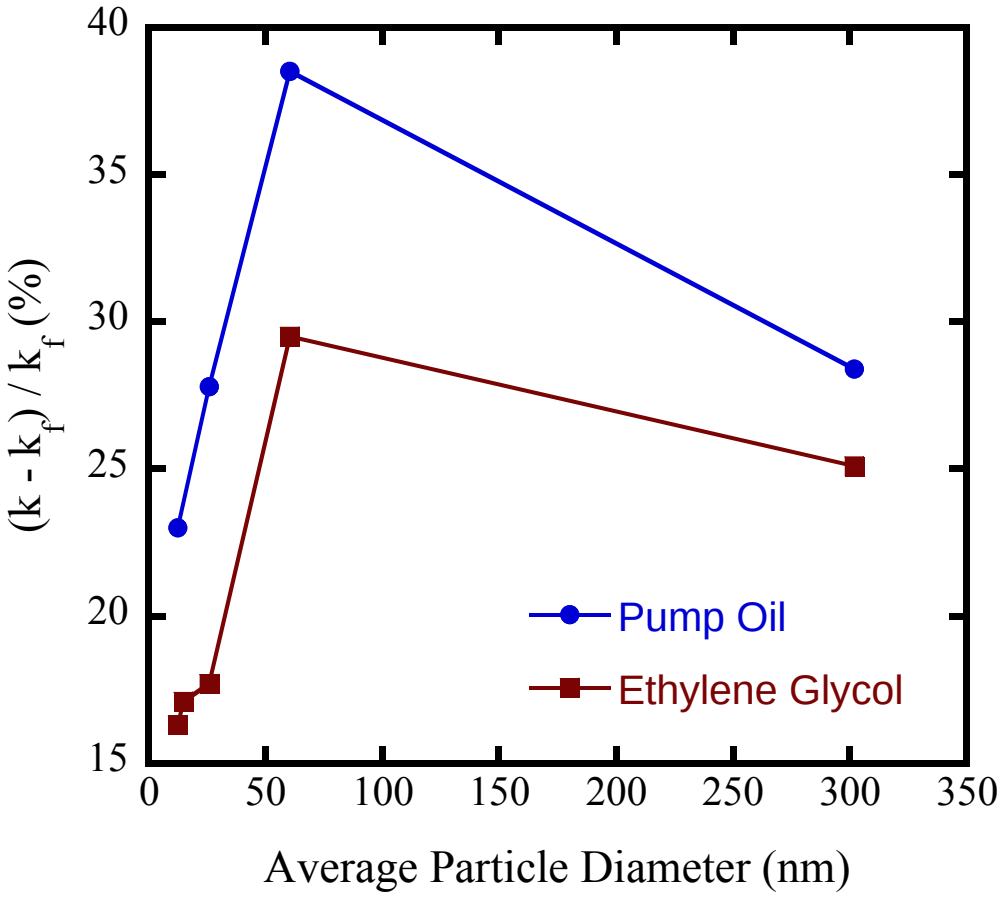

Figure 2.9 Thermal conductivity enhancement of nanofluids consisting of alumina particles in pump oil and ethylene glycol as a function of particle size as measured by Xie et al. [12]

2.3.2.3 Effect of Temperature

Das et al [8] measured the thermal conductivity of aqueous nanofluids containing Al_2O_3 and CuO at temperatures between 20 and 50 ºC. They observed that the thermal conductivity increased as the temperature increased and speculated that this behavior is typical of nanofluids over greater temperature ranges as well. However, they did not measure the thermal conductivity of aqueous nanofluids at temperatures greater than 130 ºC where the thermal conductivity of saturated water attains a maximum. Over the limited temperature range considered in their study, a gradual curve could appear linear. Thus, more comprehensive data is required before concluding whether the thermal conductivity exhibits a linear relationship with temperature. In contrast, Yang and Han [10] reported thermal conductivity measurements of perfluorohexane (FC-72) containing semiconductor (Bi_2Te_3) nanorods. They observed a decrease in the effective thermal conductivity as the temperature increased from 5 to 50 ºC. This trend is similar to the relationship between the thermal conductivity of non-polar liquids and thermal conductivity [1]. Figure 2.10 illustrates the contrast among the observed temperature dependence of the thermal conductivity of nanofluids.

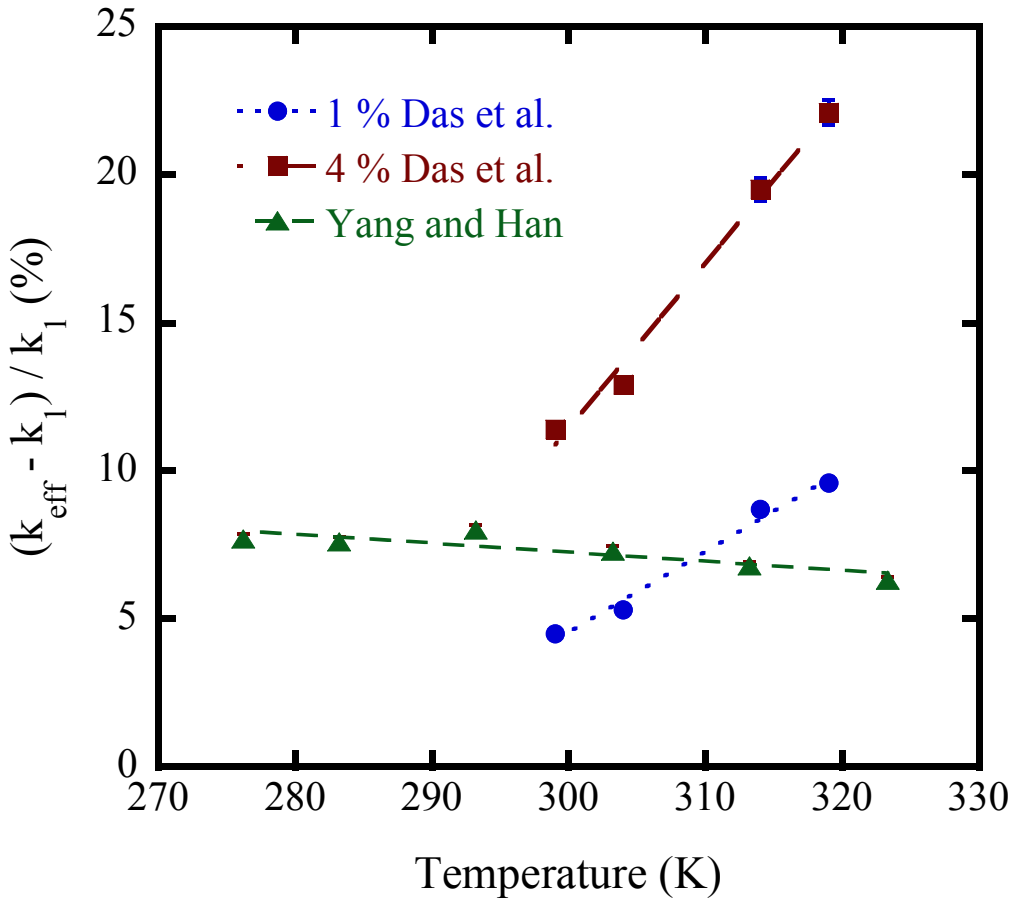

Figure 2.10 Thermal conductivity enhancement nanofluids as a function of temperature. The circles and squares represent measurements by Das et al. [8] of aqueous nanofluids containing alumina. The triangles represent measurements by Yang and Han [10] of nanofluids consisting of perfluorohexane and Bi_2Te_3 nanorods.

2.3.2.4 Effect of Ratio of Particle to Fluid Thermal Conductivity

Xie et al. [59] also examined the effect of the thermal conductivity of the base fluid using measurements of the thermal conductivity of nanofluids containing 60 nm diameter (25 $m^2 g^{-1}$) alumina nanoparticles dispersed in different base fluids. The ratio of particle to fluid thermal conductivity, α, ranged from 75 to 326. They observed a greater relative thermal conductivity enhancement for nanofluids with a greater α. The enhancement for the least conductive nanofluid (alumina in pump oil, $\alpha = 326$) was nearly 40 %, while the enhancement for the most conductive nanofluid (alumina in water, $\alpha = 75$) was about 23 %.

Several studies have explored the thermal conductivity of nanofluids with the same base fluid but with different nanoparticles [8, 9, 49, 53, 57, 62]. The thermal conductivity enhancement was greater for systems with greater α.

Similarly, some of the largest thermal conductivity enhancements observed in nanofluids have contained highly thermally conductive particles (copper [74], carbon nanotubes [7], diamonds [32]) in the same base fluids as nanofluids containing less conductive particles, which exhibited much lower thermal conductivity enhancements [59].

2.3.2.5 Effect of Particle Surface Charge

Lee et al. [63] explored the effect of the charge at the particle surface by varying the pH of the water before dispersing the nanoparticles. They observed a greater thermal conductivity enhancement at the acidic and basic pH range and a lower enhancement for

nanofluids with neutral pH values and concluded that greater surface charges increase the stability of the dispersion leading to an increased thermal conductivity.

2.3.2.6 Effect of Particle Arrangement in Suspension

Wright et al. [88] studied the thermal conductivity of dilute nanofluids containing 0.01 – 0.02 % Ni coated single wall carbon nanotubes (SWCNTs) within a magnetic field. They observed greater thermal conductivity enhancement when the magnetic field was applied, which suggested that the SWCNTs aligned to form chains creating greater conductive paths within the nanofluid. Hong et al. [95] and Wensel et al. [89] observed a similar phenomenon for dilute nanofluids containing both Fe_2O_3 and SWCNTs. However, after the nanofluids remain in the magnetic field for a certain amount of time the thermal conductivity decreases due to particle settling caused by greater particle agglomeration.

In this review, several discrepancies among the thermal conductivity data of nanofluids have been highlighted. Anomalous thermal conductivity enhancement (up to 200 %) has been observed in certain nanofluids, while not in others. The effect of smaller particle size has been shown to enhance conduction in some nanofluids and hinder conduction in others. Similarly, the effect of higher temperature has been shown to enhance conduction in some nanofluids, but it has also been shown to mimic the thermal conductivity behavior of the base fluid. Alternatively, there appears to be agreement on the relationship of the thermal conductivity of nanofluids with particle volume fraction ϕ and with the ratio of solid to liquid thermal conductivity α. The thermal conductivity linearly increases with particle volume fraction, and thermal conductivity enhancement is greater for nanofluids with greater α.

The reliability of thermal conductivity values of nanofluids in the literature is difficult to determine as evident by the aforementioned discrepancies in the observed behavior of the thermal conductivity with temperature and particle size. However, thermal conductivity measurements of commonly studied systems such as alumina in water have been reproduced within 2 % at room temperature [8, 9, 13, 50, 57, 58]. The lack of reliable and reproducible data at different temperatures and particle sizes make the development of predictive models difficult.

CHAPTER 3

TRANSIENT HOT-WIRE METHOD

In order to measure the thermal conductivity of a fluid, the measurement technique must be capable of isolating contributions due to heat conduction from those resulting from convection and radiation. Steady-state or transient methods can be used to achieve this. Steady-state methods generally confine the fluid between two surfaces, maintained at different temperatures. Two of the common geometries employed in these measurements are coaxial cylinders and parallel plates [96]. In the first method, the fluid occupies a thin annular gap between the two vertically oriented cylinders. By uniformly heating the inner cylinder while maintaining the outer cylinder at a constant lower temperature, a constant axial thermal gradient can be achieved. In the second method, the fluid occupies a thin gap between two horizontally aligned plates. The upper plate is maintained at a higher temperature so that the adjacent fluid is hotter and therefore less dense. This helps to eliminate free convection. Both methods are versatile and can be used to measure thermal conductivity over a wide range of temperature and pressure. Both methods are suitable for nonpolar as well as electrically conducting fluids. The basic equation for the thermal conductivity in these methods is rather straightforward,

$$k = c\frac{Q}{\Delta T} \tag{3.1}$$

where Q is the heat flow by conduction, ΔT is the temperature difference between the two surfaces, and c is the cell constant for the specific cell geometry. The difficulty with these methods is in the careful design and construction of the measurement cell.

Convection is minimized by keeping the coaxial cylinders perfectly aligned on a vertical axis, or keeping the parallel plates perfectly horizontal. Improper placement of one surface in relation to the other can yield a significant error due to convection. In addition, a correction must be applied to account for radiation and other heat losses. Heat is generated by resistive heating, and the heat flow Q due to conduction is obtained using,

$$Q = VI - Q_S - Q_R - Q_C \tag{3.2}$$

where V is the electric potential, I is the electric current, Q_S is the heat flow to the surroundings, Q_R is the heat flow by radiation, and Q_C is the heat flow by convection. The heat flow to the surroundings must be determined experimentally by calibrating the cell. The radiative heat flow can be found analytically for fluids which are entirely transparent. However, no analytical solution is available for partially transparent fluids. In this case, the heat transferred by radiation is found by measuring the apparent thermal conductivity while varying the thickness of the fluid gap between the solid surfaces. Due to this difficulty, the radiative heat transfer is generally minimized by designing the cell with a thin gap (0.2 – 0.3 mm) between the surfaces and using solid materials with low emissivity and highly polished surfaces. The convective heat transfer in these methods is often negligible when the cell is designed properly, but a correction can be applied by using the Rayleigh number with an empirical formula developed by Le Neindre and Tufeu as listed in Wakeham et al. [96]. When all sources of error are accounted for in a careful design, steady-state thermal conductivity measurements can be made with accuracies in the 1 – 3 % range.

Transient methods generally require that the fluid only be heated for several seconds to take advantage of the longer timescale for the onset of convection compared to

the propagation of thermal energy by conduction. These methods utilize a single surface to heat the fluid and to measure the temperature response to find the thermal conductivity of the surrounding medium. Transient methods eliminate the need for precise temperature control needed in steady-state methods. They employ a heated cylinder, plate, or wire suspended in a liquid to measure th thermal conductivity. The transient hot wire method is particularly simple to use because the wire can be modeled as a line. This simplicity also minimizes sources of heat loss compared to the steady-state systems. A significant advantage of the transient hot wire method is the ability to analytically verify the elimination of convective and radiative contributions to heat transfer. Free convection would appear in the data analysis as a deviation from the transient conduction model. Additionally, the radiative contribution to heat transfer is calculated in the analysis as detailed in Section 3.4.3.3. These properties of the transient hot wire method have made it the preferred method for thermal conductivity measurement, as demonstrated by the use of this method in many recent nanofluid studies [7, 11-13, 18, 24, 25, 32, 49-51, 54-59, 62-66, 68-72, 74-77, 79, 80, 84-86, 90, 93, 94, 97].

3.1 Basic Measurement Technique

The transient hot-wire technique utilizes a thin metal wire immersed vertically in the fluid of interest. This wire forms one resistor of a Wheatstone bridge with other resistors of known resistances. When a constant voltage is applied to the initially balanced bridge, heat is dissipated along the wire, and causes a temperature change in the wire. This temperature change and heating period must be small enough that convection does not occur during the measurement, and power is therefore supplied to the bridge for only a few seconds. The small temperature change in the wire induces a small change in

electrical resistance of the wire, which can then be used to determine the temperature change. Thus, the wire acts both as the heat source and a thermometer. The temperature versus time relationship is related to the thermal conductivity of the fluid via a specific solution to Fourier's law for an infinite line heat source in an infinite medium,

$$\Delta T = \frac{q}{4\pi k} \ln\left(\frac{4\alpha t}{r^2 \gamma}\right) \tag{3.3}$$

where ΔT is the temperature change of the wire, q is the heat dissipated per unit length, r is the distance from the heat source, γ is the exponent of Euler's constant, and k and α are the thermal conductivity and thermal diffusivity of the fluid, respectively [98]. Corrections must be applied for the finite extent of the real system, and are addressed in section 3.3.3.

3.2 Background of Transient Hot-wire Method

3.2.1 Basic Transient Hot-wire Method

The transient hot-wire method had been developed over many years, but did not become the predominant method of thermal conductivity measurement for fluids until the work of de Groot et al. [99], who showed that this method could be used to make absolute measurements of the thermal conductivity of gases up to 800 °C and 400 atm with an estimated accuracy and precision of 0.2 %. The accuracy was due to careful design of the system to minimize differences between the real and the model system. Each assumption that was made in the derivation of Equation 3.3 was analyzed to determine its significance [100], and corrections were applied to account for any deviations, particularly the change in physical properties due to the temperature increase and the finite extent of the wire and the fluid.

3.2.2 Insulated Wire Method

A transient hot-wire device with a bare metal wire can be used to measure the thermal conductivity of fluids which are not electrically conductive, such as gases and most organic liquids. In the case of electrically conducting liquids, current leakage would occur from the wire into the fluid, which would introduce significant error in the measurement of heat dissipated in the wire. Nagasaka and Nagashima [101] extended the method to measure electrolytes by adding a polyester insulating layer to the platinum wire to prevent electrical leakage. This layer of insulation added more complexity to the method, and created another correction during data analysis. However, they were able to measure the thermal conductivity of aqueous NaCl solutions between 0 and 45 °C with an estimated accuracy of 0.5 %.

3.2.3 Liquid Metal Wire Method

Hoshi et al. [102] further extended the insulated transient hot-wire method by using a borosilicate glass capillary as the insulating layer with a mercury wire. This method allows measurement over a greater temperature range than a coated wire, which is prone to cracking at high temperatures because of differences in thermal expansion of the two materials. They measured the thermal conductivity of molten salts at temperatures up to 300 °C with an estimated accuracy of 3.5 %.

The method developed by Hoshi et al. has been used extensively for the measurement of the thermal conductivity of electrically conducting liquids by DiGuilio and Teja who measured the thermal conductivity of aqueous salt solutions [103], and by Bleazard and Teja who measured the thermal conductivity of aqueous LiBr solutions and propionic acid and water mixtures [104], alkanediols [105], and acetic acid and water

mixtures [106]. More recently, Sun and Teja measured the thermal conductivity of various glycol and water mixtures [107, 108] and benzoic acid and water mixtures [109] using this method. The estimated accuracy of these measurements is approximately 2 %.

Two methods have been used to construct the capillary. The first method employed a high temperature rubber cement to seal the ends of a fine pyrex capillary to the ends of larger pyrex tubes to form a U shape shown in Figure 3.1 [110]. This method limits the temperature range of the thermal conductivity measurements because the capillary can break due to differences in the thermal expansion of the two materials. The second method consists of a single pyrex tube that is heated and stretched to form the capillary [111]. No sealant is needed, but the disadvantage is that the capillary created by this method has a non-uniform cross sectional area. However, this method allows measurements at higher temperatures than any of the previously mentioned methods. Due to the versatility and demonstrated effectiveness of the second method, it was chosen for measurement of the thermal conductivity of nanofluids in this work.

3.3 Construction of Transient Hot-wire Instrument

Two transient hot-wire instruments were used in this research. The first was designed and constructed by Bleazard and Teja [104], and consisted of a transient hot-wire cell and the electric apparatus illustrated in Figures 3.1 and 3.2, respectively. This instrument is described in detail by Bleazard and Teja [104] and was used to make the thermal conductivity measurements in Section 5.3.1. An updated apparatus which utilizes greater computing power, provides faster analysis, and is more user-friendly, was used to make the thermal conductivity measurements presented in Section 5.3.2.

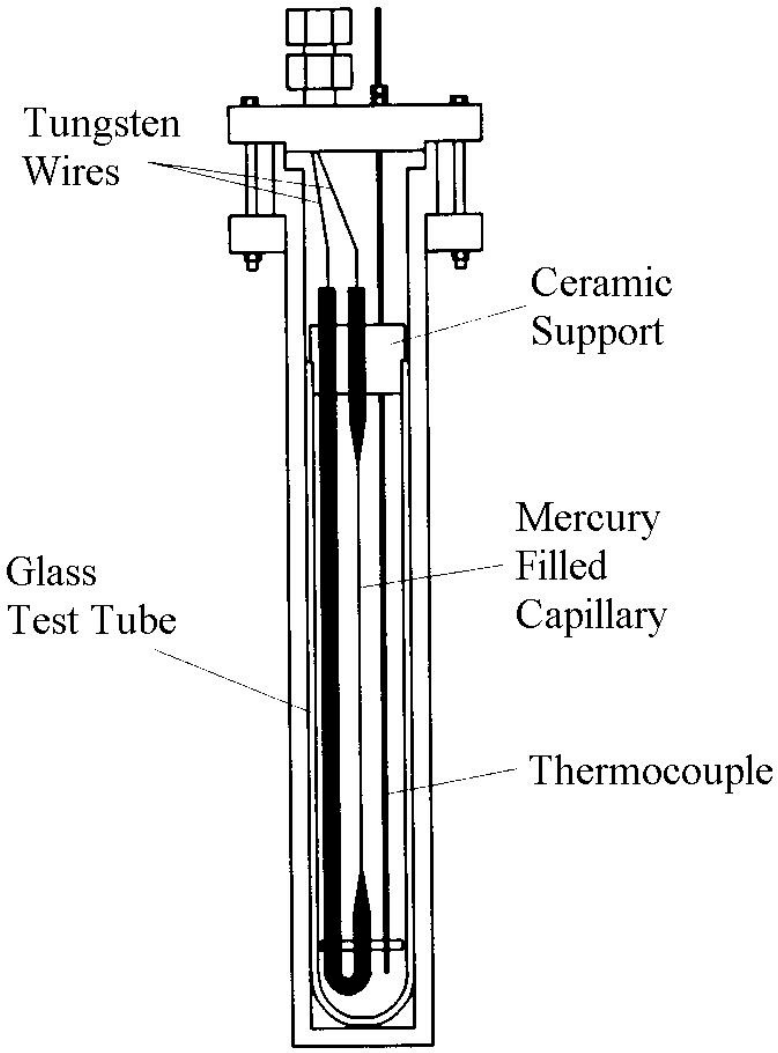

Figure 3.1 Liquid metal transient hot-wire cell. Adapted from Bleazard and Teja [104]

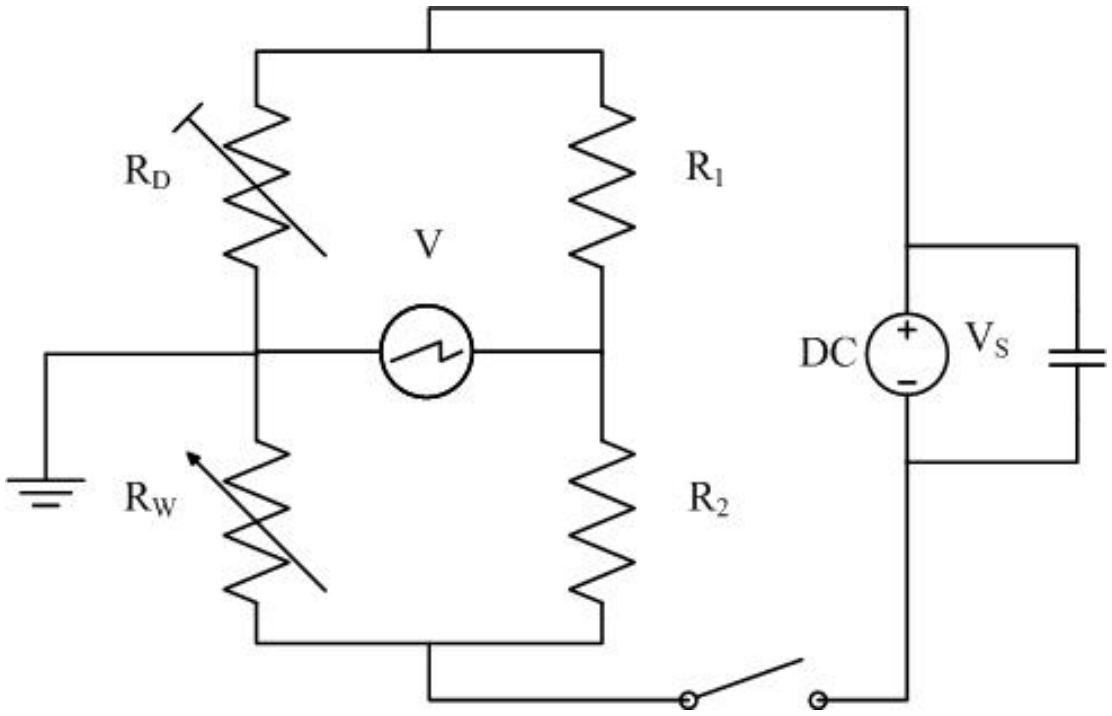

Figure 3.2 Electrical diagram of transient hot-wire apparatus.

3.3.1 Instrumentation

3.3.1.1 Hot Wire Cell

Both the original and updated instrument employed the same transient hot-wire cell. The cell consisted of a capillary formed from a standard wall borosilicate glass tube (4 mm OD, 2 mm ID) which was fixed in a ceramic support with ceramic epoxy (Thermeez Hi-Seal, Cotronics Corp.). The capillary was examined with a microscope to determine the dimensions. The average inner diameter was approximately 100 microns and the average outer diameter was approximately 250 microns. Mercury was drawn through the capillary with a vacuum pump, and tungsten wires were used to connect the mercury to the rest of the Wheatstone bridge. The mercury filled capillary was placed in a glass test tube containing the fluid to be studied, and the test tube was sealed and placed in a pressure vessel in a Techne fluidized sand bath (Model SBL-2D). The temperature of the fluid was determined with a type E thermocouple (see Appendix A for calibration).

3.3.1.2 Instrumentation of Bleazard and Teja

The electrical circuit is shown in Figure 3.2. The Wheatstone bridge consisted of the hot wire, two 100 ± 0.01 Ω precision resistors, and a 4-dial decade resistance box (General Radio 1433A) adjustable by ± 0.01 Ω with a maximum of 111.1 Ω. The bridge was powered by a Hewlett-Packard power supply (model 6213A), and a relay (Magnecraft W172DIP-1) was placed in series with the power supply to close the circuit when activated. An IBM PC XT and a Strawberry Tree analog to digital converter card (ACPC-16) was used to control the relay and for data acquisition.

3.3.1.3 Updated Instrumentation

All of the aforementioned components were replaced in the updated instrument. The new Wheatstone bridge circuit consisted of two 100 ± 0.005 % Ω precision wirewound resistors (RCD Components, Inc., Manchester, NH, Model 150B-1000-VB) and a 4-dial decade resistance box (IET Labs, Inc., Westbury, NY, HARS-X-4-0.01) adjustable by ± 0.01 Ω with a maximum of 111.1 Ω. The bridge was powered by an DC supply (Agilent, Santa Clara, CA, Model E3610A). A generic 100 μF capacitor was placed in parallel with the power supply for signal conditioning. A solid state relay (Omron Electronic Components, Schaumburg, IL, G3VM-61B1) was placed in series with the power supply, which closed the circuit when activated. A Dell computer containing an analog to digital (A/D) converter (IOtech, Cleveland, OH, ADAC/5502MF) was used to control the relay and for data acquisition and analysis.

There is no significant difference between the resistors in the updated instrument compared to the original instrument. However, the Agilent power supply is an upgrade from the original power supply because it produces a more reliable constant voltage than the original. Additionally, there was no capacitor for signal conditioning in the original instrument. The greatest difference between the original hardware and the updated hardware is the improved computing power of the Dell computer with the IOtech A/D. The original system recorded data at approximately 60 Hz for each channel, while the updated system records data at 1000 Hz for each channel.

3.3.2 Data Acquisition and Analysis

The apparatus designed by Bleazard and Teja employed a BASIC program to control the relay and for data acquisition and a separate Fortran program to analyze the data and obtain a thermal conductivity value.

In the updated apparatus, the graphical programming software LabVIEW (version 7.1) was chosen for the data acquisition and analysis and to control the relay. The LabVIEW program was designed to automatically collect the data, import data into MATLAB for data analysis, and then provide graphical analysis and a thermal conductivity value. The results from a typical thermal conductivity measurement are shown in Figure 3.3, and the actual LabVIEW and MATLAB code can be found in Appendix B. The graphical analysis includes plots of the measured data (voltage offset of the bridge and source voltage) and two plots of ΔT versus $\ln(t)$, one over the entire time period of the measurement, and the other a snapshot of the linear time period used to calculate thermal conductivity. The selection of this linear portion is described in Section 3.5. In the second plot, the experimental temperature changes are compared with predicted values for the wire. Graphical analysis provides the user with the ability to identify any errors that may arise during the measurement. Such errors include disturbances in the voltage source or the onset of convection, which would appear as a noticeable decrease in the slope on the ΔT versus $\ln(t)$ plot at later times.

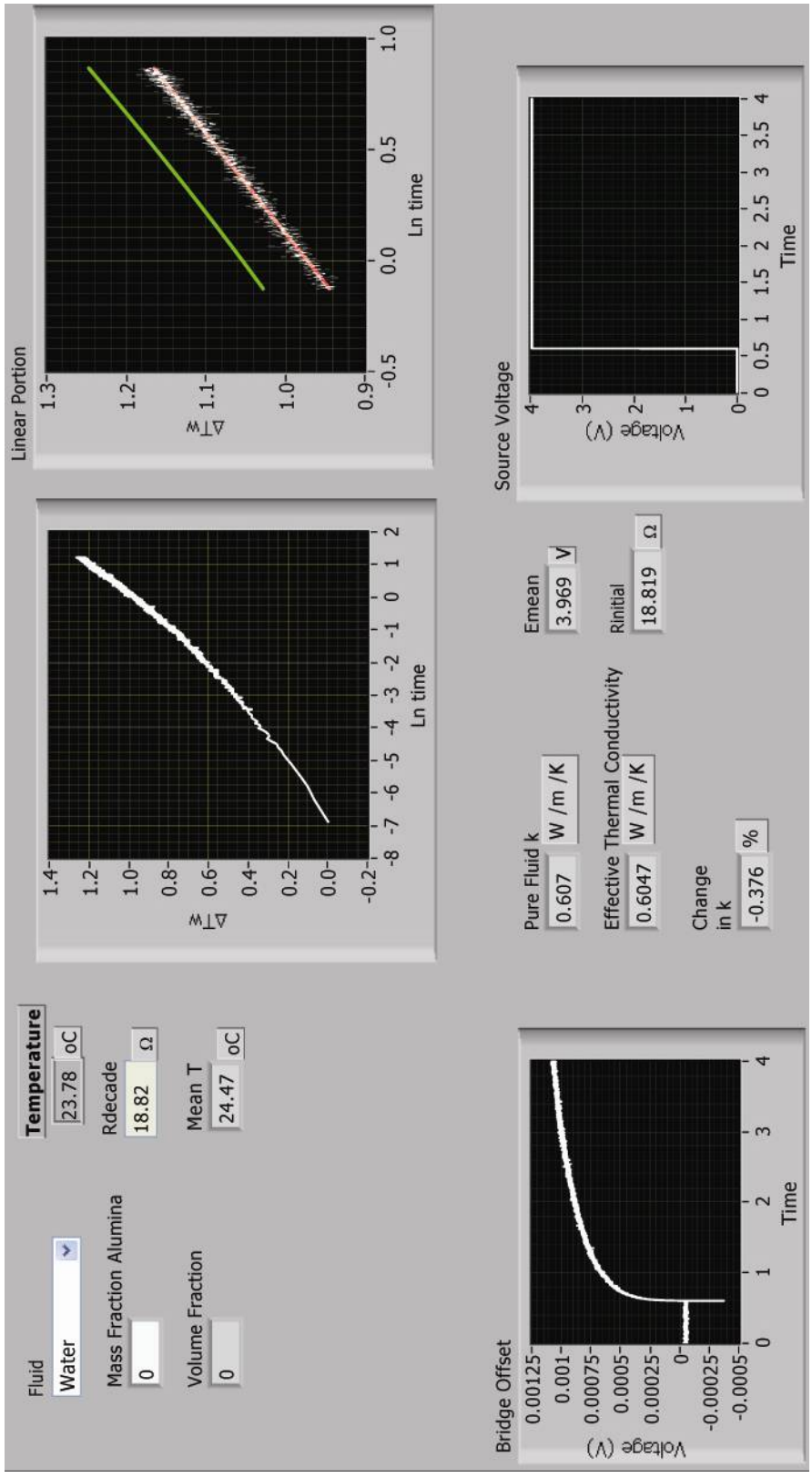

Figure 3.3 User interface in LabVIEW for transient hot wire device

3.4 Procedure, Analysis and Corrections

The following is a detailed description of the procedure and analysis used in this research.

3.4.1 Procedure

With the mercury filled capillary immersed in the fluid, the bridge is manually balanced by adjusting the decade resistance to a value which minimizes the absolute voltage offset. Then, the temperature of the fluid is measured using a thermocouple. This is followed by activation of a relay to close the circuit and allow a constant voltage to be supplied to the bridge. The current flowing through the wire gives rise to heat dissipation, which leads to an increase in the temperature of the wire. After several seconds, the relay is deactivated to open the circuit and stop current flow. The voltage across the bridge is measured at regular intervals while current flows through the circuit, and the voltage versus time data are analyzed as described below to determine the thermal conductivity.

3.4.2 Analysis

The thermal conductivity of the liquid is found from Fourier's law for an infinite line heat source in an infinite medium (Eq. 3.3). Equation 3.3 can also be written,

$$\Delta T = \frac{q}{4\pi k}\ln(t) + \frac{q}{4\pi k}\ln\left(\frac{4\alpha}{r^2\gamma}\right) \tag{3.4}$$

Thus, if the physical properties of the fluid are effectively constant during the measurement, the relationship between ΔT and ln (t) has the following slope,

$$\frac{d(\Delta T)}{d(\ln t)} = \frac{q}{4\pi k} \tag{3.5}$$

Since the heat dissipated in the wire is effectively constant, the slope is constant and the relationship between ΔT and ln (t) is linear. Thus, the thermal conductivity can be found from the slope and the heat dissipated (Eq. 3.5).

The temperature change of the wire is calculated from the voltage offset data using the following equation to find the resistance of the wire R_W,

$$R_W(t) = \frac{V_S R_D (R_1 + R_2)}{V_S R_1 + V(t)(R_1 + R_2)} - R_D \tag{3.6}$$

where R_D is the resistance of the decade box, R_1 and R_2 are the resistances of the corresponding fixed resistors in Figure 3.2, V_S is the voltage supplied to the bridge, and V is the voltage across the bridge. Then, the resistance of the wire was converted to the temperature change of the wire by,

$$\Delta T(t) = \frac{R_W(t) - R_W(0)}{\kappa R_W(0)} \tag{3.7}$$

where κ is the temperature coefficient of the electrical resistivity of mercury. Lastly, the average heat dissipated in the wire per unit length, q, is calculated from Joule's first law,

$$q = \frac{I^2 R_{Wav}}{L} = \frac{V_S^2 R_{Wav}}{(R_D + R_{Wav})^2 L} \tag{3.8}$$

where I is the current flow through the wire, L is the length of the wire, and R_{Wav} is the average resistance of the wire. The heat dissipated per unit length and the slope of the linear relationship between ΔT and ln (t) are all that are needed to determine the thermal conductivity using equation 3.5 if all of the assumptions are assumed to be correct. However, some assumptions create significant error in the thermal conductivity measurement. Some of these errors can be corrected theoretically, and others can only be corrected through calibration.

3.4.3 Corrections and Calibration

The thermal conductivity is calculated from the temperature versus time response of an ideal system using equation 3.5. The ideal temperature change ΔT_{id} is obtained by adding theoretical corrections to the measured temperature change of the wire,

$$\Delta T_{id}(t) = \Delta T(t) + \sum_i \delta T_i(t) \tag{3.9}$$

where δT_i are corrections to the temperature change.

3.4.3.1 Insulating Layer and Three Dimensional Aspect of Wire

The analysis in the previous section is based on a one dimensional linear heat source immersed in a fluid. The radius of the wire, and the radius and physical properties of the pyrex capillary were not considered in the model. Nagasaka and Nagashima [101] derived the following expression to account for the temperature correction caused by the insulating pyrex layer and for the three dimensional aspect of the wire:

$$\delta T_1(t) = \frac{-q}{4\pi k}\left\{2\ln\left(\frac{r_i}{r_o}\right) + \frac{2k}{k_G}\ln\left(\frac{r_o}{r_i}\right) + \frac{k}{2k_{Hg}} + \frac{1}{t}\left[C_1 + C_2 + C_3\ln\left(\frac{4\alpha t}{r_o^2\gamma}\right)\right]\right\} \tag{3.10}$$

$$C_1 = \frac{r_i^2}{8}\left[\left(\frac{k-k_G}{k_{Hg}}\right)\left(\frac{1}{\alpha_{Hg}} - \frac{1}{\alpha_G}\right) + \frac{4}{\alpha_G} - \frac{2}{\alpha_{Hg}}\right]$$

$$C_2 = \frac{r_o^2}{2}\left(\frac{1}{\alpha} - \frac{1}{\alpha_G}\right) + \frac{r_i^2}{k_G}\left(\frac{k_G}{\alpha_G} - \frac{k_{Hg}}{\alpha_{Hg}}\right)\ln\left(\frac{r_o}{r_i}\right)$$

$$C_3 = \frac{r_i^2}{2k}\left(\frac{k_G}{\alpha_G} - \frac{k_{Hg}}{\alpha_{Hg}}\right) + \frac{r_o^2}{2k}\left(\frac{k}{\alpha} - \frac{k_G}{\alpha_G}\right)$$

where r_i and r_o are the inner and outer radii of the capillary, respectively, t is time, k is the thermal conductivity, α is the thermal diffusivity, and γ is the exponential of Euler's

constant. The subscripts *Hg* and *G* refer to properties of mercury and borosilicate glass, respectively, while properties with no subscript refer to the fluid. The magnitude of this correction is strongly dependent on the geometry of the capillary and can cause as much as 10 % error in the thermal conductivity measurement if omitted.

3.4.3.2 Finite Extent of the Liquid

Equation 3.3 is based on an infinite volume of liquid to act as a heat sink. The following expression was derived by Healy et al. [100] to calculate the magnitude of this error:

$$\delta T_2(t) = \frac{q}{4\pi k}\left[\ln\left(\frac{4\alpha t}{b^2\gamma}\right) + \sum_{\nu=1}^{\infty}\exp\left(\frac{-g_\nu^2\alpha t}{b^2}\right)\left[\pi Y_0(g_\nu)\right]^2\right] \tag{3.11}$$

where b is the inside diameter of the cell, Y_0 is the zero-order Bessel function of the second kind, and g_ν are the roots of J_0, the zero-order Bessel function of the first kind. The magnitude of this correction was calculated during each measurement to ensure the assumption caused negligible error. In the present work, this correction was insignificant (< 0.1 %).

3.4.3.3 Heat Transfer by Radiation

Nieto de Castro et al. [112] developed the following equation to determine the amount of heat transfer by radiation during the measurement:

$$\delta T_3(t) = \frac{-qB}{4\pi k}\left[\frac{r_i^2}{4\alpha}\ln\left(\frac{4\alpha t}{r_i^2\gamma}\right) + \frac{r_i^2}{4\alpha} - t\right] \tag{3.12}$$

where B is a radiation parameter. This parameter was determined from the following equation after the first two temperature corrections are made:

$$\Delta T_{id}(t) = \frac{q}{4\pi k}\left(1 + \frac{Br_i^2}{4\alpha}\right)\ln\left(\frac{4\alpha t}{r_i^2 \gamma}\right) + \frac{Bqr_i^2}{16\pi\alpha k} - \frac{Bqt}{4\pi k} \tag{3.13}$$

This correction was also insignificant for data measuremed in this study (< 0.1 %).

3.4.3.4 Calibration

There are two sources of error that can not be accounted for theoretically. The first is the non-uniform diameter of the capillary. The capillary was produced by heating and stretching the borosilicate glass, which creates a capillary of varying thickness along its length. In the preceding analysis, the average inner and outer diameters of the wire were used in the calculations. Those values were approximated by examining the capillary under a microscope. However, the use of an average wire diameter did not eliminate this source of error. During Joule heating, a wire of varying diameter is analogous to a series of resistors with varying resistance, which causes different levels of heat dissipation along the length of the wire.

Secondly, axial heat conduction was not considered in any of the previous calculations. The analysis was based on all heat conducting radially through the wire, glass and fluid, since the model is of an infinite wire with no ends. The real system was designed to minimize end effects, but they are not eliminated. Despite far less heat transfer area, a small amount of heat is conducted axially in the mercury wire because there is much less resistance to heat transfer through the mercury at the end of the wire than through the borosilicate glass. De Groot et al. [113] solved this problem for the bare platinum wire by constructing an instrument from two wires of the same diameter but different lengths. DiGuilio and Teja [110] extended this method to the liquid metal transient hot wire method. The end effects would be similar in both of these wires and

would effectively offset each other. The system would then be modeled as a single wire with a length equal to the difference between the two wires. The differential method requires that both wires be the same diameter, and that the insulation for each wire have the same thickness. The differential method was not used in this work because of the difficulty with producing capillaries of different lengths but equal diameters.

There is no analytical correction available for either of these sources of error. However, calibration of the apparatus was used to compensate for these errors. By measuring a reference fluid with a well known thermal conductivity, an effective wire length was calculated. The effective wire length determined during the calibration was then used for subsequent measurements and provides accurate results for various liquids, temperatures, and pressures, since these errors are primarily dependent on the geometry of the wire. To validate this approach, the thermal conductivity of another reference fluid was measured as a function of temperature. Bleazard and Teja [104] used this approach to show that overall the error was < 2 % using this method.

3.5 Calibration of Updated Instrument

The effective length of the wire was adjusted to calibrate the updated apparatus. Two other parameters were considered in the calibration experiment. First, the voltage supplied to the bridge had to be selected since this directly determines the temperature rise in the wire. Since the voltage supplied to the bridge was constant, a higher voltage leads to a greater temperature rise in the wire. If the voltage is too low, the noise in the data becomes more significant and leads to lower resolution in the experimental measurement. However, if the voltage is too large, convection may occur during the measurement due to a larger temperature rise in the wire. A precise optimization was

unnecessary for this parameter. However, it is most important to operate within a range that avoids both of these problems for the variety of fluids to be studied. For this research, a value of 4 V was chosen based on several trials.

The second parameter is the time period corresponding to the linear portion of the ΔT vs ln(t) relationship, which was determined through calibration. Time periods of 1, 1.5, 2, and 2.5 seconds were considered. At 1 second, the variation between measurements was greater than at larger time periods. However, as the time period increased, there was a greater change in temperature and therefore in the physical properties of the fluid, which caused an increasingly larger change in the slope. For this reason, 1.5 seconds was selected as the time period for the experiment. The specific time corresponding to the beginning of the linear portion was then selected. This value along with the effective wire length was determined during the calibration with reference fluids water [23] and dimethyl phthalate [114]. Calibration data are presented in Figure 3.4 for dimethyl phthalate at 73 ºC. The same data were collected for this fluid at 24, 117, and 145 ºC and for water at 24, 59, and 84 ºC. At least five measurements were performed for each set of conditions. For water above 84 ºC, convection occurred and the data were not considered in the calibration. The individual measurements were averaged to obtain a single curve corresponding to a specific fluid at one temperature. From these seven curves, the average and standard deviation were found for each time period and displayed in Figures 3.5 and 3.6, respectively. The effective length and time period were selected that produced the minimum standard deviation. The standard deviation reached a minimum value of 0.055 cm for the time period of 0.88 to 2.38 seconds with a

corresponding effective length of 9.9 cm. A plot of residuals of the effective mean is presented in Figure 3.7.

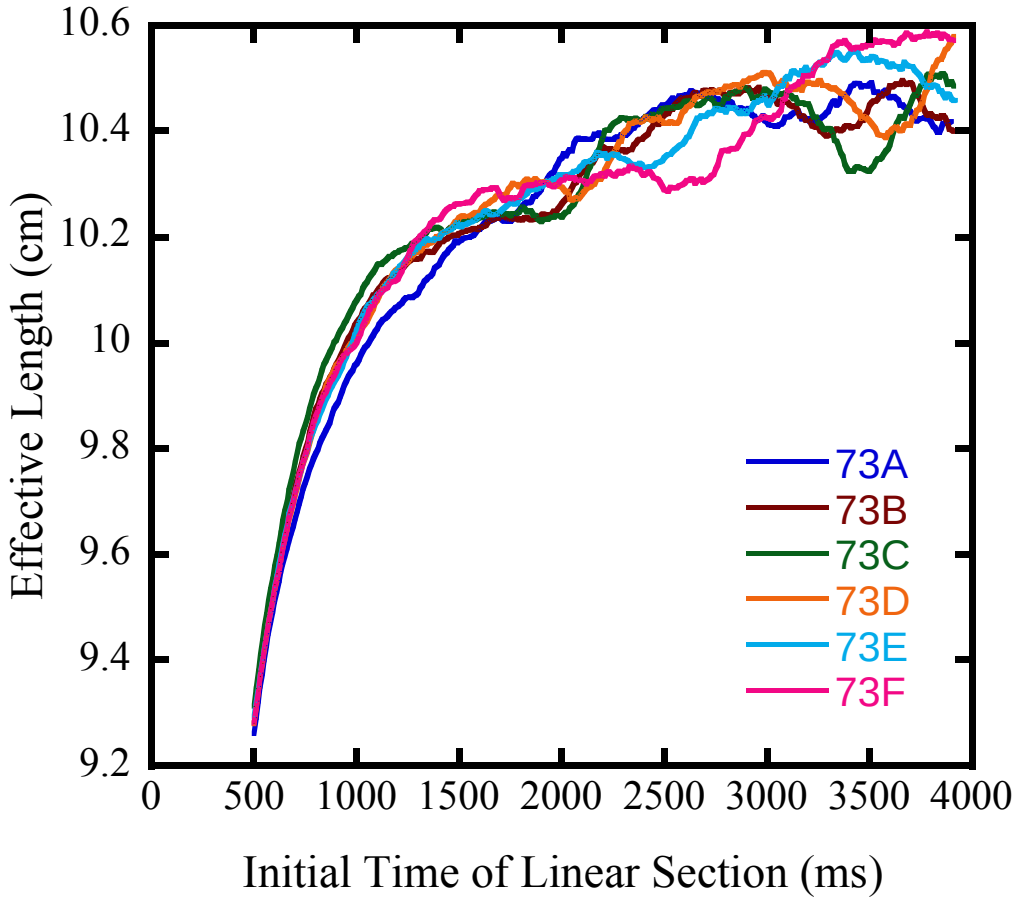

Figure 3.4 Multiple calibrations of the effective length of the hot wire with dimethyl phthalate (DMP) at 73 ºC as a function of the time period.

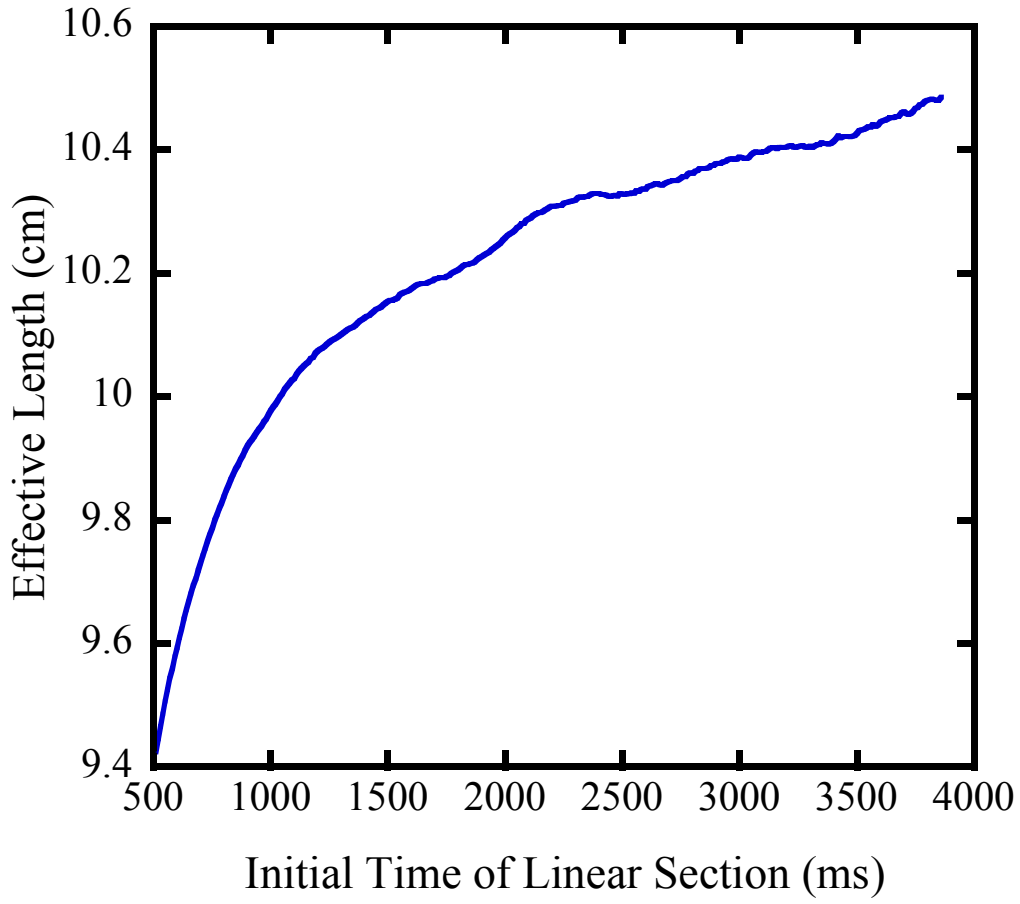

Figure 3.5 The mean effective length as a function of the time period determined from each measurement of water and dimethyl phthalate at all temperatures

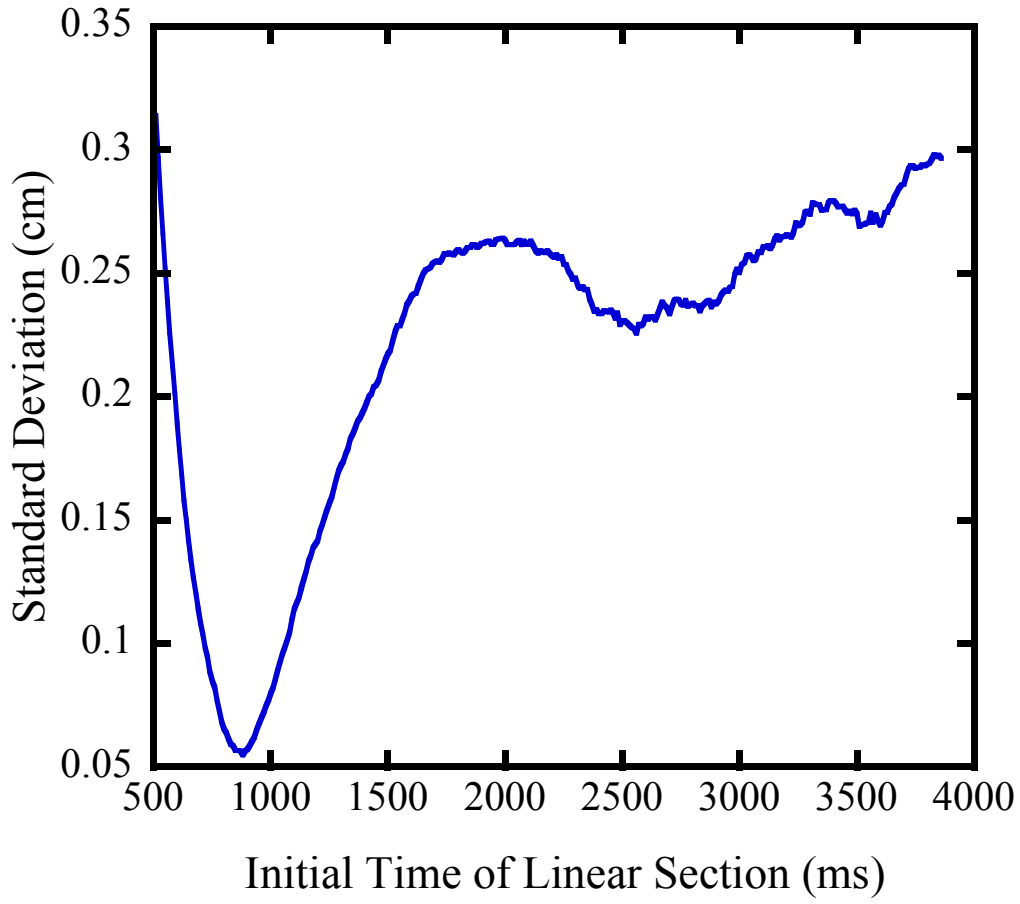

Figure 3.6 The standard deviation of the effective wire length as a function of the time period analyzed.

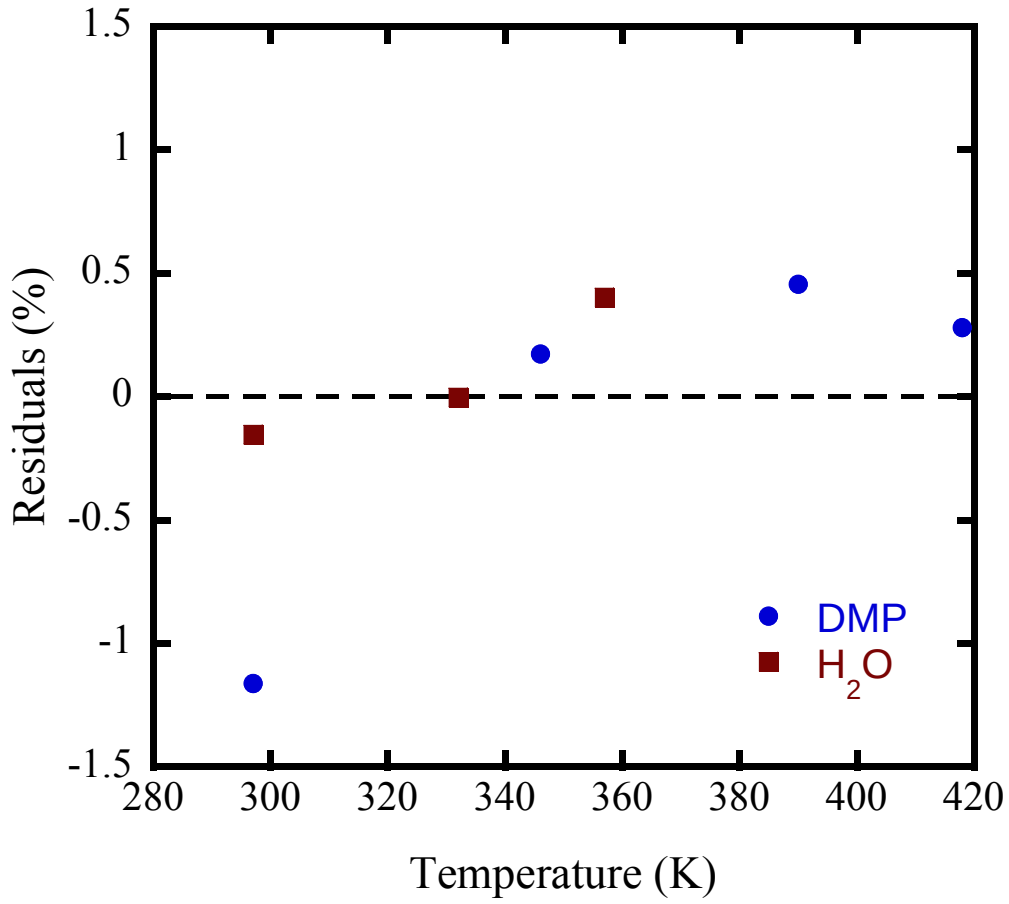

Figure 3.7 Residuals of the effective wire length for water and dimethyl phthalate at various temperatures

3.6 Validation of Updated Instrument

Ethylene glycol was used to validate the transient hot wire apparatus because it is one of the base fluids considered in this study. Table 3.1 contains a comparison of the measured thermal conductivity and reference values [115] at three temperatures. Each reported measured value is the average of at least 5 measurements. The error for the reference data is reported to be less than 5 %, and measured values from this work are within 2 % of the reported values.

A heterogeneous system was also selected to validate the instrument for nanofluid samples. An aqueous nanofluid containing alumina was selected due to the large amount of data available for this system in the literature. Six thermal conductivity data sets [8, 13, 50, 52, 57, 58] are available for this system containing 0 – 5 % (v/v) alumina nanoparticles with average particle diameters between 38 – 50 nm at room temperature. Moreover, these six sets of data are in general agreement with each other within 1.5 %. The measurements in this study for the aqueous nanofluid sample containing alumina (46 nm diameter) compare favorably with the results from the literature as illustrated in Figure 3.8. The measured values in this study were within 1.1 % of a linear fit to the literature values, which is well within the 2 % reported accuracy of this method.

Table 3.1 Validation of transient hot wire apparatus with ethylene glycol

Temperature (K)	298.0	323.9	352.4
k_{exp} (W m^{-1} K^{-1})	0.257	0.260	0.264
k_{ref} (W m^{-1} K^{-1}) [115]	0.254	0.257	0.258
% error	1.36 %	1.02 %	1.85 %

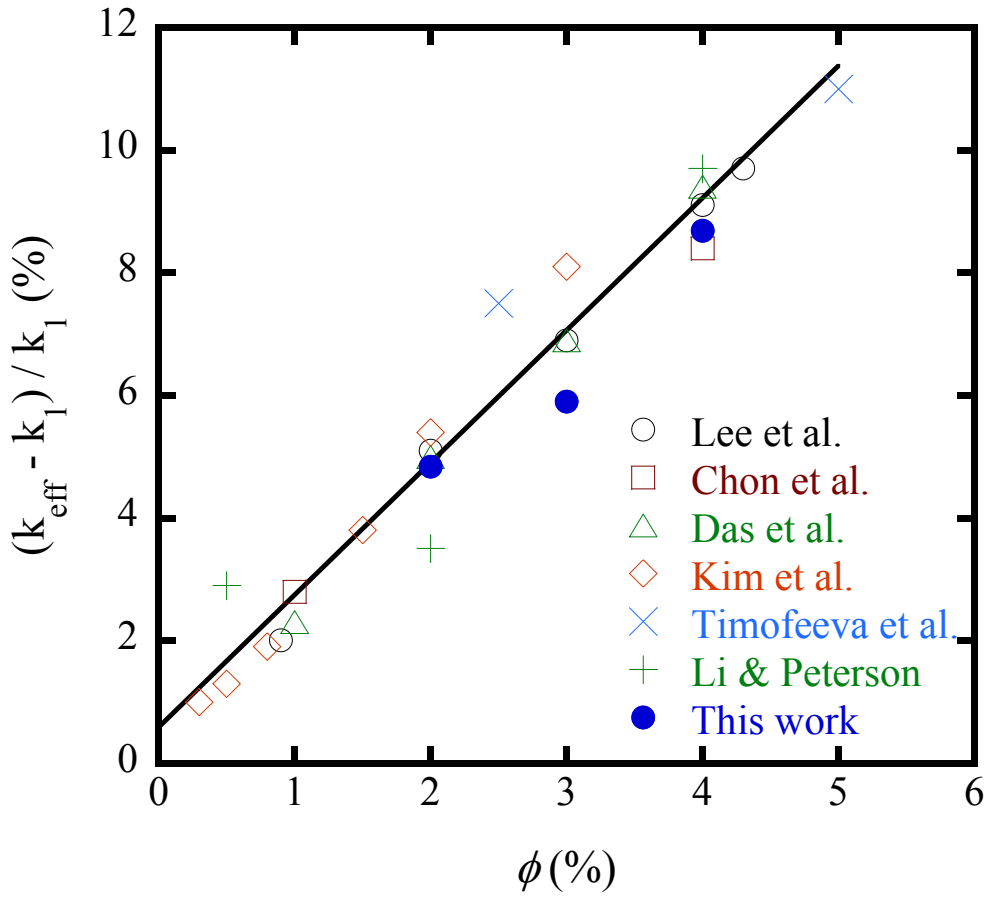

Figure 3.8 Thermal conductivity enhancement of aqueous alumina nanofluids. The solid circles (●) represent measurements from this study (47 nm diameter alumina), and the others represent data from the literature (38 – 50 nm diameter alumina) [8, 13, 50, 52, 57, 58].

CHAPTER 4

THERMAL CONDUCTIVITY MEASUREMENTS AND CHARACTERIZATION OF SOLID / LIQUID DISPERSIONS

The focus of this work is on the thermal conductivity of dispersions containing metal oxides in electrically conducting liquids. This chapter describes the systems that were studied and the results of the thermal conductivity measurements as well as methods for characterization of the nanofluids.

4.1 Materials and Methods

4.1.1 Materials

Nanofluids were prepared using alumina, ceria, or titania particles in deionized water, ethylene glycol, or a mixture of the two. The resistivity of the pure deionized water was greater than 18 MΩ·cm, and the ethylene glycol was reagent grade (99.0 %) from VWR International (West Chester, PA). The particles were obtained from different vendors as dry powders. Sources are listed in Table 4.1 together with the crystal phase and average particle size reported by the manufacturer.

Commercial nanofluids were supplied by NEI Corporation (Somerset, NJ) and are listed in Table 4.2. Each of these nanofluids contained a proprietary dispersant.

Table 4.1 Sources of Alumina and Ceria powders and their properties provided by the manufacturer

Manufacturer (Product Name)	Crystal Phase & Material	Average Particle Diameter (nm)
Electron Microscopy Sciences	γ - Al_2O_3	50
Electron Microscopy Sciences	α - Al_2O_3	300
Electron Microscopy Sciences	α - Al_2O_3	1000
Nanophase (NanoTek)	δ/γ - Al_2O_3	47
Nanostructured and Amorphous Materials	γ - Al_2O_3	11
Nanostructured and Amorphous Materials	γ - Al_2O_3	20
Nanostructured and Amorphous Materials	α-Al_2O_3	150
Nanostructured and Amorphous Materials	CeO_2	15 - 30
Nanostructured and Amorphous Materials	CeO_2	70 - 100

Electron Microscopy Sciences (Hatfield, PA)
Nanophase (Romeoville, IL)
Nanostructured and Amorphous Materials (Los Alamos, NM)

Table 4.2 Nanofluids provided by NEI Corporation (Somerset, NJ)

Particle Material	Average Particle Diameter (nm)	Base Fluid	Volume Fractions
γ - Al_2O_3	50 nm	Water	1.4, 2.9, 4.6 %
γ - Al_2O_3	50 nm	50 % (w/w) Water + Ethylene Glycol	0.5, 1, 2, 3, 4 %
γ - Al_2O_3	10 nm	50 % (w/w) Water + Ethylene Glycol	0.5, 1, 2, 3 %
TiO_2	2 nm	50 % (w/w) Water + Ethylene Glycol	2, 4, 6, 8.5 %

4.1.2 Sample Preparation

Nanofluid samples were prepared by dispersing pre-weighed quantities of dry particles in either deionized water or ethylene glycol. The pH of each aqueous mixture was measured and, if necessary, was adjusted to 4.0 ± 0.2 by the addition of HCl to promote dispersion. The mixtures were then subjected to ultrasonic mixing (Sonics & Materials, Inc. Vibra-Cell VCX 750) for several minutes to break up any particle aggregates. The acidic pH is much less than the isoelectric point of these particles (7-9 for alumina [116] and 6.7-8.7 for ceria [117]), thus ensuring a positive surface charge on the particles. The surface charge enhanced repulsion between the particles, which resulted in uniform dispersions for the duration of the experiments. An image of an aqueous nanofluids containing alumina is displayed in Figure 4.1

Figure 4.1 Aqueous nanofluid containing 3 % (v/v) alumina particles

4.2 Nanofluid Characterization

4.2.1 Primary Particle Size

Average particle sizes provided by the manufacturer are typically determined by surface area measurements of the dry powder. However, different lots of particles may have different sizes, and this measurement provides no information regarding the size distribution of particles. Thus, transmission electron microscopy (TEM) was employed to obtain images of each type of alumina particle, and surface area measurements were performed to determine the average particle size.

TEM images were obtained using a Hitachi (Pleasanton, CA) HF-2000 transmission electron microscope. TEM samples were prepared by diluting a small amount of a nanofluid sample (approximately 10:1) and placing a few drops on the TEM grid and allowing it to dry for 24 hours.

The Brunauer – Emmett – Teller (BET) surface areas were obtained from nitrogen adsorption data measured by an Accelerated Surface Area and Porosity (ASAP 2020) system from Micromeritics (Norcross, GA). The samples were degassed before the measurements by ramping the temperature up to 300 ºC at a rate of 10 ºC / min and held at that temperature for 100 minutes. Afterwards, free space in the sample tube was measured using the analysis port of the ASAP 2000. The sample was then degassed by heating to 300 ºC under vacuum for at least 4 hours. The BET surface areas were calculated from P / P_0 data between 0.05 and 0.30, where P and P_0 are the equilibrium and saturation pressures of nitrogen, respectively.

The average particle diameter was determined from the specific surface area and an estimate of the shape of the particles obtained from the TEM images. All of the

particles were either spherical or ellipsoidal (sphericity > 0.9). Estimates of the average and standard deviation of the particle diameter were obtained by measuring individual particles in the TEM images. The images display aggregates consisting of many particles, which make it difficult to differentiate individual particles. Therefore, only ten particles were considered from each image. Examples of these images are displayed in figures 4.2 and 4.3. The remaining images are shown in Appendix C. Table 4.3 displays the average particle diameters obtained from both the surface area measurements and the TEM images. The large differences between a few of the particle samples can be attributed to the polydispersity of those samples (Figure 4.2). The surface area measurements provide a more accurate mean than the TEM images due to the extremely small sample size considered in the analysis of TEM images. Therefore, only the diameters obtained from the surface area measurements are considered in the analysis of thermal conductivity results. Only two samples of ceria were used in this study, thus surface area measurements were sufficient without TEM imaging to demonstrate the difference in size. The average particle size of the ceria was calculated assuming spherical particles.

4.2.2 Secondary Particle Size

Particles in each sample were aggregated to some degree, which can be seen in the TEM images. The aggregate size is also referred to as the secondary particle size and is important in determining the stability of the dispersion. It is this size which determines the Brownian velocity of particles in a liquid. An average hydrodynamic radius can be calculated by measuring the velocity of the aggregates with dynamic light scattering. The measurement is only valid for transparent or nearly transparent samples, so the technique

is not appropriate for the concentrations used in this work (0.5 – 5.0 %). Aqueous samples were prepared as stated previously, and then a portion was diluted until the liquid was transparent. The level of dilution was adjusted so that a similar average count rate was achieved in each measurement. The measurements were performed with a 90Plus particle size analyzer from Brookhaven Instruments Corporation (Holtsville, NY). The samples were measured at room temperature. Two runs were performed on each sample, and each run lasted 2 minutes at a measurement rate of 1 per second. The results are displayed in Table 4.3 and are presented as hydrodynamic diameters for consistency.

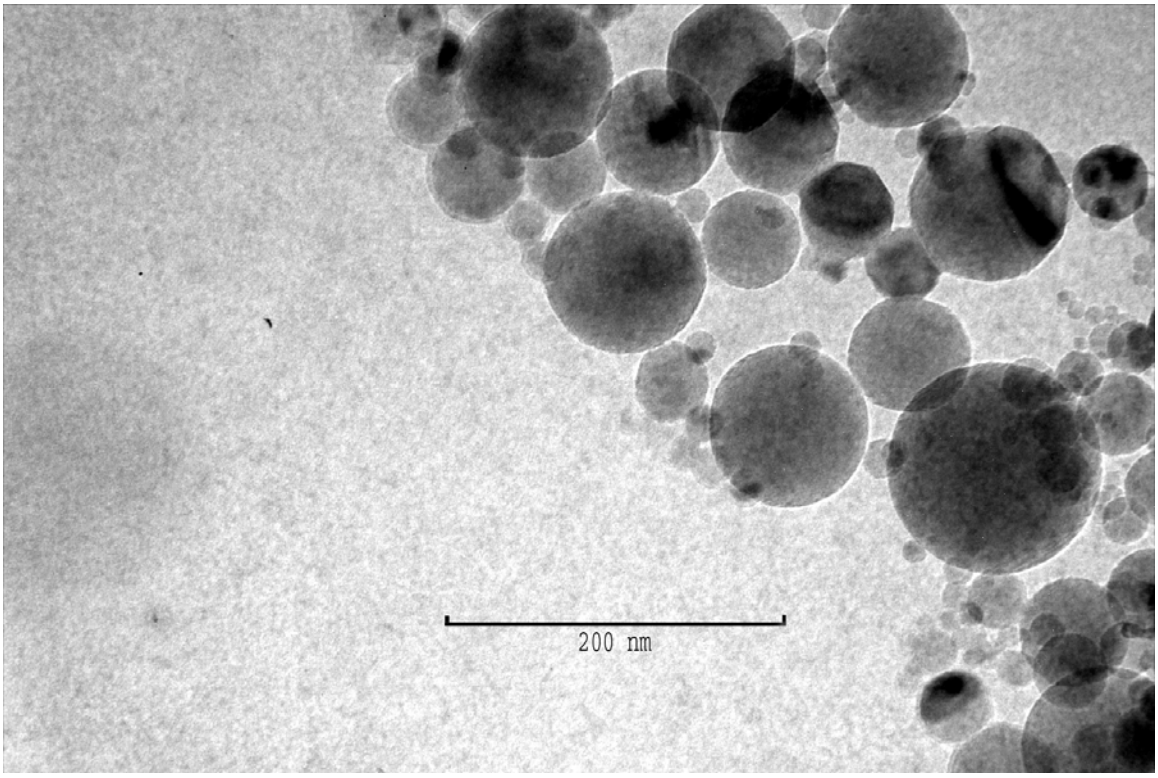

Figure 4.2 Transmission electron microscopy image of alumina particles with a nominal size of 47 nm from Nanophase Technologies (Romeoville, IL). The average diameter of these particles is 77 nm and 46 nm as determined by TEM and BET, respectively. Magnification = 100,000

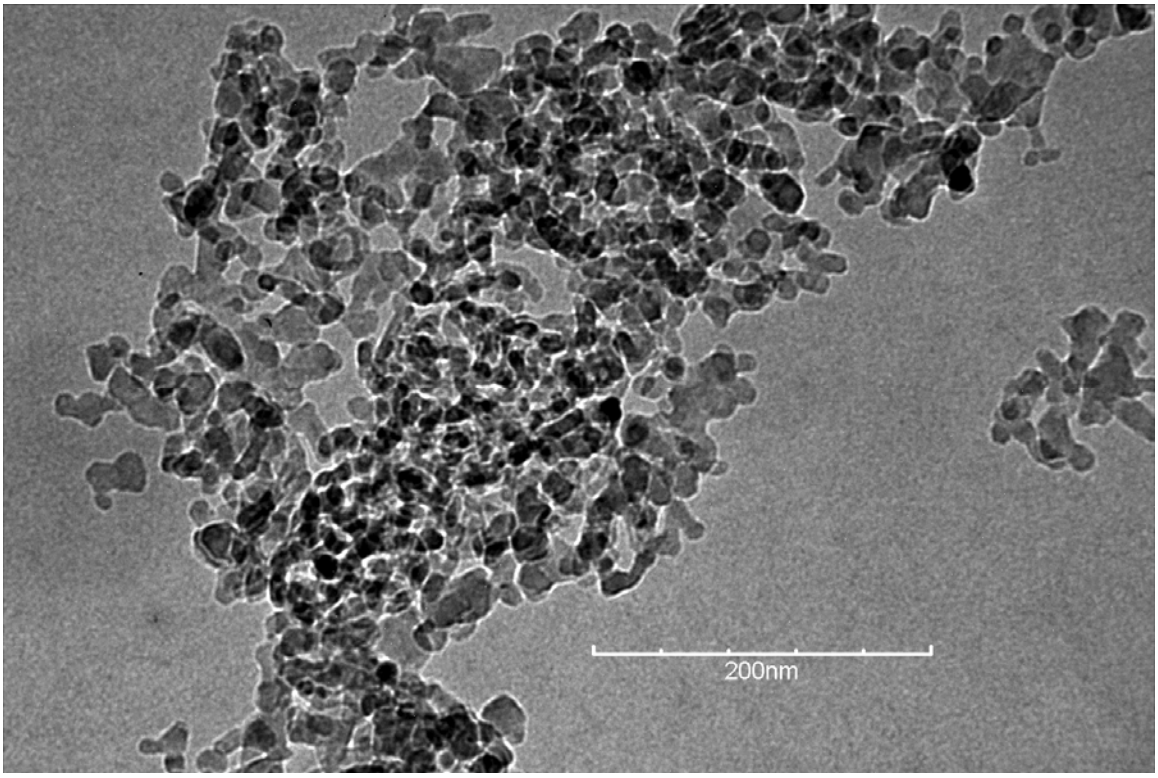

Figure 4.3 Transmission electron microscopy image of alumina particles with a nominal size of 50 nm from Electron Microscopy Sciences (Hatfield, PA). The average diameter of these particles is 20 nm and 16 nm as determined by TEM and BET, respectively Magnification = 100,000

Table 4.3 Mean primary and secondary particle sizes (nm) of powders dispersed in water from specific surface area measurements, transmission electron microscopy, and dynamic light scattering

Material	Particle Diameter from Manufacturer	Particle Diameter from BET	Tranmission Electron Microscopy			Hydrodynamic Diameter
			Diameter	Standard Deviation	Coefficient of Variation	
Al_2O_3	11	8	6	2	33 %	320
Al_2O_3	20	12	10	2	20 %	265
Al_2O_3	47	46	77	110	140 %	205
Al_2O_3	50	16	20	5	25 %	520
Al_2O_3	150	245	180	38	21 %	790
Al_2O_3	300	71	99	95	96 %	492
Al_2O_3	1000	282	290	51	18 %	522
CeO_2	15 – 30	12	NA	NA	NA	280
CeO_2	70 – 100	74	NA	NA	NA	550

4.3 Thermal Conductivity Measurements

4.3.1 Temperature Studies

The thermal conductivity of nanofluids of specific mass fractions is presented in Tables 4.4 - 4.9 and Figures 4.4 – 4.9. Each data point represents the average value of five thermal conductivity measurements. Standard deviations for each series of measurements are also provided. The measurements were made at temperatures ranging from 294 K to 422 K using the original transient hot wire instrument constructed by Bleazard and Teja [104], after the sample was allowed to come to thermal equilibrium at each temperature for no less than 30 minutes. The samples consisted of 12 nm alumina nanoparticles dispersed in water and in ethylene glycol, and the nanofluids provided by NEI listed in Table 4.2. Note that for each mass fraction, the volume fraction decreases with temperature since the density of the liquid phase decreases with temperature. Thus, the volume fractions listed in the figures refer to the volume fraction at room temperature.

The nanofluids containing ethylene glycol (Figure 4.4) and the ethylene glycol and water mixture (Figures 4.7 and 4.8) clearly display curvature in the thermal conductivity – temperature relationship. Furthermore, the maximum thermal conductivity occurs at approximately the same temperature as the base liquid. This relationship may be valid in aqueous nanofluids (Figures 4.5 and 4.6), but this cannot be stated unambiguously since the thermal conductivity maximum for water occurs at a temperature (~ 403 K) near the maximum temperature measured in this work (~ 422 K). At temperatures greater than 422 K, convection was evident during the measurement, which invalidated those measurements. Figure 4.5 displays a comparison of the thermal

conductivities for aqueous data from this work and from Das et al. [8]. Their data lies at the lower temperature range of this work (< 320 K), but the thermal conductivity data displays a stronger temperature dependence than observed in this work. This work and the data from Das et al. appear to exhibit a linear relationship between thermal conductivity and temperature below 320 K.

The nanofluids containing TiO_2 nanoparticles exhibited a lower thermal conductivity than the ethylene glycol and water mixtures (Figure 4.9). Furthermore, the thermal conductivity of the nanofluids decreased as the volume fraction increased. This suppression of the thermal conductivity with the addition of nanoparticles to a liquid has not been observed previously in the literature.

Table 4.4 Thermal conductivity of ethylene glycol nanofluids containing Al_2O_3

Mass fraction of Al_2O_3	T (K)	Volume fraction of Al_2O_3	Mean k W m^{-1} K^{-1}	Standard Deviation
3.26 %	302.0	1.00 %	0.258	0.004
3.26 %	323.4	0.98 %	0.259	0.004
3.26 %	347.3	0.97 %	0.262	0.001
3.26 %	372.2	0.95 %	0.267	0.003
3.26 %	392.4	0.94 %	0.264	0.002
3.26 %	411.1	0.92 %	0.260	0.002
9.34 %	296.3	3.00 %	0.276	0.003
9.34 %	323.6	2.95 %	0.282	0.002
9.34 %	349.0	2.90 %	0.284	0.005
9.34 %	373.3	2.85 %	0.285	0.005
9.34 %	392.1	2.81 %	0.287	0.003
9.34 %	409.6	2.78 %	0.280	0.007
12.2 %	304.0	3.99 %	0.290	0.005
12.2 %	323.7	3.94 %	0.291	0.005
12.2 %	348.5	3.87 %	0.294	0.003
12.2 %	373.3	3.81 %	0.293	0.006
12.2 %	391.0	3.76 %	0.288	0.007
12.2 %	409.0	3.71 %	0.285	0.007

Table 4.5 Thermal conductivity of aqueous nanofluids containing Al_2O_3

Mass fraction of Al_2O_3	T (K)	Volume fraction of Al_2O_3	Mean k W m^{-1} K^{-1}	Standard Deviation
3.61 %	297.2	1.00 %	0.625	.014
3.61 %	321.6	0.99 %	0.641	.017
3.61 %	345.5	0.98 %	0.653	.011
3.61 %	371.1	0.96 %	0.670	.007
3.61 %	396.9	0.94 %	0.678	.005
10.3 %	298.7	3.00 %	0.636	.014
10.3 %	322.3	2.97 %	0.646	.009
10.3 %	346.9	2.94 %	0.674	.010
10.3 %	371.4	2.89 %	0.680	.006
10.3 %	391	2.85 %	0.696	.013
10.3 %	410.9	2.80 %	0.687	.010
16.3 %	302.3	4.99 %	0.650	.011
16.3 %	324.4	4.95 %	0.671	.005
16.3 %	348.3	4.89 %	0.685	.006
16.3 %	368.6	4.82 %	0.712	.006
16.3 %	391.9	4.74 %	0.720	.011

Table 4.6 Thermal conductivity of aqueous nanofluids containing Al_2O_3 from NEI

Mass fraction of Al_2O_3	T (K)	Volume fraction of Al_2O_3	Mean k W m^{-1} K^{-1}	Standard Deviation
5.00 %	294.4	1.40 %	0.621	0.002
5.00 %	322.2	1.39 %	0.632	0.007
5.00 %	346.6	1.37 %	0.651	0.005
5.00 %	373.5	1.34 %	0.677	0.002
5.00 %	398.0	1.32 %	0.693	0.009
5.00 %	421.5	1.29 %	0.701	0.005
10.0 %	294.9	2.91 %	0.635	0.004
10.0 %	326.0	2.88 %	0.662	0.003
10.0 %	349.5	2.84 %	0.680	0.007
10.0 %	373.0	2.80 %	0.697	0.005
10.0 %	396.1	2.75 %	0.701	0.006
15.0 %	294.9	4.54 %	0.645	0.005
15.0 %	322.2	4.50 %	0.675	0.008
15.0 %	348.7	4.44 %	0.694	0.003
15.0 %	372.7	4.37 %	0.703	0.008
15.0 %	397.3	4.29 %	0.728	0.007

Table 4.7 Thermal conductivity of water + ethylene glycol nanofluids containing Al_2O_3 (50 nm) from NEI

Mass fraction of Al_2O_3	T (K)	Volume fraction of Al_2O_3	Mean k W m^{-1} K^{-1}	Standard Deviation
1.71 %	294.7	0.50 %	0.403	0.002
1.71 %	322.0	0.49 %	0.422	0.003
1.71 %	349.6	0.48 %	0.430	0.004
1.71 %	373.1	0.47 %	0.440	0.002
1.71 %	397.3	0.46 %	0.446	0.003
1.71 %	418.6	0.45 %	0.431	0.005
3.37 %	295.4	1.00 %	0.411	0.003
3.37 %	322.2	0.99 %	0.425	0.003
3.37 %	348.4	0.97 %	0.435	0.006
3.37 %	372.6	0.95 %	0.442	0.003
3.37 %	397.1	0.93 %	0.453	0.003
3.37 %	419.6	0.91 %	0.440	0.009
6.59 %	294.6	2.00 %	0.424	0.004
6.59 %	326.1	1.97 %	0.454	0.004
6.59 %	348.0	1.94 %	0.461	0.005
6.59 %	373.5	1.90 %	0.469	0.005
6.59 %	397.2	1.86 %	0.473	0.004
6.59 %	418.1	1.82 %	0.474	0.008
9.65 %	295.1	3.00 %	0.432	0.004
9.65 %	322.8	2.96 %	0.446	0.004
9.65 %	347.4	2.91 %	0.457	0.002
9.65 %	374.4	2.85 %	0.464	0.003
9.65 %	397.5	2.79 %	0.467	0.003
9.65 %	418.6	2.73 %	0.468	0.002
12.6 %	295.3	4.00 %	0.440	0.002
12.6 %	326.5	3.93 %	0.460	0.009
12.6 %	349.5	3.87 %	0.471	0.005
12.6 %	372.7	3.81 %	0.482	0.004
12.6 %	398.1	3.72 %	0.481	0.002
12.6 %	420.1	3.64 %	0.484	0.004

Table 4.8 Thermal conductivity of water + ethylene glycol nanofluids containing Al_2O_3 (10 nm) from NEI

Mass fraction of Al_2O_3	T (K)	Volume fraction of Al_2O_3	Mean k W m^{-1} K^{-1}	Standard Deviation
1.71 %	296.4	0.50 %	0.403	0.002
1.71 %	324.1	0.49 %	0.414	0.004
1.71 %	348.4	0.48 %	0.429	0.003
1.71 %	372.2	0.48 %	0.435	0.005
1.71 %	397.8	0.46 %	0.441	0.004
1.71 %	422.3	0.45 %	0.438	0.007
3.37 %	296.6	1.00 %	0.413	0.003
3.37 %	324.8	0.98 %	0.431	0.004
3.37 %	348.0	0.97 %	0.438	0.003
3.37 %	373.1	0.95 %	0.447	0.004
3.37 %	397.6	0.93 %	0.457	0.005
3.37 %	421.3	0.91 %	0.449	0.004
6.59 %	296.7	2.00 %	0.423	0.002
6.59 %	315.2	1.98 %	0.438	0.002
6.59 %	333.2	1.96 %	0.451	0.004
6.59 %	353.6	1.93 %	0.458	0.007
6.59 %	372.5	1.90 %	0.464	0.004
9.66 %	296.0	3.00 %	0.429	0.001
9.66 %	313.6	2.97 %	0.445	0.005
9.66 %	333.8	2.94 %	0.456	0.001
9.66 %	353.6	2.90 %	0.468	0.004

Table 4.9 Thermal conductivity of water + ethylene glycol nanofluids containing TiO_2 from NEI

Mass fraction of TiO_2	T (K)	Volume fraction of TiO_2	Mean k W m^{-1} K^{-1}	Standard Deviation
6.59 %	297.3	2.00 %	0.392	0.004
6.59 %	321.3	1.97 %	0.397	0.004
6.59 %	348.0	1.94 %	0.414	0.006
6.59 %	372.9	1.90 %	0.422	0.006
6.59 %	397.0	1.86 %	0.424	0.003
6.59 %	421.2	1.82 %	0.420	0.008
12.6 %	297.6	4.00 %	0.384	0.002
12.6 %	324.4	3.94 %	0.398	0.003
12.6 %	348.3	3.88 %	0.402	0.003
12.6 %	373.4	3.81 %	0.413	0.003
12.6 %	397.4	3.73 %	0.414	0.002
12.6 %	419.0	3.65 %	0.417	0.002
18.1 %	296.8	6.00 %	0.383	0.002
18.1 %	321.9	5.92 %	0.389	0.003
18.1 %	348.5	5.82 %	0.402	0.003
18.1 %	373.7	5.71 %	0.414	0.006
18.1 %	397.4	5.60 %	0.417	0.005
18.1 %	419.0	5.48 %	0.416	0.002
24.3 %	296.8	8.50 %	0.362	0.003
24.3 %	323.7	8.38 %	0.375	0.001
24.3 %	347.9	8.26 %	0.375	0.002
24.3 %	372.7	8.11 %	0.383	0.001
24.3 %	397.3	7.94 %	0.384	0.003
24.3 %	418.6	7.78 %	0.389	0.003

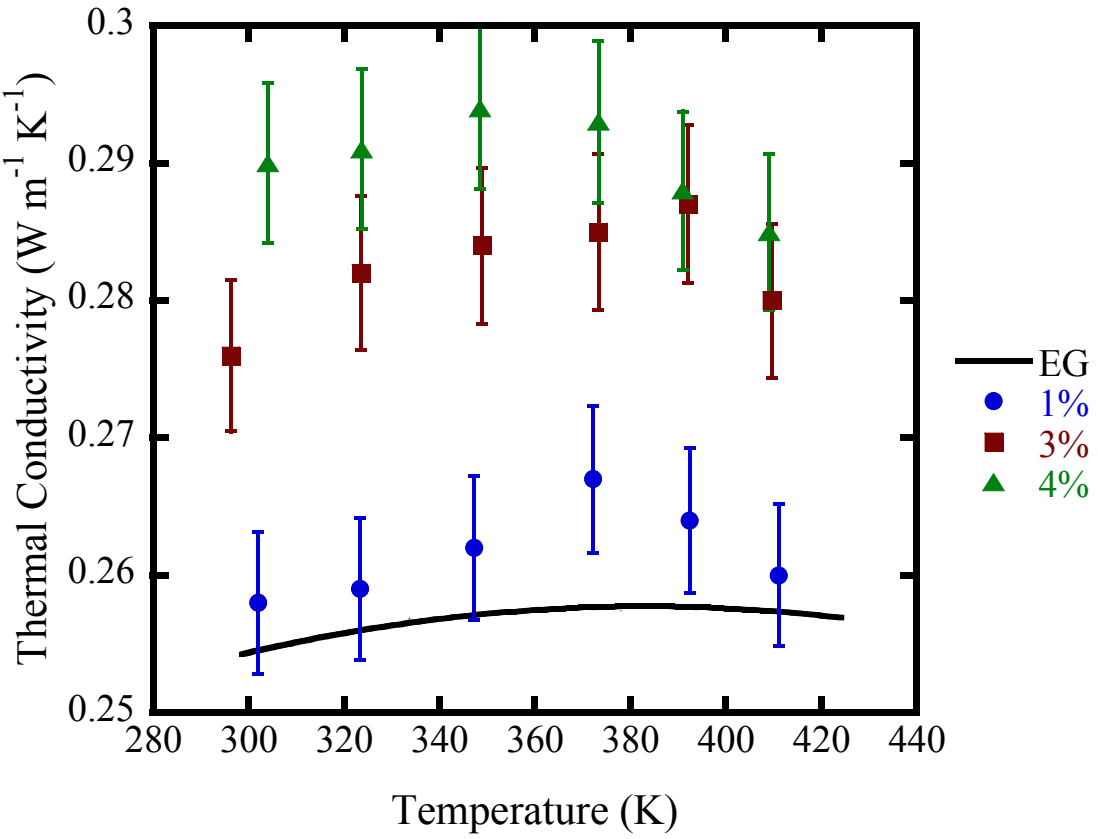

Figure 4.4 Thermal conductivity of ethylene glycol and nanofluids consisting of alumina nanoparticles (diameter = 12 nm) in ethylene glycol. Each data set represents a different volume fraction of alumina (calculated at room temperature). The curve represents the thermal conductivity of ethylene glycol.

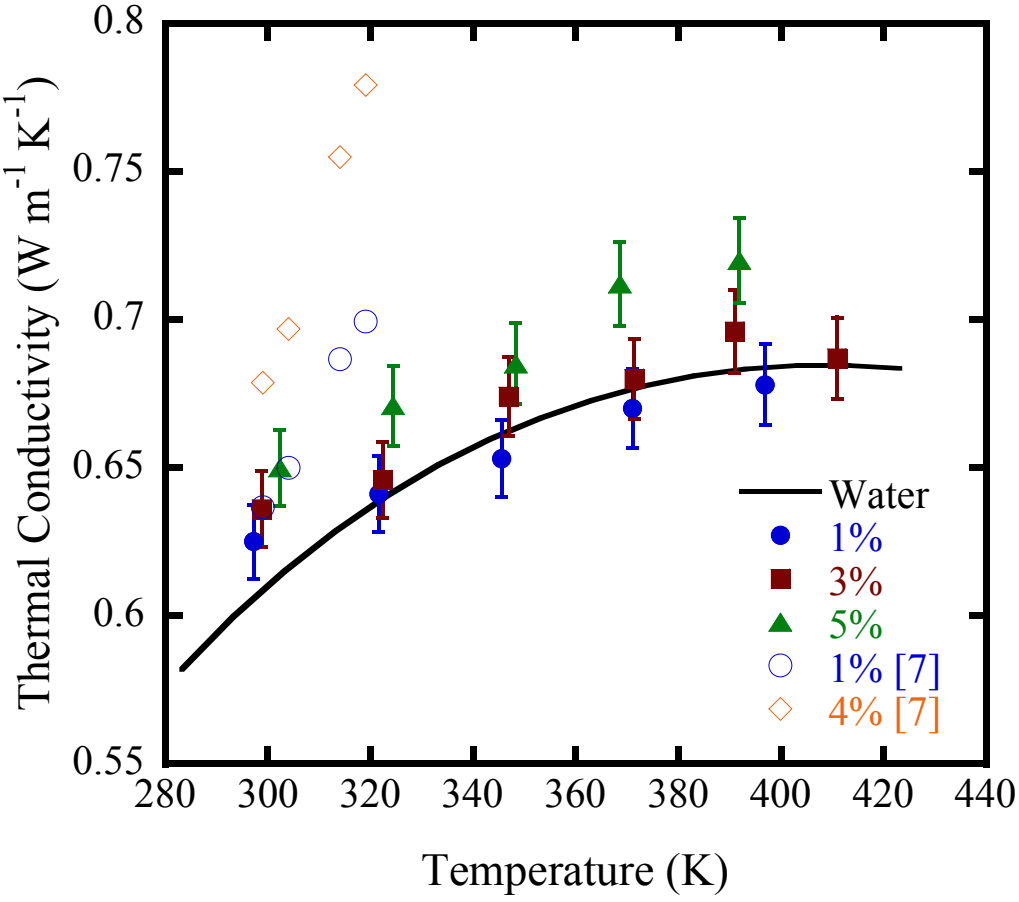

Figure 4.5 Thermal conductivity of water and aqueous nanofluids containing alumina nanoparticles (diameter = 12 nm). Each data set represents a different volume fraction of alumina (calculated at room temperature). The curve represents the thermal conductivity of water. Data of Das et al. [8] is presented for comparison (diameter = 38 nm).

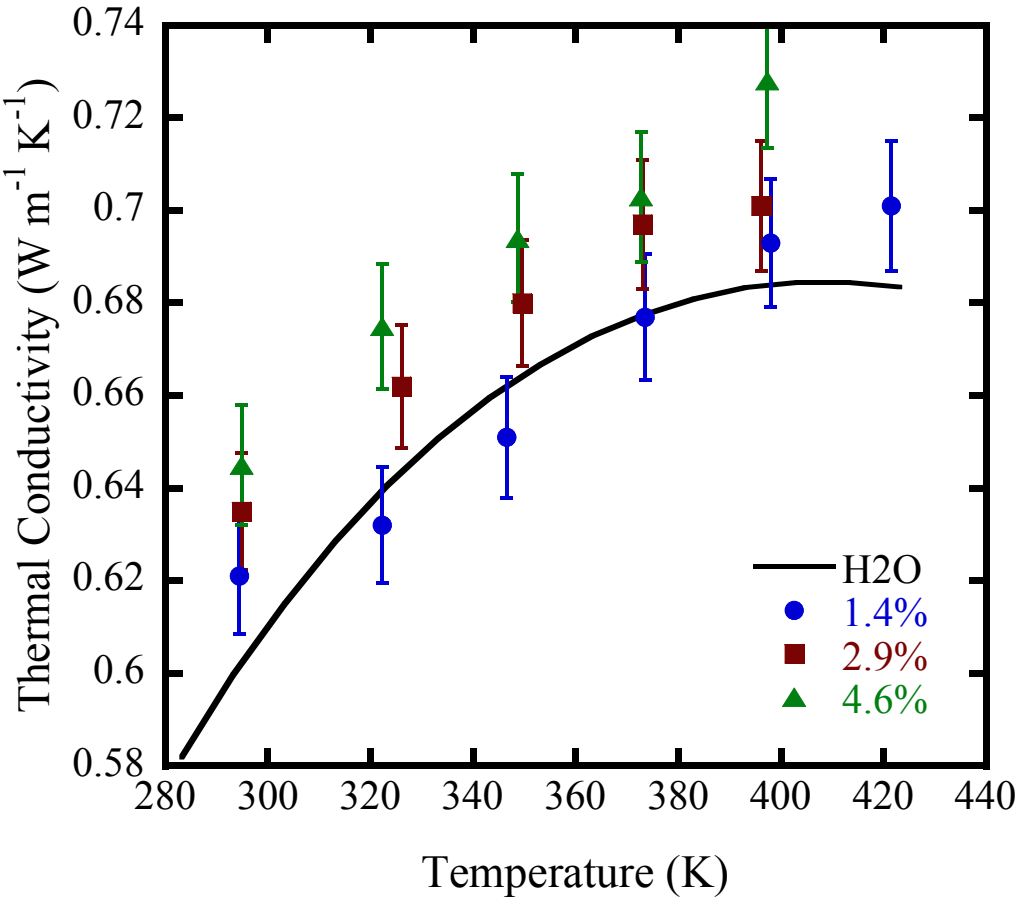

Figure 4.6 Thermal conductivity of water and aqueous nanofluids containing alumina nanoparticles (diameter = 50 nm) with a dispersant. Each data set represents a different volume fraction of alumina (calculated at room temperature). The curve represents the thermal conductivity of water.

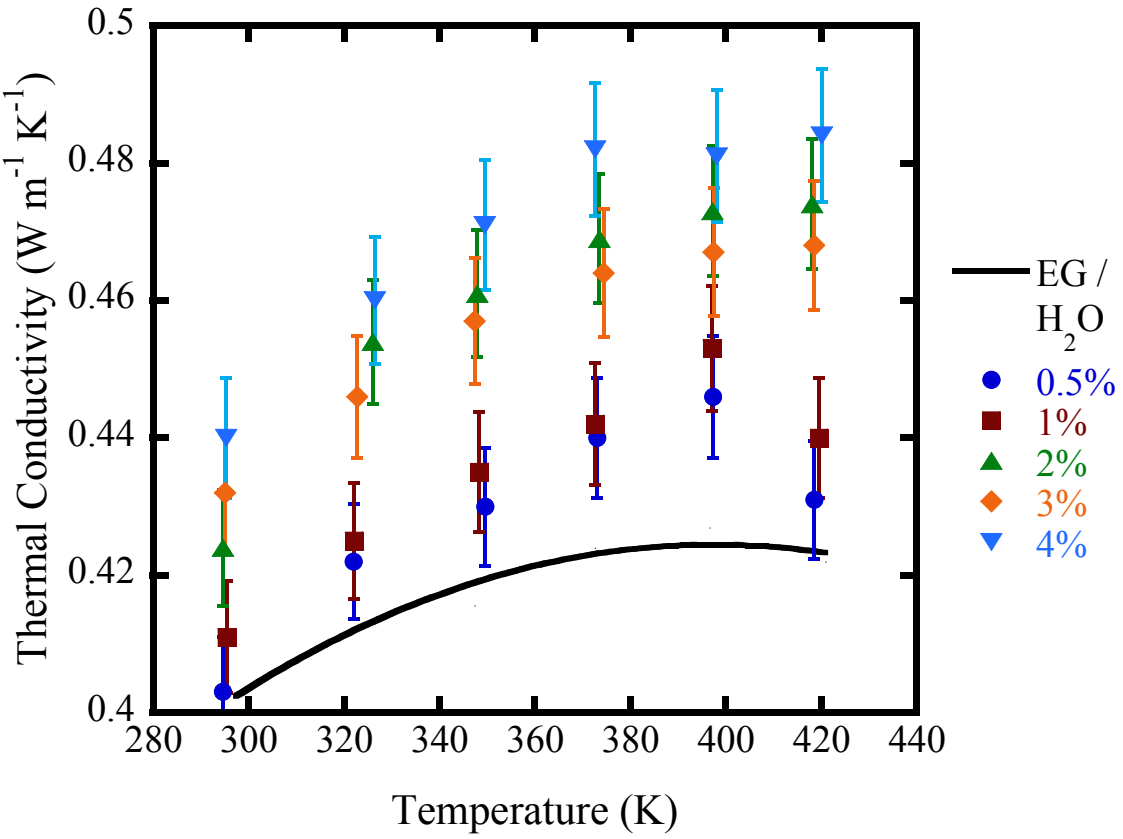

Figure 4.7 Thermal conductivity of a 50 % (w/w) ethylene glycol and water mixture and nanofluids consisting of this mixture and alumina nanoparticles (diameter = 50 nm) with a dispersant. Each data set represents a different volume fraction of alumina (calculated at room temperature). The curve represents the thermal conductivity of the ethylene glycol and water mixture.

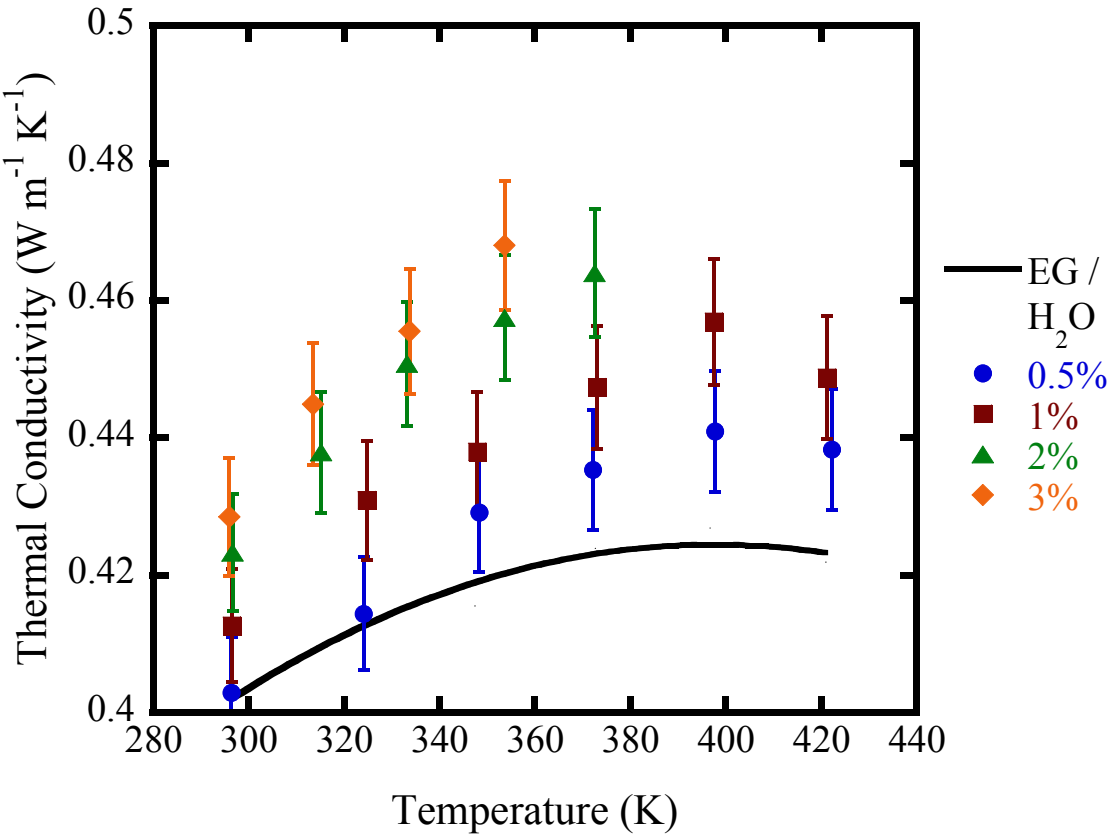

Figure 4.8 Thermal conductivity of a 50 % (w/w) ethylene glycol and water mixture and nanofluids consisting of this mixture and alumina nanoparticles (diameter = 10 nm) with a dispersant. Each data set represents a different volume fraction of alumina (calculated at room temperature). The curve represents the thermal conductivity of the ethylene glycol and water mixture.

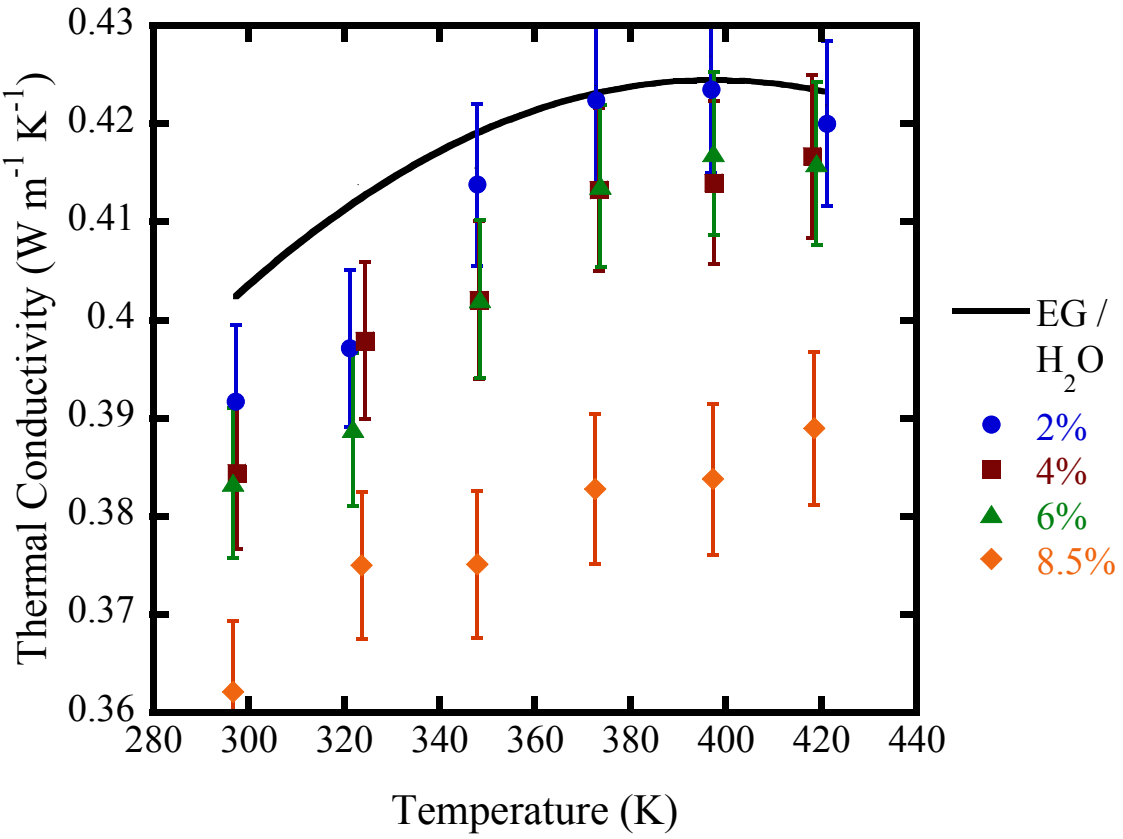

Figure 4.9 Thermal conductivity of a 50 % (w/w) ethylene glycol and water mixture and nanofluids consisting of this mixture and titania nanoparticles (diameter = 2 nm) with a dispersant. Each data set represents a different volume fraction of alumina (calculated at room temperature). The curve represents the thermal conductivity of the ethylene glycol and water mixture.

4.3.2 Particle Size Studies

The thermal conductivity of nanofluids measured at specific mass fractions and particle sizes is presented in Tables 4.10 - 4.12 and Figures 4.10 – 4.13. Each data point represents the average value of at least five measurements. The standard deviations for each series of measurements are also provided. All measurements were made at room temperature with the new transient hot wire instrument described in section 3.3.1. The samples consisted of alumina or ceria nanoparticles dispersed in water and alumina in ethylene glycol. The error bars in the figures represent the estimated experimental error.

Figure 4.10 and 4.11 display a linear particle volume fraction dependence for aqueous alumina and ceria nanofluids, respectively. The same trend has been observed in many studies in the literature as discussed in section 2.3.2.1. Note that the slope increases as the particle size increases. Figure 4.12 displays the thermal conductivities for aqueous alumina nanofluids as a function of particle diameter. The thermal conductivity generally decreases with decreasing particle size below a certain particle diameter (~ 50 nm). The thermal conductivity of nanofluids containing larger particles appears nearly constant with particle diameter. Additionally, the thermal conductivity decreased as the particle size decreased for the nanofluids consisting of alumina in ethylene glycol (Figure 4.13).

Figure 4.12 displays a comparison of thermal conductivities for aqueous nanofluids containing alumina from this work and from the work of Chon et al. [50] and Timofeeva et al. [58]. Chon et al observed an increase in the thermal conductivity of the nanofluids as the particle diameter decreased. Alternatively, the data from Timofeeva et al. is similar to data from this work, where the addition of the largest particles yielded the

greatest thermal conductivity of the nanofluids. In each study, only three different sizes of nanoparticles were considered, but they demonstrate the discrepancy in nanofluid thermal conductivity data in the literature.

The effect of the ratio of solid to liquid thermal conductivities α has not been rigorously studied in this work. However, the thermal conductivity enhancement of nanofluids containing ethylene glycol and alumina was greater than that of aqueous nanofluids containing the same size of alumina particles. The ethylene glycol has a lower thermal conductivity than water, so α is higher for these nanofluids containing ethylene glycol. Figure 4.14 displays this difference in thermal conductivity enhancement.

Table 4.10 Thermal conductivity of aqueous nanofluids containing Al_2O_3

Average Particle Diameter (nm)	T (K)	Volume fraction of Al_2O_3	Mean k W m^{-1} K^{-1}	Standard Deviation
8	299.1	1.93 %	0.620	0.017
8	297.4	2.99 %	0.621	0.008
8	297.7	3.99 %	0.623	0.016
12	297.4	2.00 %	0.622	0.006
12	297.4	3.00 %	0.630	0.009
12	297.8	4.00 %	0.640	0.005
16	296.8	2.00 %	0.635	0.003
16	298.0	3.00 %	0.642	0.015
16	298.3	3.98 %	0.662	0.015
46	298.0	2.00 %	0.637	0.017
46	298.3	2.99 %	0.644	0.018
46	297.8	3.99 %	0.660	0.011
71	299.9	0.93 %	0.633	0.009
71	296.8	1.86 %	0.657	0.010
71	297.7	3.00 %	0.696	0.017
71	296.6	3.99 %	0.712	0.016
245	300.5	1.86 %	0.656	0.013
245	298.5	3.00 %	0.678	0.012
245	299.1	4.00 %	0.709	0.013
282	297.7	1.00 %	0.646	0.016
282	297.4	2.00 %	0.669	0.011
282	298.0	3.00 %	0.693	0.008
282	298.7	4.00 %	0.719	0.020

Table 4.11 Thermal conductivity of nanofluids containing Al_2O_3 in ethylene glycol

Average Particle Diameter (nm)	T (K)	Volume fraction of Al_2O_3	Mean k W m^{-1} K^{-1}	Standard Deviation
12	298.6	2.00 %	0.272	0.001
12	298.0	3.00 %	0.276	0.002
16	298.6	2.00 %	0.273	0.001
16	297.9	3.00 %	0.281	0.002
245	298.6	2.00 %	0.280	0.002
245	298.3	2.99 %	0.294	0.003
282	297.9	2.00 %	0.283	0.002
282	298.0	3.01 %	0.299	0.002

Table 4.12 Thermal conductivity of aqueous nanofluids containing CeO_2

Average Particle Diameter (nm)	T (K)	Volume fraction of CeO_2	Mean k W m^{-1} K^{-1}	Standard Deviation
12	297.7	2.00 %	0.630	0.006
12	297.9	3.00 %	0.649	0.010
12	298.0	4.00 %	0.671	0.013
74	297.8	2.00 %	0.659	0.010
74	298.7	3.00 %	0.693	0.016
74	298.1	4.00 %	0.730	0.020

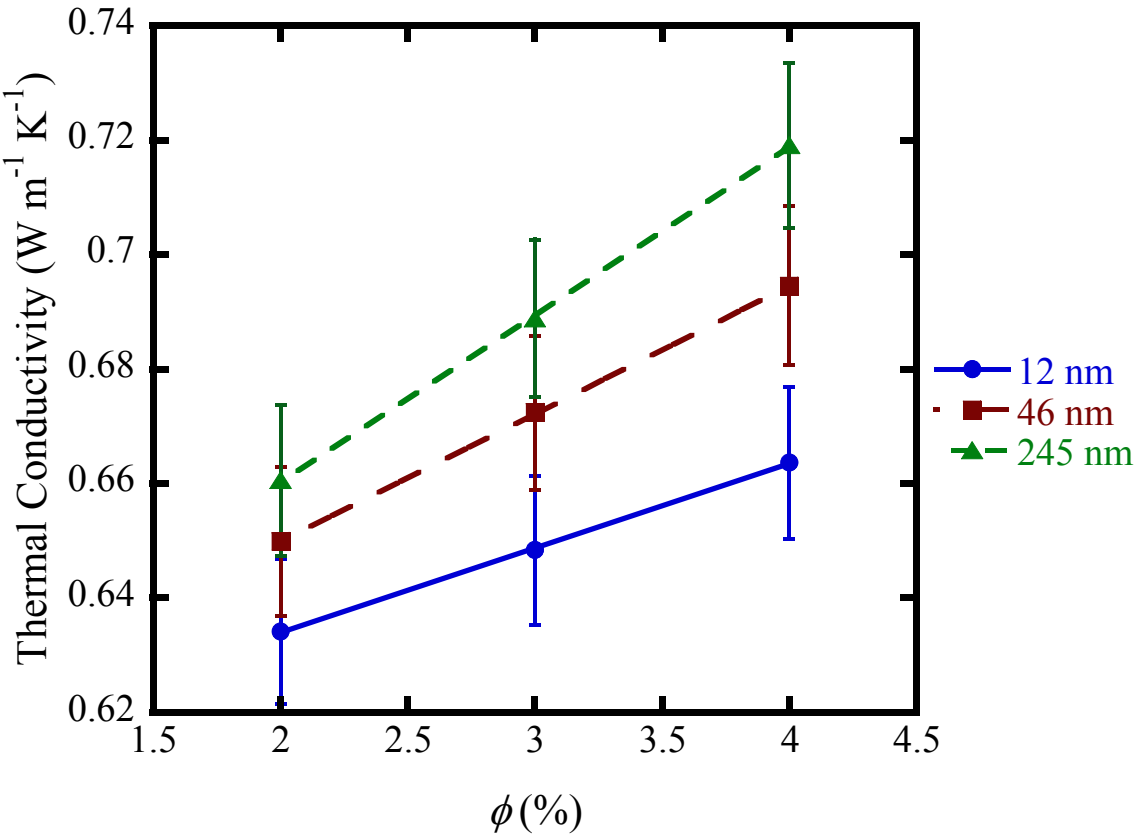

Figure 4.10 Thermal conductivity versus volume fraction for aqueous nanofluids containing alumina at room temperature. The lines represent linear fits.

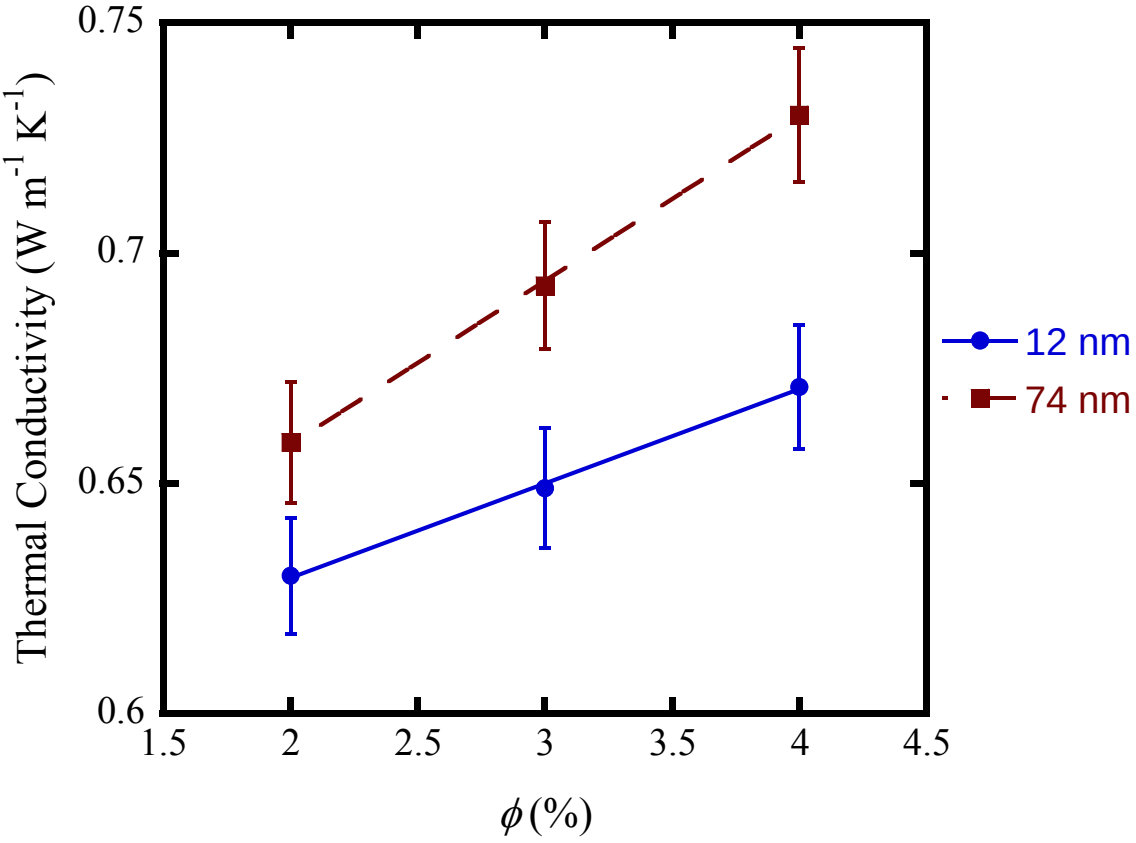

Figure 4.11 Thermal conductivity versus volume fraction for aqueous nanofluids containing ceria at room temperature. The lines represent linear fits.

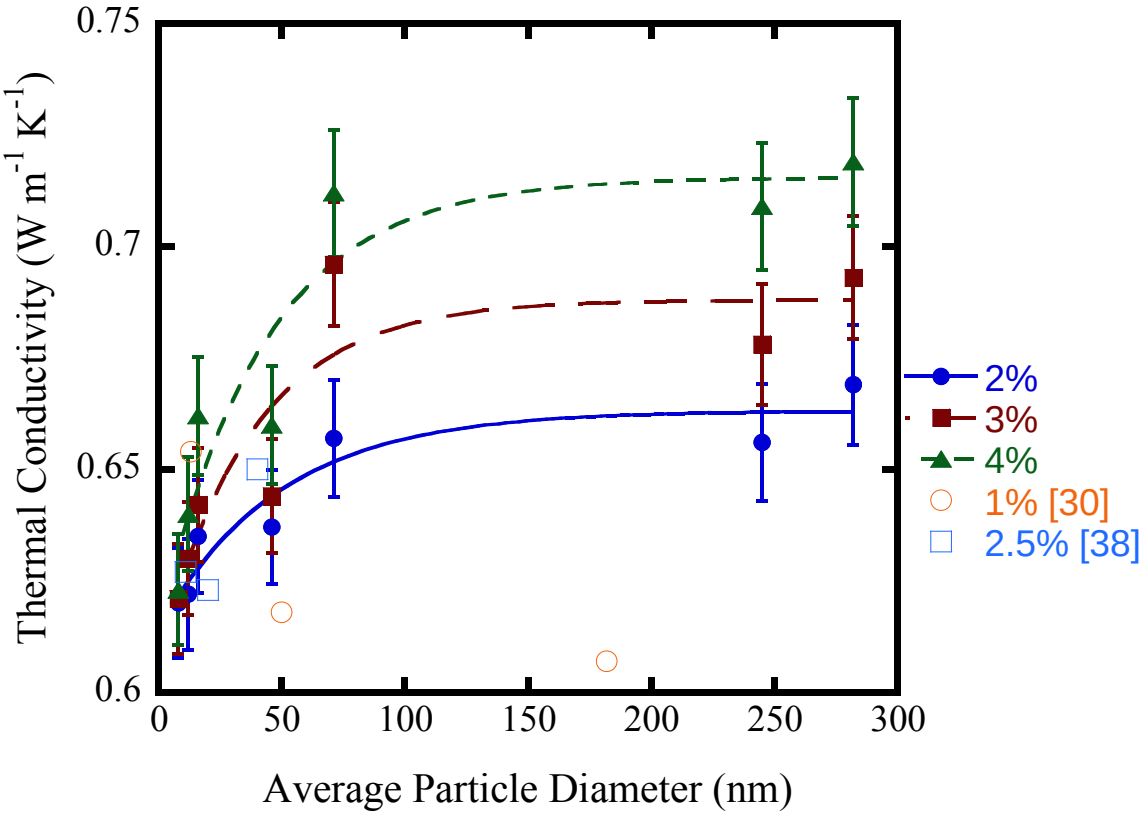

Figure 4.12 Thermal conductivity of aqueous nanofluids containing 2 - 4 % (v/v) alumina at room temperature. Empirical curve fits are provided to aid in visual detection of trends in the data. Data from Chon et al. [50] and Timofeeva et al. [58] is presented for comparison.

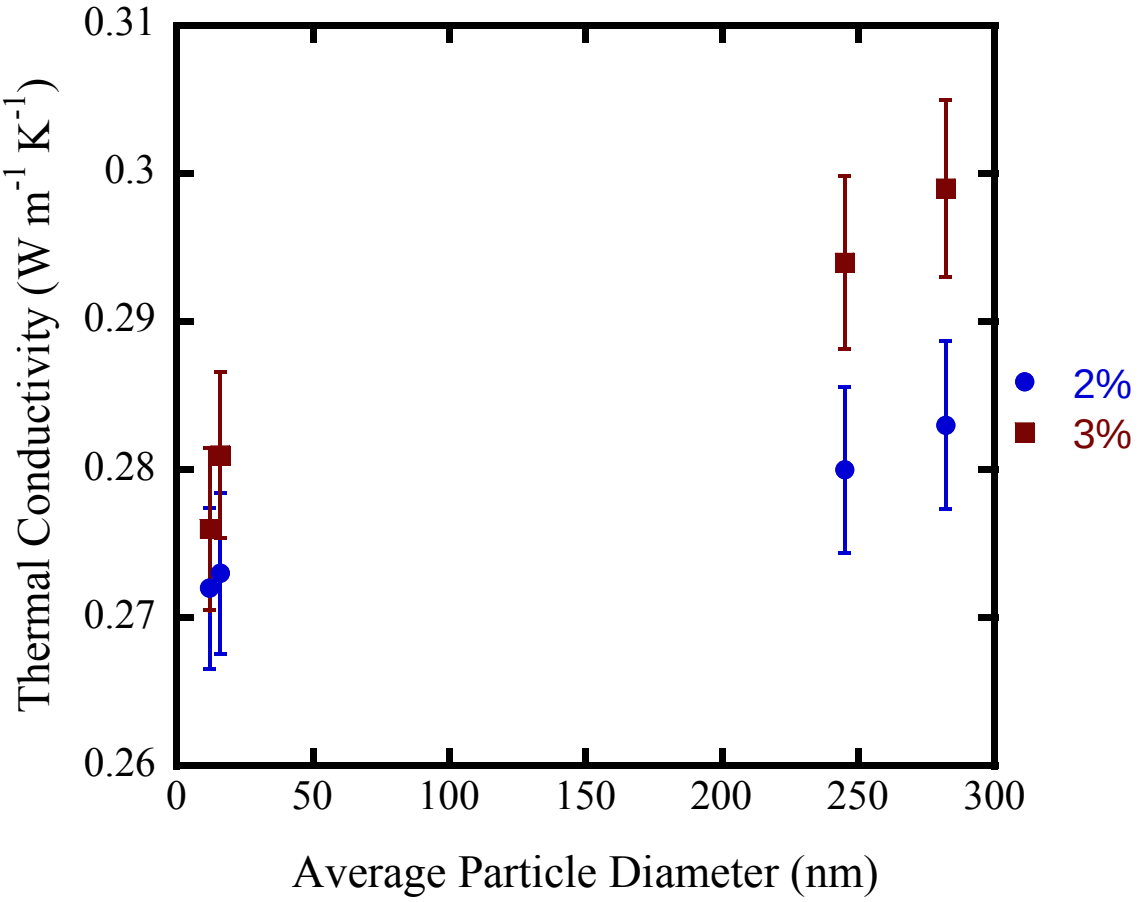

Figure 4.13 Thermal conductivity of nanofluids consisting of 2 - 4 % (v/v) alumina in ethylene glycol at room temperature.

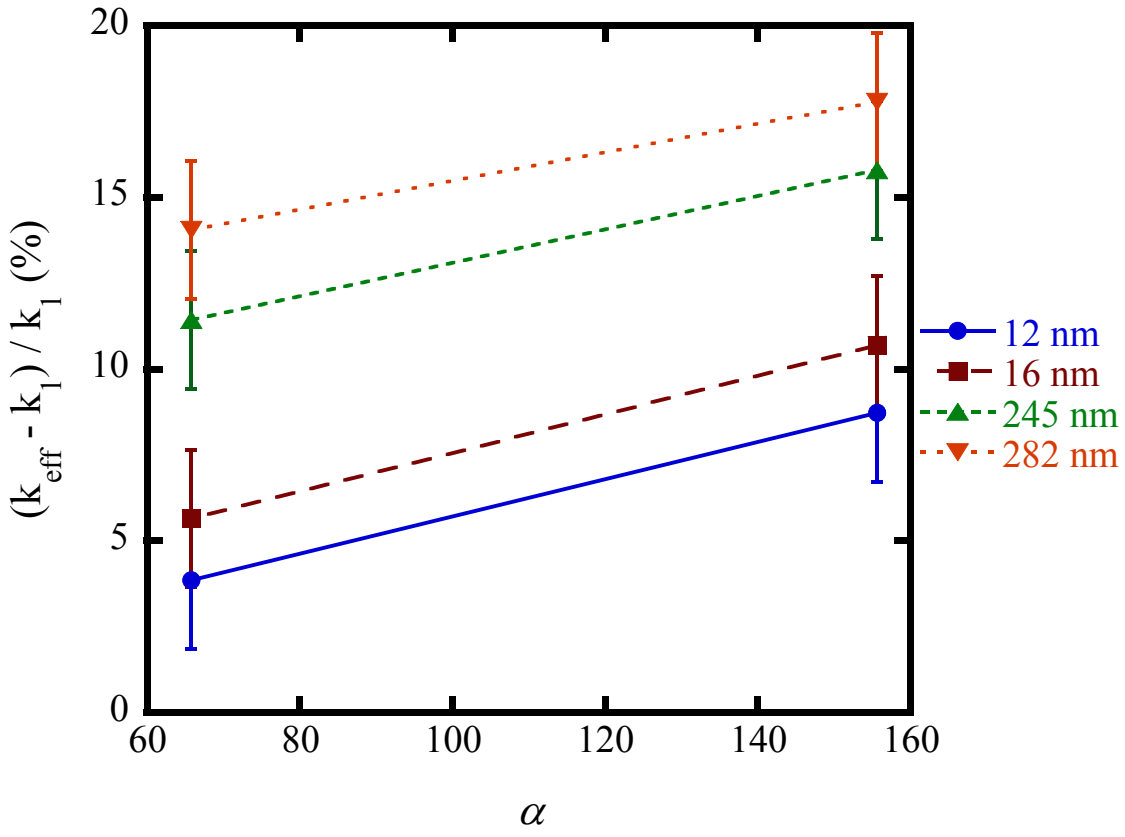

Figure 4.14 Thermal conductivity enhancement of nanofluids containing 3 % (v/v) alumina as a function of the ratio of solid to liquid thermal conductivity at room temperature.

4.4 Thermal Conductivity Behavior

The thermal conductivity of nanofluids displayed a temperature dependence similar to the base fluid in this work. This trend was observed in nanofluids consisting of alumina and water, alumina and ethylene glycol, and alumina and a mixture of ethylene glycol and water. A maximum was observed in the thermal conductivity versus temperature curve for nanofluids at approximately the same temperature as the maximum for the base fluid.

The thermal conductivity of nanofluids appears to decrease with decreasing particle size below a certain diameter (< 50 nm), but seems constant above that size. This trend was observed for aqueous alumina nanofluids. Nanofluids containing alumina and ethylene glycol and aqueous ceria nanofluids also exhibited a decreasing thermal conductivity with decreasing particle diameter.

The thermal conductivities of nanofluids in this work exhibited particle volume fraction and α dependences in agreement with the literature. The thermal conductivity linearly increases with increasing particle volume fraction, and the thermal conductivity enhancement increases with increasing α.

CHAPTER 5

BACKGROUND - THEORY

The transport properties of heterogeneous systems have been the subject of many investigation beginning with Maxwell [118] who derived an expression for the effective conductivity of a medium containing a dilute suspension of non-interacting spheres as follows:

$$\frac{k_{eff}}{k_1} = 1 + \frac{3(\alpha - 1)\phi}{(\alpha + 2) - (\alpha - 1)\phi} \tag{5.1}$$

where ϕ is the volume fraction of spheres and,

$$\alpha = {k_2}/{k_1} \tag{5.2}$$

with k_1 and k_2 being the conductivities of the continuous and discrete phases, respectively. This equation was derived for the electrical conductivity, but it applies to other transport properties such as thermal conductivity. Many studies have focused on extensions of this model to account for the interaction of particles in more concentrated suspensions, particle shape, and arrangements of particles. The more commonly used models are discussed in this section. A more detailed discussion of thermal conductivity models for heterogeneous materials can be found elsewhere [119-121].

Tsotsas and Martin [120] classified thermal conductivity models for heterogeneous systems into three categories, solutions (analytical or numerical) of the Laplace equation (type I), empirical models consisting of combinations of resistances in series and in parallel (type II), and solutions of a unit cell with either parallel heat flux

vectors or parallel isotherms (type III). This discussion will be limited to the first two of these categories since they are more commonly used.

5.1 Type I Thermal Conductivity Models

The Maxwell equation (Eq. 5.1) was the first model for transport properties of a heterogeneous system derived by solving the Laplace equation,

$$\nabla^2 T = 0 \tag{5.3}$$

He considered a dilute dispersion of n_S spheres with radius a and thermal conductivity k_2 in a continuous medium with thermal conductivity k_1.and a constant temperature gradient, G, far from the spheres. The Laplace equation can then be solved in spherical coordinates for the temperature inside and outside the spheres with the following boundary conditions:

$$\begin{aligned} &T(r,\theta)_{r\to\infty} = Gr\cos\theta \\ &T_2(r,\theta)\big|_{r=a} = T_1(r,\theta)\big|_{r=a} \\ &k_2 \left.\frac{\partial T_2}{\partial r}\right|_{r=a} = k_1 \left.\frac{\partial T_1}{\partial r}\right|_{r=a} \end{aligned} \tag{5.4}$$

The last boundary condition is based on the assumption that each sphere is surrounded by the base fluid and does not interact with other spheres. Each sphere is considered separately, and the total effect is obtained by multiplying by the number of spheres. The resulting solutions for the temperature within and outside the sphere is as follows,

$$T_2(r,\theta) - T_0 = \left(\frac{3k_1}{2k_1 + k_2}\right) Gr\cos\theta \tag{5.5}$$

$$T_1(r,\theta) - T_0 = \left(1 - \frac{k_2 - k_1}{2k_1 + k_2}\frac{n_S a^3}{r^3}\right) Gr\cos\theta \tag{5.6}$$

where T_0 is the temperature at the center of a sphere. If this dispersion with an effective thermal conductivity k_{eff} is contained within a single sphere of radius b and surrounded by the same base fluid, equation 5.3 can be solved with the following boundary conditions:

$$\begin{aligned} T(r,\theta)_{r\to\infty} &= Gr\cos\theta \\ T_m(r,\theta)\big|_{r=b} &= T_1(r,\theta)\big|_{r=b} \\ k_{eff}\left.\frac{\partial T_m}{\partial r}\right|_{r=b} &= k_1\left.\frac{\partial T_1}{\partial r}\right|_{r=b} \end{aligned} \tag{5.7}$$

The resulting solution is,

$$T_1(r,\theta) - T_0 = \left(1 - \frac{k_{eff} - k_1}{2k_1 + k_{eff}}\frac{b^3}{r^3}\right)Gr\cos\theta \tag{5.8}$$

By introducing the volume fraction of spheres,

$$\phi = {n_S a^3}\Big/{b^3} \tag{5.9}$$

equations 5.6 and 5.8 can be combined to yield equation 5.1.

Many models have been proposed to overcome some of the limitations of the Maxwell model. For example, Lord Rayleigh [122] derived a series of linear equations which provide a thermal conductivity for concentrated systems of square arrays of cylinders or cubic arrays of spheres. Hamilton and Crosser [123] extended the Maxwell equation to include an empirical shape factor, *n*,

$$\frac{k_{eff}}{k_1} = 1 + \frac{n(\alpha - 1)\phi}{(\alpha + n - 1) - (\alpha - 1)\phi} \tag{5.10}$$

For systems where $\alpha < 100$, n is equal to 3, which is equivalent to the Maxwell equation. For systems where $\alpha > 100$, n is defined by the following equation,

$$n = {3}\Big/{\psi} \tag{5.11}$$

where ψ is the sphericity of the particles. This model provided predictions within 2 % of measured thermal conductivity values for mixtures of rubber with aluminum particles of different shapes ($0.5 < \psi < 1.0$). Additionally, Jeffrey [124] extended the first order Maxwell equation to include a second order term by including the effect of interactions between pairs of spheres to give:

$$\frac{k_{eff}}{k_1} = 1 + 3\beta\phi + \phi^2\left(3\beta^2 + \frac{3\beta^3}{4} + \frac{9\beta^3}{16}\frac{\alpha+2}{2\alpha+3} + \frac{3\beta^4}{2^6} + \ldots\right) \tag{5.12}$$

where,

$$\beta = \frac{\alpha - 1}{\alpha + 2} \tag{5.13}$$

The terms inside the parentheses are a convergent infinite series. This equation was also developed for a dilute suspension. Thus, for small values of ϕ, the equation is equivalent to the Maxwell equation if the second order term is neglected.

Progelhof et al. [121] described an equation developed by Bruggeman [125] for the thermal conductivity of dilute suspensions of spheres. In contrast to the Maxwell equation, the effective medium approximation was used in the derivation to give:

$$1 - \phi = \left(\frac{k_2 - k_{eff}}{k_2 - k_1}\right)\left(\frac{k_1}{k_{eff}}\right)^{1/3} \tag{5.14}$$

With the effective medium approximation, each sphere is considered to be suspended in a medium with a homogenous conductivity of k_{eff}. Landauer [126] also employed this approximation in his derivation for the thermal conductivity of a suspension of spheres,

$$(1-\phi)\frac{k_1 - k_{eff}}{k_1 + 2k_{eff}} + \phi\frac{k_2 - k_{eff}}{k_2 + 2k_{eff}} = 0 \tag{5.15}$$

Landauer observed that predictions of this equation compared favorably with experimental electrical conductivity data for binary metallic mixtures over the entire range of concentrations [126]. The derivation did not require the assumption of a dilute suspension of spheres. However, the equation was developed under the assumption that a single particle is surrounded by a random arrangement of volumes containing either the medium or a particle. As a result, this model does not provide accurate predictions of the thermal conductivity of dispersions containing aggregated particles [48].

5.2 Type II Thermal Conductivity Models

The second type of thermal conductivity model for heterogeneous materials considers a suspension as an array of elements with specific resistances. This system is then modeled as a combination of resistances in series and in parallel. The simplest of these models was described by Keey [127] and developed by Krischer [128],

$$k_{eff} = \left[\frac{1-f}{(1-\phi_2)k_1 + \phi_2 k_2} + f\left(\frac{1-\phi_2}{k_1} + \frac{\phi_2}{k_2} \right) \right]^{-1} \tag{5.16}$$

where f is an empirical factor equivalent to the relative proportion of parallel resistances in a rectangular array of elements. No assumption is made regarding the spacing of the discrete phase. Thus, the model is capable of incorporating the irregular arrangement of particles. However, experimental data is required to estimate the empirical factor. A useful aspect of this model is that it provides upper ($f = 0$) and lower ($f = 1$) bounds for the thermal conductivity of heterogeneous materials. If $f = 0$, all of the particles are arranged in series which creates a pathway of high thermal conductivity and maximizes the effective thermal conductivity of the dispersion. If $f = 1$, all of the particles are arranged in parallel and therefore minimizes the effective thermal conductivity of the

dispersion. Tsao [129] developed a model similar to the Krischer model which includes the effect of different geometries of the discrete phase. His model gives:

$$k_{eff} = \left[\int_0^1 \frac{dP_1}{k_1 + (k_2 - k_1)\int_{P_1}^1 \frac{1}{\sigma\sqrt{2\pi}} e^{-1/2\left(\frac{P_1 - \phi}{\sigma}\right)} dP_1} \right]^{-1} \tag{5.17}$$

where P_1 and σ are parameters that must be determined experimentally. Tsao defined P_1 as the one dimensional porosity which is the fraction of the discrete phase on any line drawn through a cubic volume of the heterogeneous material, and σ is the standard deviation of P_1.

5.3 Theoretical Bounds for Thermal Conductivity of Heterogeneous Materials

It may be deduced from the above discussion that the thermal conductivity of heterogeneous materials depends on the spatial distribution of each phase [130]. Since this information is typically unavailable, theoretical bounds for the thermal conductivity are often considered. As mentioned earlier, Krischer's model gives upper and lower bounds when $f = 0$ and $f = 1$. Hashin and Shtrikman [130] derived more restrictive bounds using variational theorems to give:

$$1 + \frac{3\phi(\alpha - 1)}{\alpha + 2 - \phi(\alpha - 1)} \leq \frac{k_{eff}}{k_1} \leq \alpha\left[1 - \frac{3(\alpha - 1)(1 - \phi)}{3\alpha - \phi(\alpha - 1)}\right] \tag{5.18}$$

Note that the lower bound is equivalent to the Maxwell equation. Thus, an idealized suspension with homogeneously dispersed spheres yields the lowest thermal conductivity of any spatial arrangement.

5.4 Accuracy of Thermal Conductivity Models

Turian et al. [48] compared many theoretical models for the thermal conductivity of heterogeneous materials with available data on solid – liquid dispersions ($0.16 < \alpha < 1507$). They demonstrated that when the difference between the thermal conductivities of each phase is small ($0.4 < \alpha < 2.4$), many of the thermal conductivity models (Maxwell [118], Jeffrey [124], Bruggeman [125]) agree within 2 % with experimental data for dilute suspensions ($\phi < 0.15$). For these values of α, the Jeffrey and the Bruggeman equations were accurate within 2 % for more concentrated suspensions as well. However, as α increased, agreement with experimental data was less satisfactory. For each dispersion considered, the Jeffrey model was more accurate than the Maxwell equation, and the Bruggeman model was more accurate than both the Maxwell and Bruggemann models.

5.5 Geometric Mean

Turian et al. [48] found that the volume fraction – weighted geometric mean of the thermal conductivities of the individual phases,

$$k_{eff} = k_1^{1-\phi} k_2^{\phi} \tag{5.19}$$

provided as good or a better prediction of the thermal conductivity than any of the theoretical models when $\alpha > 3.5$. This empirical equation seems to better reflect the thermal conductivity of real dispersions containing interacting particles with irregular spatial arrangement as opposed to the ideal homogeneously dispersed systems considered by Maxwell. Turian et al. investigated the volume – fraction weighted arithmetic, geometric, and harmonic means in addition to theoretical thermal conductivity models. The arithmetic mean and the harmonic mean are equivalent to the upper and lower

bounds provided by the Krischer model, and the geometric mean falls between these bounds. Moreover, the geometric mean is within the more restrictive Hashin – Shtrikman bounds for $\alpha > 5$. In their comparison of various model predictions with experimental data, the average deviation for $3.5 < \alpha < 70$ was 14.3 % with the Maxwell equation and 5.7 % with equation 5.19, and for $70 < \alpha < 200$ the average deviation was 26.3 % with the Maxwell equation and 9.9 % with equation 5.19. Overall, the volume fraction – weighted geometric mean provided the best prediction of experimentally measured thermal conductivities of solid – liquid dispersions.

5.6 Nanofluid Thermal Conductivity Models

Keblinski et al. [14] considered several size dependent contributions to the thermal conductivity of nanofluids and suggested that the enhancement in thermal conductivity is due to Brownian motion of the particles, or to ordered liquid molecules at the liquid / particle interface, or nanoparticle clustering. The Brownian motion of the nanoparticles results in collisions between particles that can cause heat to transfer directly from particle to particle. However, a simple kinetic analysis showed that mechanism could be discounted. They then assumed that the liquid molecules at the surface of the particles are more conductive because they exhibit higher order than bulk liquid molecules. As there is greater surface area associated with smaller particles, a greater fraction of the liquid molecules is ordered and contributes to enhanced conduction. Keblinski et al. also considered aggregation or clustering of suspended particles and showed that it is possible for these clusters to create paths of lower thermal resistance. The higher specific surface area of nanoparticles promotes a greater degree of aggregation than with a suspension of larger particles. This last theory is very similar to

that of Krischer [128], who developed an empirical model to describe the irregular arrangement of suspended particles. Most nanofluid thermal conductivity models were developed based on one or more of these mechanisms.

5.6.1 Brownian Motion

Many models attribute the enhanced thermal conductivity of nanofluids to the effect of Brownian motion. Instead of heat transfer between individual particles, the hypothesis is that interaction between the dynamic particles and fluid molecules enhances conduction. As the particles move randomly through the fluid, they carry fluid molecules with them and create a local convective effect at the microscale level, thus enhancing thermal conduction. As an example, the Jang and Choi [131] model is based on a linear combination of contributions from the liquid, the suspended particles, and the Brownian motion of the particles to give:

$$\frac{k_{eff,m}}{k_1} = (1-\phi) + \varepsilon\alpha\phi + C_1 \frac{d_f}{d} \mathrm{Re}^2 \, \mathrm{Pr}\, \phi \tag{5.20}$$

where ε is a constant related to the Kapitza resistance (see Section 5.6.4), C_1 is a proportionality constant, d_f is the diameter of a fluid molecule, and Re and Pr are the Reynolds the Prandtl numbers of the fluid, respectively. The Reynolds number, Re, is defined by,

$$\mathrm{Re} = \frac{\rho k_B T}{3\pi\mu^2 l_f} \tag{5.21}$$

where k_B is the Boltzmann constant, l_f is the mean free path of a fluid molecule, and ρ and μ are the density and viscosity of the fluid, respectively. Their model reflects a strong temperature dependence due to Brownian motion and a simple inverse relationship with

the particle diameter. As the particle diameter increases, the third term becomes negligible and the model reduces to a linear combination of the thermal conductivity of the fluid and the contribution from the particle. However, it has been demonstrated repeatedly that a linear combination of the individual thermal conductivity contributions is a poor predictor of the effective thermal conductivity in heterogeneous systems [48, 120]. Based on the Jang and Choi model, Chon et al. [50] employed the Buckingham-Pi theorem to develop the following empirical correlation,

$$\frac{k_{eff,m}}{k_1} = 1 + 64.7\phi^{0.7460}\left(\frac{d_f}{d}\right)^{0.3690} \alpha^{0.7476}\,\mathrm{Pr}^{0.9955}\,\mathrm{Re}^{1.2321} \tag{5.22}$$

where the Reynolds and Prandtl numbers are the same as in the Jang and Choi model. The equation was fit to their measurements of aqueous nanofluids containing three sizes of alumina particles. However, their correlation is of limited use, since it is based on measurements over a limited temperature range (20 – 70 ºC) and it was fit to thermal conductivity data for a single nanoparticle material in a single base fluid. Chon et al. did not demonstrate any ability of their model to predict the thermal conductivity of other nanofluids. Other models are available that are fitted to similarly limited nanofluid data and include no consideration for the more conventional thermal conductivity models [132-134]. However, some researchers have used conventional heterogeneous thermal conductivity models as a starting point and extended these to include a particle size dependence based on Brownian motion [135-139]. For instance, Xuan et al. [138] developed an extension of the Maxwell equation to include the microconvective effect of the dynamic particles and the heat transfer between the particles and fluid to give:

$$\frac{k_{eff,m}}{k_1} = \frac{\alpha + 2 + 2\phi(\alpha - 1)}{\alpha + 2 - \phi(\alpha - 1)} + \frac{18\phi HAk_B T}{\pi^2 \rho d^6 k_1}\tau \tag{5.23}$$

where H is the overall heat transfer coefficient between the particle and the fluid, A is the corresponding heat transfer area, and τ is the comprehensive relaxation time constant. The heat transfer area should be proportional to the square of the diameter, thus the effective thermal conductivity is proportional to the inverse of the particle diameter to the fourth power. Such a strong particle size dependence has yet to be demonstrated experimentally. Additionally, the equation reduces to the Maxwell equation with increasing particle size. As discussed previously, thermal conductivity enhancements greater than those predicted by the Maxwell equation have been reported for nanofluids containing relatively large nanoparticles (d > 30 nm) [59]. It is therefore obvious that models that reduce to the Maxwell equation at large nanoparticle sizes will not be able to represent published data.

The Brownian motion models share a common attribute that distinguishes them from other models. Each model exhibits a monotonically increasing relationship between the thermal conductivity and temperature due to the temperature dependence of the velocity of the particles. This behavior has been observed over a limited temperature range for nanofluids between 10 ºC and 70 ºC [8, 9, 50, 52, 58]. However, all of these studies have focused on nanofluids consisting of polar liquids, water and ethylene glycol. The thermal conductivities of these liquids increase with temperature unlike most other liquids. In the one study [10] which considered nanoparticles in a liquid with decreasing thermal conductivity, perfluorohexane, the thermal conductivity of the nanofluid decreased with increasing temperature.

5.6.2 Ordered Liquid Molecules

A layer of ordered liquid molecules adjacent to the surface of the solid particles has been credited with the enhanced thermal conductivity observed in nanofluids. Molecules in this layer exhibit greater order than bulk liquid molecules, and with greater order, they should exhibit a greater thermal conductivity than that of the bulk liquid. Yu and Choi [140] developed the following extension of the Maxwell equation which incorporates a layer of ordered liquid molecules into an effective particle,

$$\frac{k_{eff,m}}{k_1} = \frac{k_{pe} + 2k_1 + 2(1+\beta_l)^3(k_{pe} - k_1)}{k_{pe} + 2k_1 - (1+\beta_l)^3(k_{pe} - k_1)}, \tag{5.24}$$

where the thermal conductivity of the effective particle is defined as,

$$k_{pe} = \frac{\left[2(1-\gamma) + (1+\beta_l)^3(1+2\gamma)\right]\gamma}{-(1-\gamma) + (1+\beta_l)^3(1+2\gamma)} k_2, \tag{5.25}$$

$$\gamma = k_{layer} \Big/ k_2, \tag{5.26}$$

$$\beta_l = h \Big/ d, \tag{5.27}$$

where k_{layer} is the thermal conductivity of the ordered liquid layer of molecules and h is the thickness of that layer. Others [141-146] have developed similar models using the same method of defining an effective particle which includes the solid particle and the surrounding ordered liquid layer. These models are capable of fitting some of the experimental data available in the literature by adjusting the thickness and thermal conductivity of the ordered liquid layer. However, Evans et al. [147] used molecular dynamics simulations to estimate the thermal conductivity of water molecules with greater order and found that the thermal conductivity was greater by an order of three when the water had crystalline order. Thus, the thermal conductivity of the ordered water

layer should be less than or equal to three times the thermal conductivity of bulk water. By using this value in any of the aforementioned models, the thermal conductivity enhancement is equivalent to the Maxwell equation except at very small values of particle diameter (< 5 nm). Based on this data, nanofluids would be more thermally conductive than other dispersions only if the diameter of the nanoparticles is less than 5 nm.

An inverse relationship between thermal conductivity and particle size is a common attribute among both the Brownian motion and ordered liquid thermal conductivity models. In certain models, this relationship is stronger (Xuan et al. [138]) than others (Chon et al. [50]). However, there is little to no experimental evidence to support this relationship. Some studies have examined the effect of particle size on thermal conductivity, and have found slightly greater enhancement [50, 52] or lower enhancement [12, 58] with decreasing particle size.

5.6.3 Nanoparticle Clustering

The difference between models developed to account for nanoparticle clustering [148-150] and models which reflect the spatial arrangement of particles is that the nanoparticle clustering models include a particle size dependence. The smaller particle size creates greater attraction between the individual particles, which leads to a greater extent of aggregation. Prasher et al. [150] extended the Maxwell equation for use with a dispersion of particle aggregates. Each aggregate consists of nanoparticles, a fraction of which form a conductive pathway, or backbone, while the remaining nanoparticles are considered dead ends. They calculated the thermal conductivity of the fluid and dead ends inside the aggregate (k_{nc}) and then found the thermal conductivity of the effective

aggregate (k_a) by including the backbone. This concept is illustrated in Figure 5.1. This model is quite difficult to use as it requires knowledge of the aggregate size as well as the proportion of nanoparticles forming conductive pathways through the aggregate.

The hypothesis that particle clustering enhances conduction in suspensions is well supported by numerical simulations and molecular dynamics studies [151-153]. However, those studies did not find a significant particle size dependence.

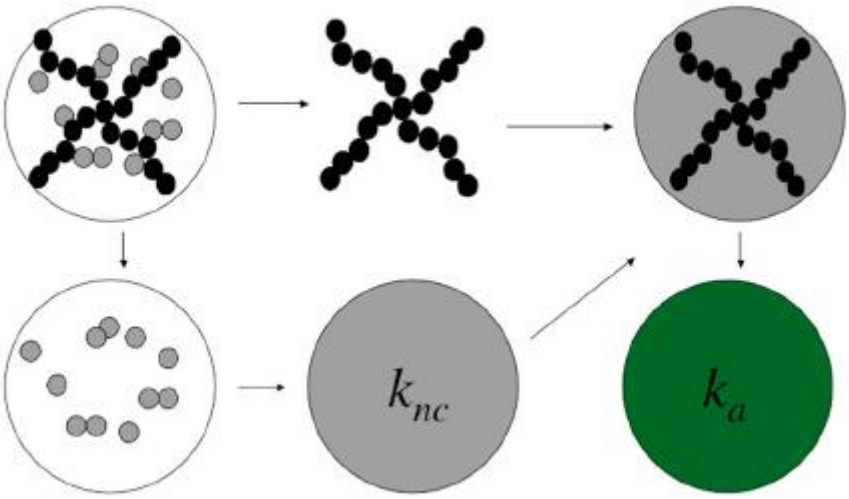

Figure 5.1 Schematic of method by Prasher et al. [150] to determine the thermal conductivity of an aggregate which includes the backbone of nanoparticles, the dead end nanoparticles and the fluid surrounding the particles.

5.6.4 Interfacial Thermal Resistance

In contrast to the previously discussed phenomena, thermal resistance at the solid-liquid interface should lead to a reduction in the thermal conductivity of the dispersion. The interfacial thermal resistance is defined as a temperature discontinuity at the interface and is sometimes referred to as the Kapitza resistance [154]. This empirical property

incorporates phonon scattering that occurs at the interface as well as any other phenomena that create resistance to heat transport across the interface such as poor contact between the substances. Nan et al. [155] presented several models which incorporate the shape of the particle and the interfacial thermal resistance into the Maxwell equation. For spheres the model is as follows,

$$\frac{k_{eff}}{k_1} = \frac{\alpha(1+2\chi)+2+2\phi[\alpha(1-\chi)-1]}{\alpha(1+2\chi)+2-\phi[\alpha(1-\chi)-1]}, \tag{5.28}$$

$$\chi = \frac{2R_B k_1}{d}, \tag{5.29}$$

where R_B is the interfacial thermal resistance. When $\chi << 1$, equation 5.28 reduces to the Maxwell equation. As χ increases due to smaller diameter or greater resistance, the effective thermal conductivity of the nanofluid decreases. The work of Prasher et al. [136] extends this model to include the effect of Brownian motion. The interfacial thermal resistance has been measured for a few systems, carbon nanotubes with sodium dodecyl sulfate (SDS) in D_2O [156], citrate-stabilized Pt nanoparticles in water and thiol-stabilized AuPd nanoparticles in toluene [157]. The thermal conductivity of these systems can be estimated by using these values of the interfacial thermal resistance in conjunction with equation 5.28. For example, based on the value for Pt in water, an aqueous nanofluid containing 25 nm diameter Pt particles would enhance the thermal conductivity half as much as a nanofluid containing 100 nm diameter Pt particles.

5.7 Summary of Thermal Conductivity Models for Nanofluids

Numerous thermal conductivity models have been developed for heterogeneous systems and specifically for nanofluids. Theoretical models such as those by Maxwell

[118] and Bruggeman [125] were derived by assuming a homogeneous or random arrangement of particles. However, these assumptions are not valid for dispersions containing aggregates. Empirical models [48, 128] have been successfully employed to account for the spatial arrangement of particles. More recently, particle size has been incorporated into many models in an attempt to describe the thermal conductivity of nanofluids. Several mechanisms have been described in the previous section that may affect the thermal conductivity of nanofluids, including Brownian motion of the particles, ordered liquid molecules at the solid / liquid interface, nanoparticle clustering, and interfacial thermal resistance. However, there is no consensus as to which mechanism has the dominant effect on the thermal conductivity.

CHAPTER 6

THERMAL CONDUCTIVITY MODELING OF SOLID / LIQUID DISPERSIONS

There have been many attempts to model the thermal conductivity of nanofluids and to elucidate the mechanisms for conduction in these fluids [50, 131, 136, 140, 150]. In this chapter, some of the models and mechanisms discussed in chapter 2 are evaluated using the data presented in Chapter 4.

6.1 Evaluation of Thermal Conductivity Models

A number of thermal conductivity models have been discussed in Chapter 5. These models have been evaluated in terms of their predictions and through a comparison trends in the thermal conductivity data presented in Chapter 5. This assessment has been performed through an examination of the relationships between the thermal conductivity of nanofluids and volume fraction (ϕ), temperature (T), the ratio of the pure phase thermal conductivities (α), and the particle diameter (d).

6.1.1 Particle Volume Fraction

The thermal conductivity of nanofluids in this work generally exhibited a linear relationship with the volume fraction between 1 and 5 % as displayed in Figure 6.1. The linear trend observed in this work has also been commonly observed in the literature [8, 12, 49, 57, 60]. Some exceptions have been reported in the case of particle volume fractions less than 1 % (v/v) [66, 69], but such dilute nanofluids were not considered in this work. Thus, the nonlinear relationship observed by Murshed et al. [66] displayed in

Figure 2.6 was not observed in this work. Throughout the range of particle volume fractions considered in this work (1 – 5 %), all of the thermal conductivity models discussed in chapter 5 exhibit a linear relationship with respect to particle volume fraction (Figures 4.10 and 4.11). Figure 6.1 includes a comparison of the predicted thermal conductivity versus volume fraction relationship for various models. At particle volume fractions between 1 and 5 %, the models by Bruggemann, Landauer, and Jeffrey predict thermal conductivity values within 2 % of the Maxwell equation. Thus, the Maxwell model effectively predicts the same trends as these models and will be the only of these models discussed in this chapter.

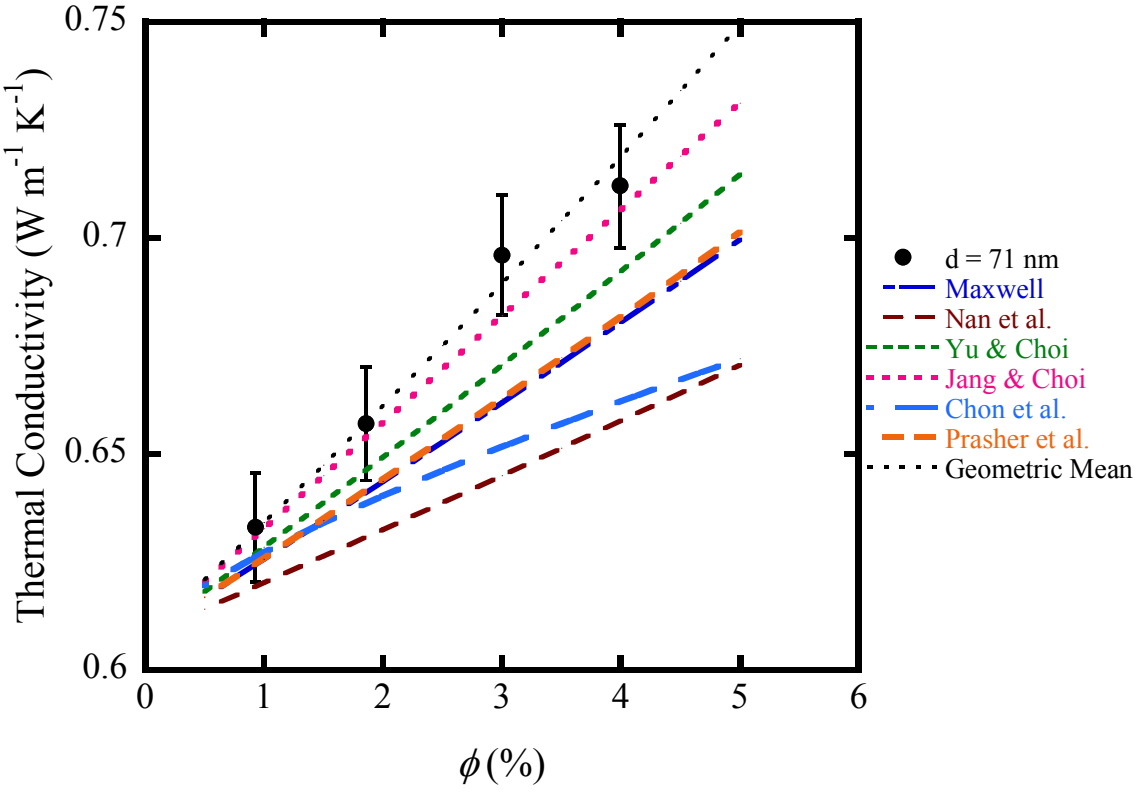

Figure 6.1 Thermal conductivity measurements and predictions for an aqueous nanofluid containing alumina (diameter = 72 nm) from several models as a function of volume fraction (ϕ). The error bars represent the estimated measurement error.

6.1.2 Temperature

The thermal conductivity models based on Brownian motion exhibit a strong temperature dependence while the temperature dependence of other thermal conductivity models arises from the inherent temperature dependence of the individual phases. Figure 6.2 illustrates the difference in the predicted thermal conductivity enhancement versus temperature relationship for several models. Note that the Brownian motion models by Jang and Choi [131], Chon et al. [50], and Prasher et al. [136] display a monotonically increasing thermal conductivity as the temperature rises, but the other models exhibit thermal conductivity enhancements which are relatively constant with temperature. This temperature dependence due to the Brownian motion of the nanoparticles can be seen in the Stokes – Einstein relation,

$$D = \frac{k_B T}{3\pi\mu d} \tag{6.1}$$

where D is the diffusivity of the particle, k_B is the Boltzmann constant, T is the temperature, μ is the viscosity, and d is the radius of the particle. The diffusivity contains both direct and indirect temperature dependence because of the viscosity, and the temperature dependence is greater than first order. In many of the Brownian motion models, the thermal conductivity is directly proportional to the diffusivity or velocity of the suspended particles. Consequently, the relationship between the thermal conductivity of a nanofluid and temperature greater than first order. However, the experimental results clearly demonstrate curvature in the thermal conductivity versus temperature behavior for each nanofluid, as illustrated in Figures 5.4, 5.7 – 5.8. Each nanofluid exhibits a maximum thermal conductivity at approximately the same temperature as the

maximum observed for the pure fluid. Figure 6.3 displays the thermal conductivity of the nanofluids consisting of alumina in ethylene glycol

These results suggest that the thermal conductivity versus temperature behavior of the nanofluid closely follows the behavior of the base fluid. Due to their strong temperature dependence, the Brownian motion based models are incapable of fitting these experimental results. A more appropriate thermal conductivity model would contain no direct temperature dependence, but would be approximately proportional to the thermal conductivity of the base fluid, similar to the Maxwell model. A comparison between the Maxwell model and the experimental data in Figure 6.3 illustrates the similarity between the experimental and theoretical relationship between the thermal conductivity of nanofluids and temperature.

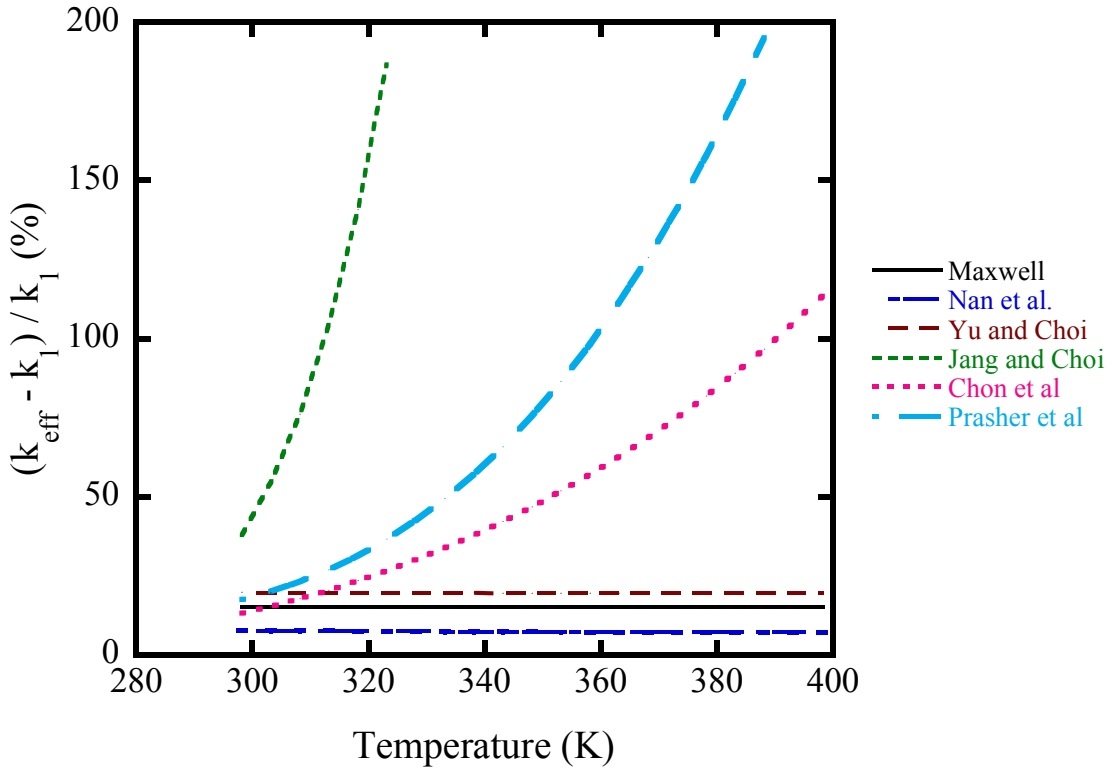

Figure 6.2 Thermal conductivity enhancement predictions for an aqueous nanofluid containing 5 % (v/v) alumina (40 nm) from several models as a function of temperature.

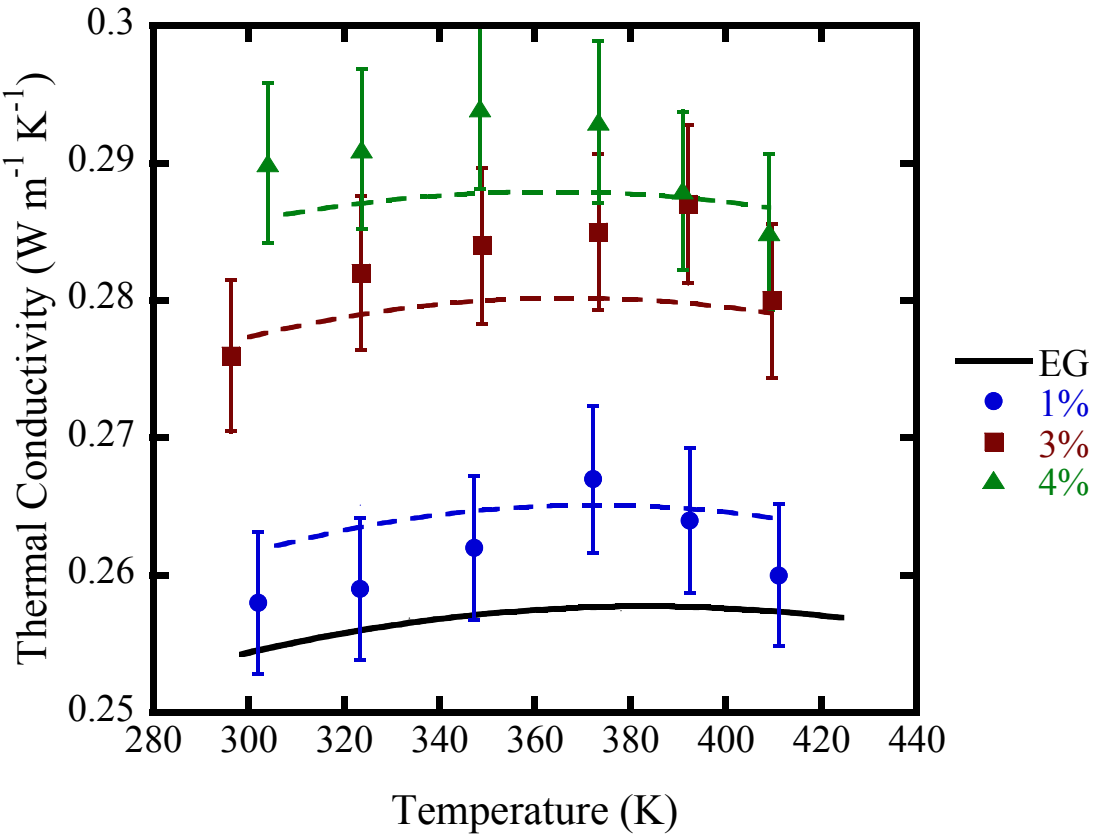

Figure 6.3 Thermal conductivity of ethylene glycol and nanofluids consisting of ethylene glycol and alumina nanoparticles (diameter = 12 nm). Each data set represents a different volume fraction of alumina (calculated at room temperature). The dashed lines represent the Maxwell equation for each concentration. The error bars represent estimated error for the measurements.

6.1.3 Thermal Conductivity of Individual Phases

As the ratio of solid to liquid thermal conductivity, α, increases, the thermal conductivity predictions from the Maxwell equation approach a limiting value, which is only dependent on the particle volume fraction and the thermal conductivity of the liquid. The following equation is obtained from the Maxwell equation when $\alpha >> 1$.

$$k_{eff} = k_1\left(1+\frac{3\phi}{1-\phi}\right) \tag{6.2}$$

This shows that the thermal conductivity of a nanofluid does not depend on the solid thermal conductivity when $\alpha >> 1$ or $k_2 >> k_1$. (Note that the thermal conductivity enhancement is also independent of the liquid thermal conductivity.) However, this limiting value given by eq. 6.2 is not observed experimentally. Xie et al. [59] measured the thermal conductivity of alumina nanoparticles in various base fluids and observed that the relative thermal conductivity enhancement of the nanofluid was greater for less conductive fluids (greater α). In this work, nanofluids consisting of ethylene glycol and alumina exhibited greater thermal conductivity enhancement than the aqueous nanofluids containing the same concentration of the same size of alumina particles.

Turian et al. [48] observed this deficiency in the Maxwell model and similar models [124-126]. They found that deviations between thermal conductivity predictions of the Maxwell equation and experimental data increased as α increased, and that the volume fraction – weighted geometric mean provided more accurate predictions of the thermal conductivity of solid – liquid dispersions when α is high ($\alpha > 70$),

$$\frac{k_{eff}}{k_1} = \alpha^{\phi} \tag{6.3}$$

A comparison of thermal conductivity predictions from the geometric mean and the Maxwell equation are compared with the data from Xie et al. [59] in Figure 6.4. The geometric mean exhibits a relationship between the thermal conductivity and α that is similar to the empirical trend. Furthermore, the geometric mean predictions are within 6 % (within 1 % for $\alpha \leq 150$) of the experimental data while the predictions from the Maxwell equation deviate from the experimental data by as much as 23 %.

The geometric mean is compared with the Hashin and Shtrikman (HS) bounds in Figure 6.5. The HS bounds represent the limits of thermal conductivity throughout the range of spatial arrangement of particles in suspension. Note that the lower HS bound is the same as the Maxwell equation. Thus, the lower HS bound represents the thermal conductivity of a dispersion containing homogeneously dispersed particles with no particle interactions. Consequently, aggregation of suspended particles promotes conduction and yields a greater thermal conductivity than that predicted by Maxwell. The upper HS bound represents the arrangement of particles that maximizes the thermal conductivity of a dispersion. Also the thermal conductivity of the upper HS bound increases monotonically with increasing α, and the lower HS bound reaches a limiting value. Thus, the thermal conductivity of dispersions is a function of α due to aggregation of the particles and is best represented by the volume fraction – weighted geometric mean.

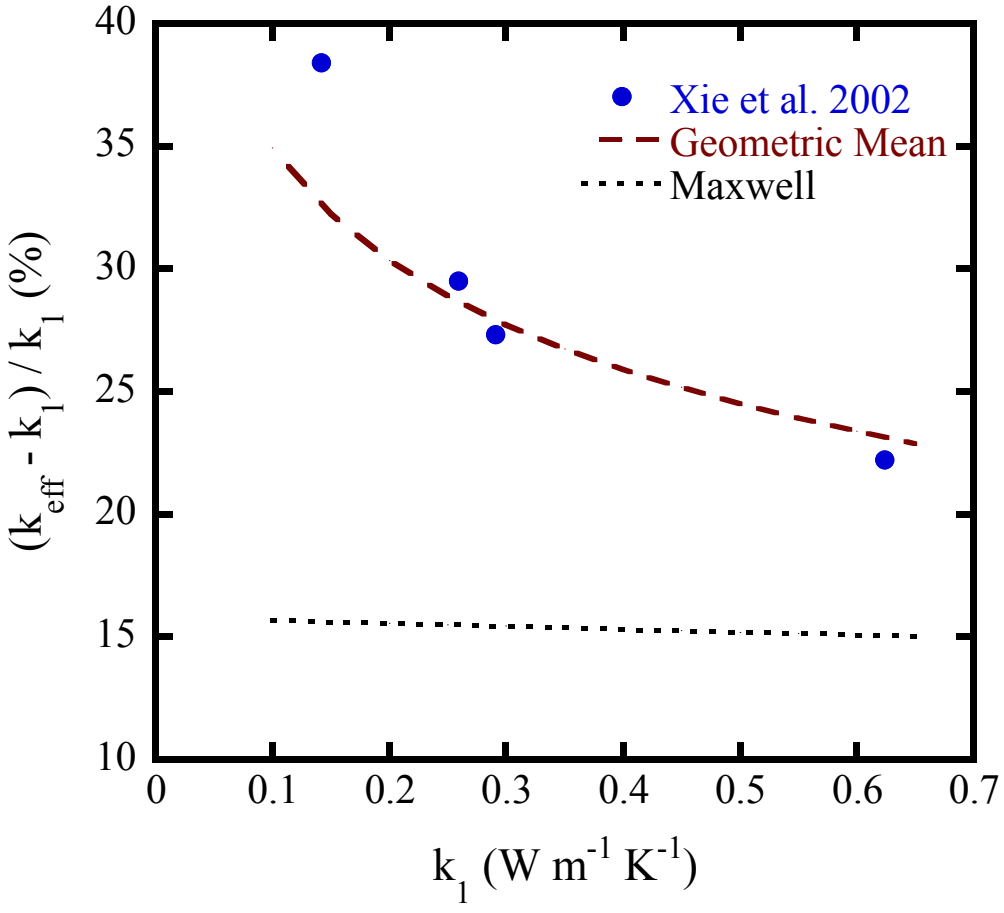

Figure 6.4 The thermal conductivity of 5 % (v/v) alumina in pump oil, ethylene glycol, glycerol, and water from Xie et al. [59]. The dashed lines represents the volume fraction weighted geometric mean or the Maxwell equation.

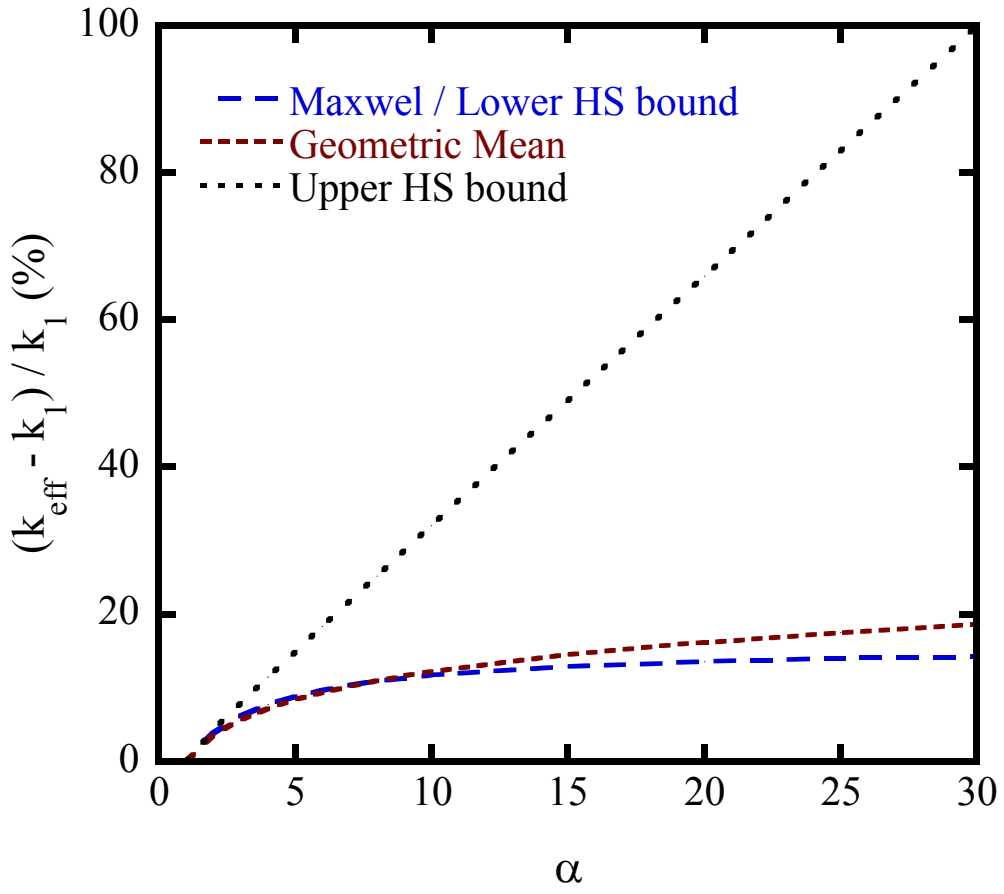

Figure 6.5 The Hashin and Shtrikman bounds for the thermal conductivity of a heterogeneous material as a function of the ratio of the individual phase thermal conductivies (α). The lower bound is equivalent to the Maxwell model. The volume fraction in these calculations is 5 %.

6.1.4 Particle Diameter

The models for the thermal conductivity of nanofluids exhibit an inverse relationship between thermal conductivity and particle diameter. In the Brownian motion based models, the size dependence typically arises from the Brownian velocity. In the ordered liquid layer models, the particle diameter is related to the total surface area, which determines the volume of ordered liquid molecules. Figure 6.6 displays a comparison of thermal conductivity predictions from various models and their relationship with particle diameter. These types of models yield thermal conductivity predictions that increase as the particle size decreases below a threshold. For example, the predictions of the Yu and Choi [140] model are weakly dependent on particle size above a diameter of 20 nm. However, below 20 nm, the thermal conductivity exhibits a strong particle size dependence. This inverse relationship between the thermal conductivity and the particle size has not been validated experimentally.

The experimental data in this work (Tables 4.10 – 4.12) exhibits a relationship between the thermal conductivity of the dispersion and the particle size similar to that exhibited by the Nan et al. [155] model. As illustrated in Figure 6.7, the thermal conductivity of the dispersion decreases with decreasing particle size. A decrease in thermal conductivity enhancement was also observed for decreasing particle size in aqueous ceria nanofluids (Figure 4.11). The thermal conductivity models for nanofluids are incapable of fitting these results due to their inverse dependence between thermal conductivity and particle size. The model by Nan et al. is the only available model that exhibits decreasing thermal conductivity with decreasing particle size. They attributed this trend to thermal resistance at the interface of the solid nanoparticles and the liquid. .

The interfacial thermal resistance is defined as a temperature discontinuity at the interface. Thus, it is an empirical phenomenon and can be caused by various mechanisms such as phonon dynamics and poor contact between the individual phases. In nanofluids, the thermal resistance is most likely phonon boundary scattering occurring at the interface of the solid and liquid. A number of studies [38, 40, 44] have experimentally demonstrated lower thermal conductivity of silicon nanomaterials attributed to phonon boundary scattering. Also, the thermal conductivity of solids is lower when the solid dimensions are confined. For example, the thermal conductivity of nanowires is less than that for nanofilms when the diameter of the wire is comparable to the thickness of the film as a result of confinement in two dimensions instead of one [43]. Consequently, nanoparticles should exhibit lower thermal conductivity than either wires or films due to confinement in three dimensions. The thermal conductivity of nanofluids consisting of titania (d = 2 nm) in a mixture of ethylene glycol and water exhibited thermal conductivity less than the mixture without particles (Figure 5.9). Furthermore, the thermal conductivity decreased with increasing particle concentration. These results suggest that the thermal conductivity of the titania is less than the thermal conductivity of the fluid. Thus, the thermal conductivity of solid nanoparticles should be represented by a model which is a function of the particle size rather than incorporating the particle size dependence into the model for the dispersion.

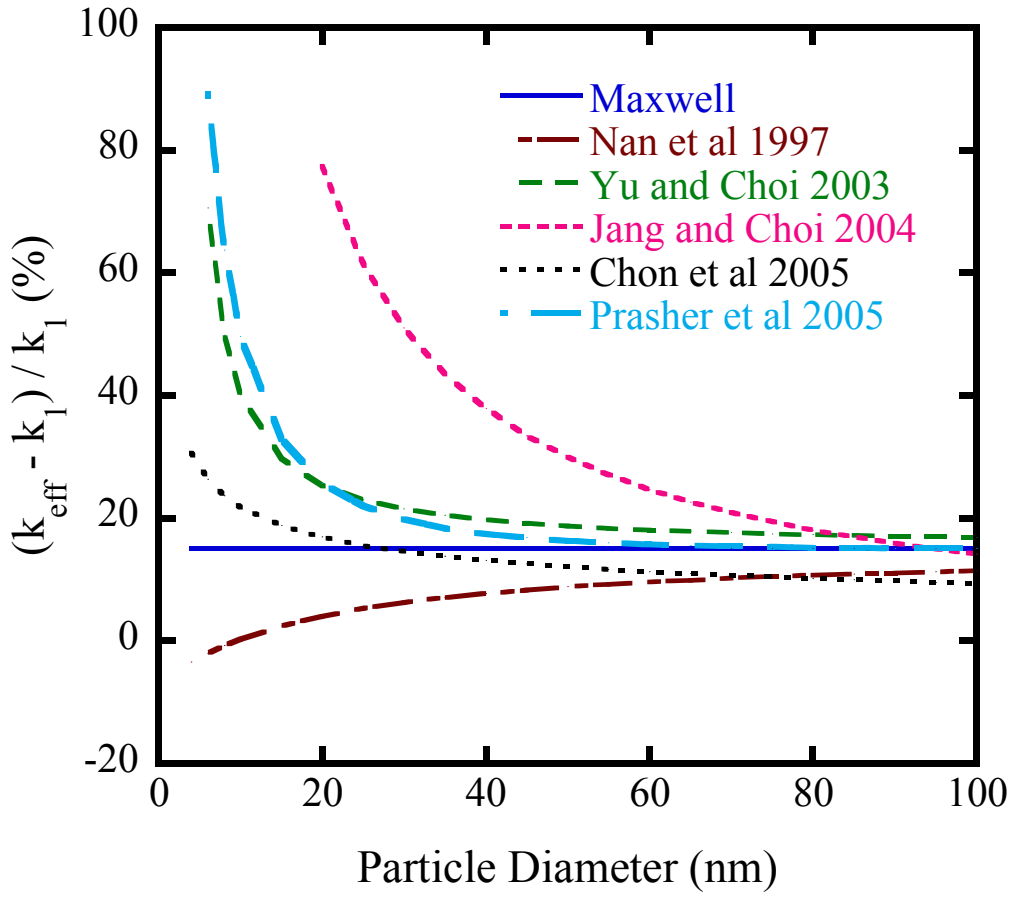

Figure 6.6 Thermal conductivity enhancement predictions for an aqueous nanofluid containing 5 % (v/v) alumina at room temperature from several models as a function of particle diameter.

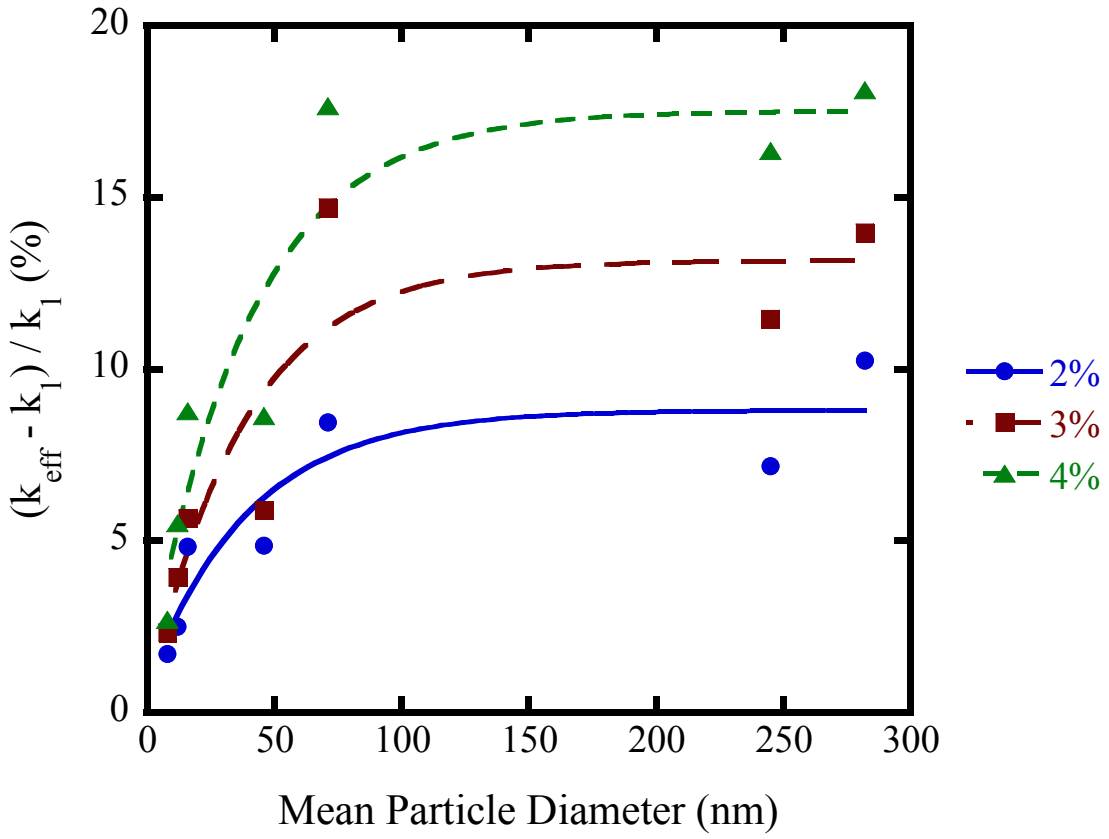

Figure 6.7 Thermal conductivity enhancement of aqueous nanofluids containing 2 - 4 % (v/v) alumina at room temperature. Empirical curve fits are provided to aid in visual detection of trends in the data.

6.1.5 Geometric Mean

All of the published models for the thermal conductivity of nanofluids represent the enhancement versus volume fraction trend well, as shown in Figure 6.1 and discussed in section 6.1.1. However, the relationship of the enhancement with temperature, α, and particle size is not represented adequately by any of the models as discussed in the previous three sections (6.1.2 – 6.1.4). Based on this analysis in the previous sections, only two models are capable of predicting three of these four observed trends, the model by Nan et al. and the volume fraction – weighted geometric mean.

The model by Nan et al. [155] displays trends that reflect the behavior of the thermal conductivity as a function of particle volume fraction, temperature, and particle diameter. However, the model reduces to the Maxwell model at large particle size and includes the same deficiency in reflecting the relationship between the thermal conductivity of the dispersion and the thermal conductivities of the individual phases. Figure 6.8 displays a comparison of predictions from the Nan et al. model compared to the Maxwell model and experimental data. The Nan et al. model is incapable of predicting the thermal conductivities of these nanofluids containing larger particles (d > 50 nm).

The volume fraction – weighted geometric mean reflects the empirical trends between the thermal conductivity and the particle volume fraction, temperature, and the thermal conductivities of the individual phases. Figure 6.9 displays experimental data and the corresponding predictions from the geometric mean. The geometric mean yields predictions that are within 2 % of the experimental values for the dispersions containing larger particles (d > 50 nm), but it contains no direct particle size dependence. However,

the thermal conductivity of the solid is dependent on the particle size in the nanoscale range (section 3.2.2). Therefore, a particle size dependence can be incorporated into the volume fraction – weighted geometric mean through the thermal conductivity of the solid particles.

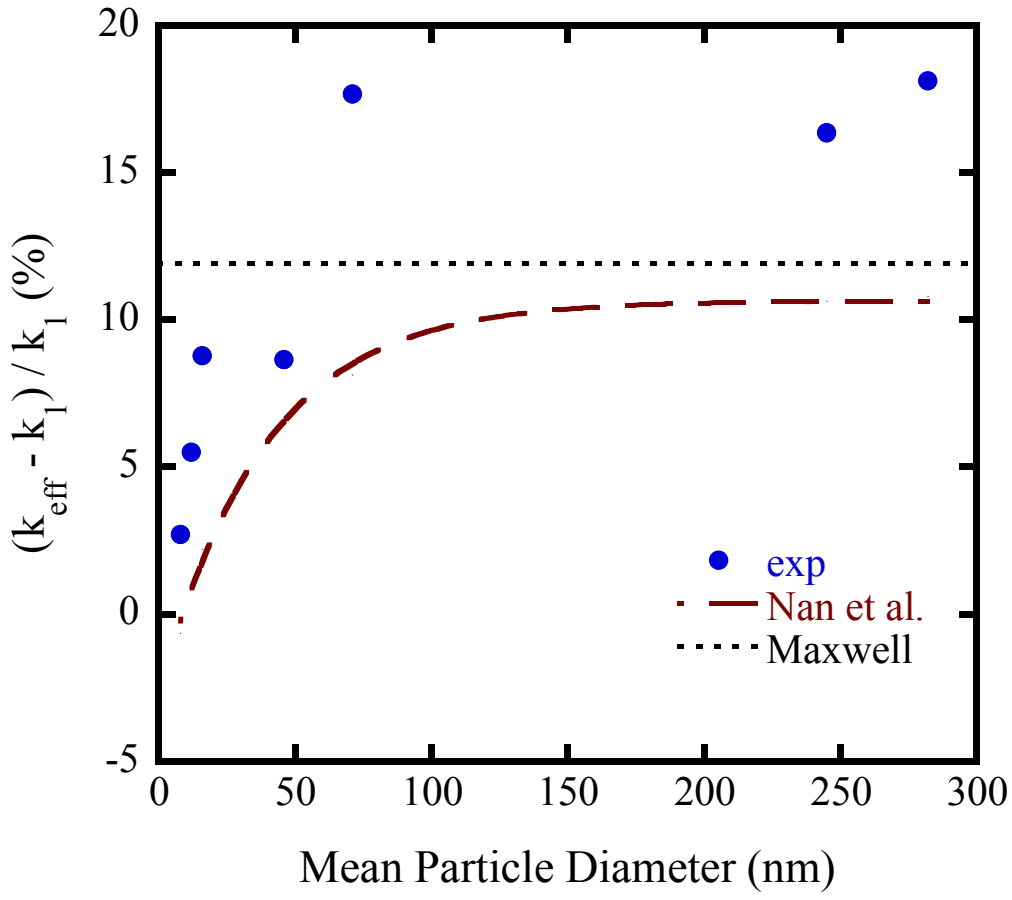

Figure 6.8 Thermal conductivity enhancement of aqueous nanofluids containing 4 % (v/v) alumina at room temperature. The Nan et al. [155] model and the Maxwell model [118] are provided for comparison. The thermal conductivity of bulk alumina (40 W m^{-1} K^{-1}) was used in the predictions.

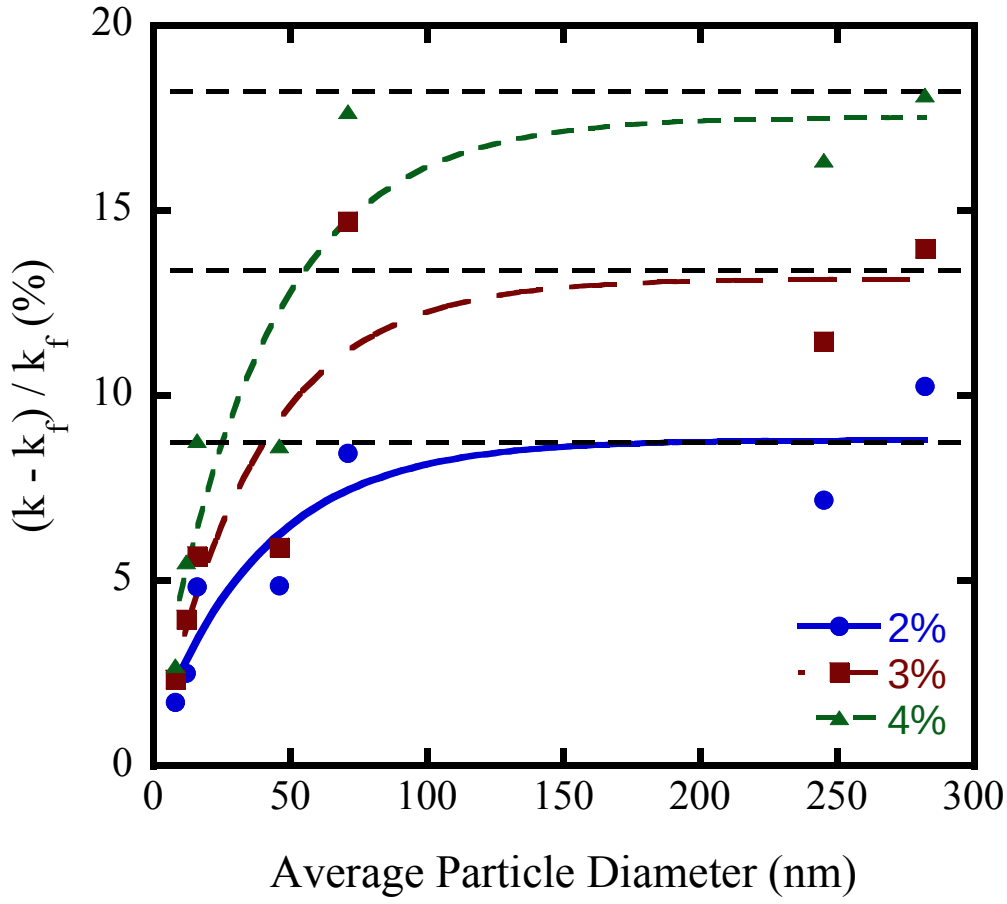

Figure 6.9 Thermal conductivity enhancement of aqueous nanofluids containing 2 - 4 % (v/v) alumina at room temperature. Empirical curve fits are provided to aid in visual detection of trends in the data. The dashed lines represent the volume fraction weighted geometric mean at each concentration using the bulk alumina thermal conductivity (40 W m^{-1} K^{-1}).

6.2 Size Dependent Particle Thermal Conductivity

Molecular dynamics studies by Ziambaras and Hyldgaard [43] and Fang et al. [45] predict that the thermal conductivity of nanomaterials increases linearly with particle size at small sizes and eventually attains the bulk thermal conductivity at larger particle sizes. It is therefore proposed here that the thermal conductivity of the particle be represented by the following equation,

$$k_2(d) = k_{bulk}\left(1 - e^{-A_1 d}\right) \tag{6.4}$$

where k_{bulk} is the thermal conductivity of the bulk material (40 W m^{-1} K^{-1} for alumina [19]) and A is an empirical parameter. To estimate this parameter, the thermal conductivity of each size of alumina particles was estimated by performing a least squares fit of the geometric mean to the experimental data of the aqueous nanofluids (Table 5.10) as displayed in Figure 6.10. The semi-empirical fit and the estimated thermal conductivities of alumina particles versus average particle diameter are displayed in Figure 6.11. The error bars represent the experimental error in the thermal conductivity measurement of the fluid. The following equation was found with the least squares method to find the fitted parameter,

$$k_2(d) = \left(40\frac{W}{m \cdot K}\right)\left(1 - e^{-\left(0.0126\,nm^{-1}\right)d}\right). \tag{6.5}$$

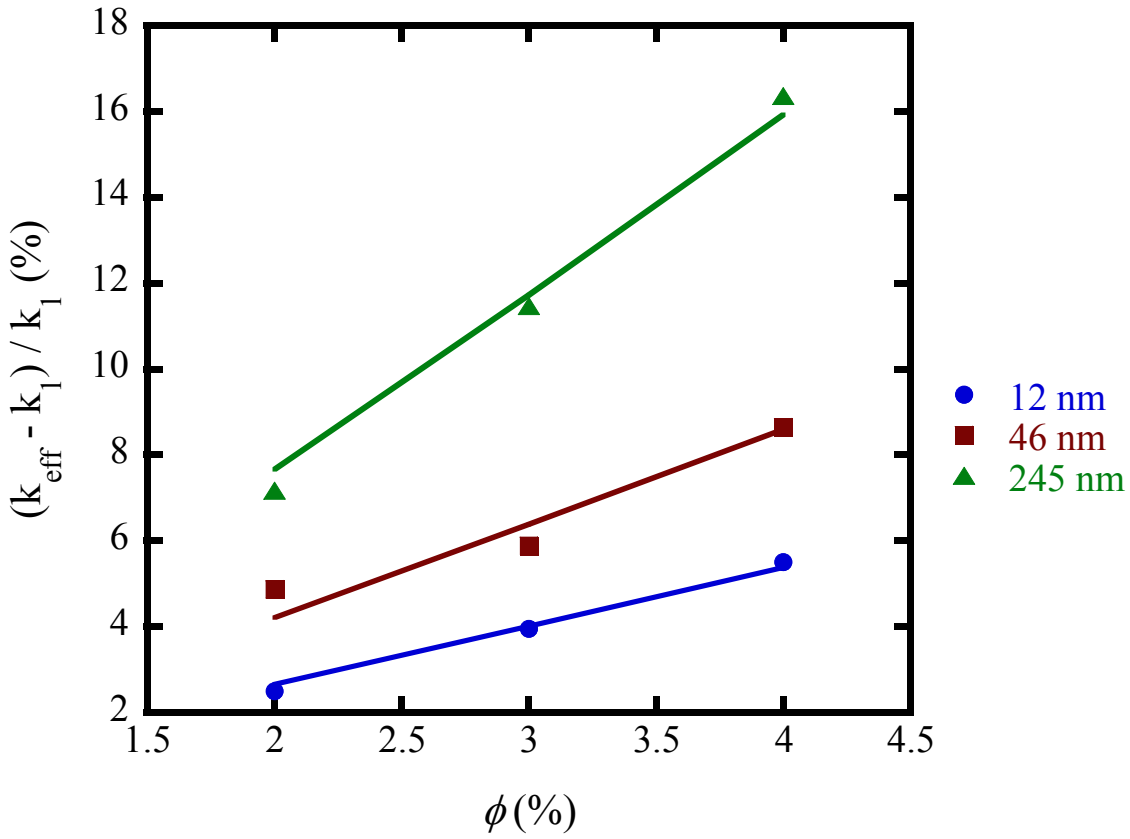

Figure 6.10 Thermal conductivity enhancement of aqueous nanofluids containing alumina at room temperature for various mean particle diameters. The lines represent least squares fits of the volume fraction weighted geometric mean by adjusting the thermal conductivity of the particle (k_2).

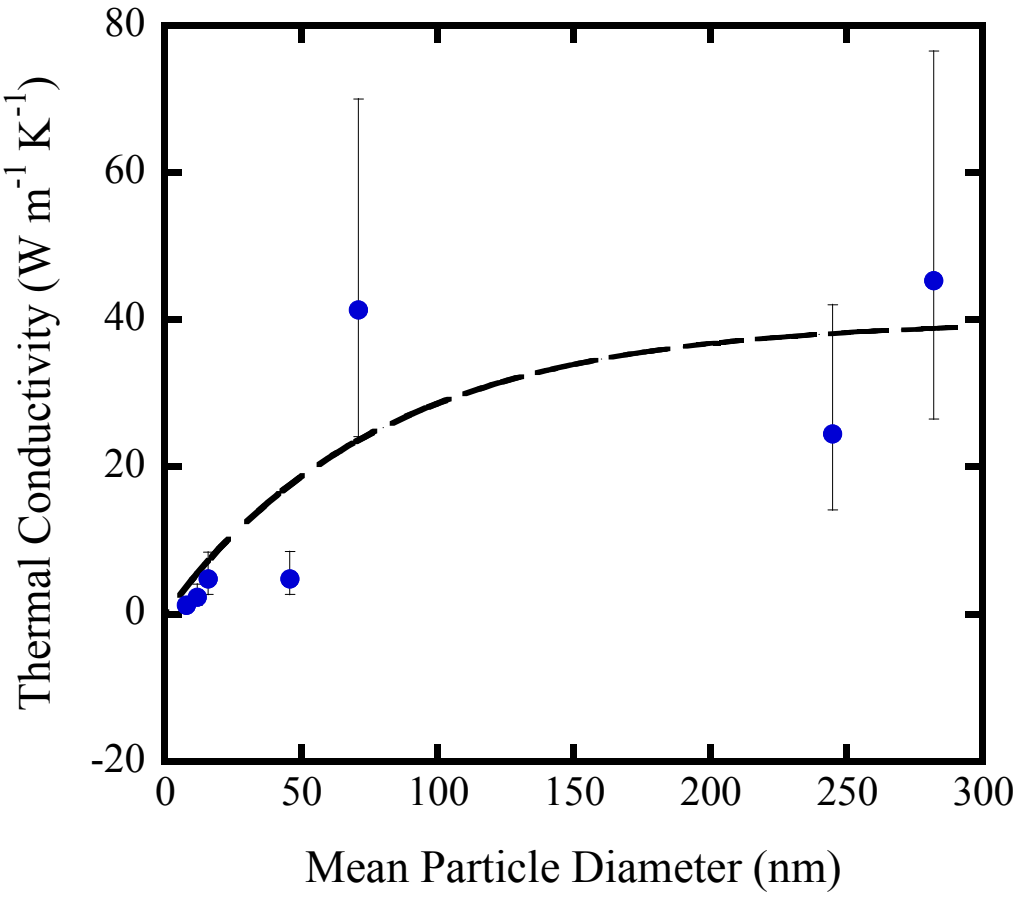

Figure 6.11 Estimated thermal conductivity of alumina particles from the volume fraction weighted geometric mean. The curve represents a semi-empirical fit (eq. 6.5).

6.3 Prediction of Thermal Conductivity of Nanofluids

Equation 6.5 and the geometric mean were used to predict the thermal conductivity of alumina in ethylene glycol as a function of temperature and particle size. Figures 6.12 and 6.13 display comparisons of these predictions of thermal conductivity enhancement with the experimental data from this study. The predictions are all within 1.5 % of the experimental data in Figure 6.12 and within 2.3 % in Figure 6.13. Figure 6.14 displays a comparison between the predictions of the model and experimental data as a function of α from this work and that of Xie et al. [59]. The predictions were within 4 % of the data of Xie et al. and within 2 % of the data from this work. Additionally, these equations provided predictions within 4 % of the experimental data from Xie et al. [12] (Figure 6.15) and within 1 % of Eastman et al. [60] (Figure 6.16). Furthermore, these equations provided predictions within 4.8, 4.5, 2.2, and 1.8 % of the measured values of Lee et al. [57], Wang et al. [53], Kim et al. [13], and Yoo et al. [55], respectively. However, some experimental thermal conductivity data deviates from predictions of this model due to a temperature dependence which conflicts with the results of this work [8, 9, 50, 52]. The reasons for other discrepancies between the measured thermal conductivity and these predictions are unknown [49, 51, 58].

The dearth of thermal conductivity data for nanofluids containing different particle sizes makes it difficult to apply this model to other systems. Thermal conductivity data is available for CuO nanofluids containing particles between 23 and 36 nm [11, 18, 53, 57, 60, 65], but this size range is too narrow to obtain a reliable correlation between thermal conductivity and particle size. However, the model is capable of fitting data available in the literature for CuO nanofluids because the measured

values are less than the maximum value of the model given by the geometric mean with the thermal conductivity of the bulk solid. Alternatively, the model is incapable of predicting the measured thermal conductivity values for nanofluids containing more conductive particles such as Cu [25, 49, 60, 71-74], diamond [32], Ag [32, 77], Au [73] or alloys [81-83]. Specifically, the maximum predicted thermal conductivity enhancement for a nanofluid consisting of 0.3 % (v/v) Cu in ethylene glycol is 2.1 %, whereas the measured value was 40 % [74]. In addition, the maximum predicted thermal conductivity enhancement for a nanofluid consisting of 1.3 % (v/v) diamond particles in ethylene glycol is 11.2 %, and the measured value was 75 % [32]. Further comments about the available thermal conductivity studies in relation to this new model are provided in Table 6.1. Studies of nanofluids containing particles which were not spherical or nearly spherical were not considered, since the effect of particle shape has not been incorporated into the model [10, 24, 27, 75, 84-93].

Thus, the volume fraction – weighted geometric mean with a single parameter semi-empirical equation for the solid thermal conductivity is capable of predicting the thermal conductivity of nanofluids containing alumina, but it unproven with other systems. Furthermore, the model is not appropriate for predicting the thermal conductivity of nanofluids containing highly thermally conductive particles such as copper, silver, or diamond.

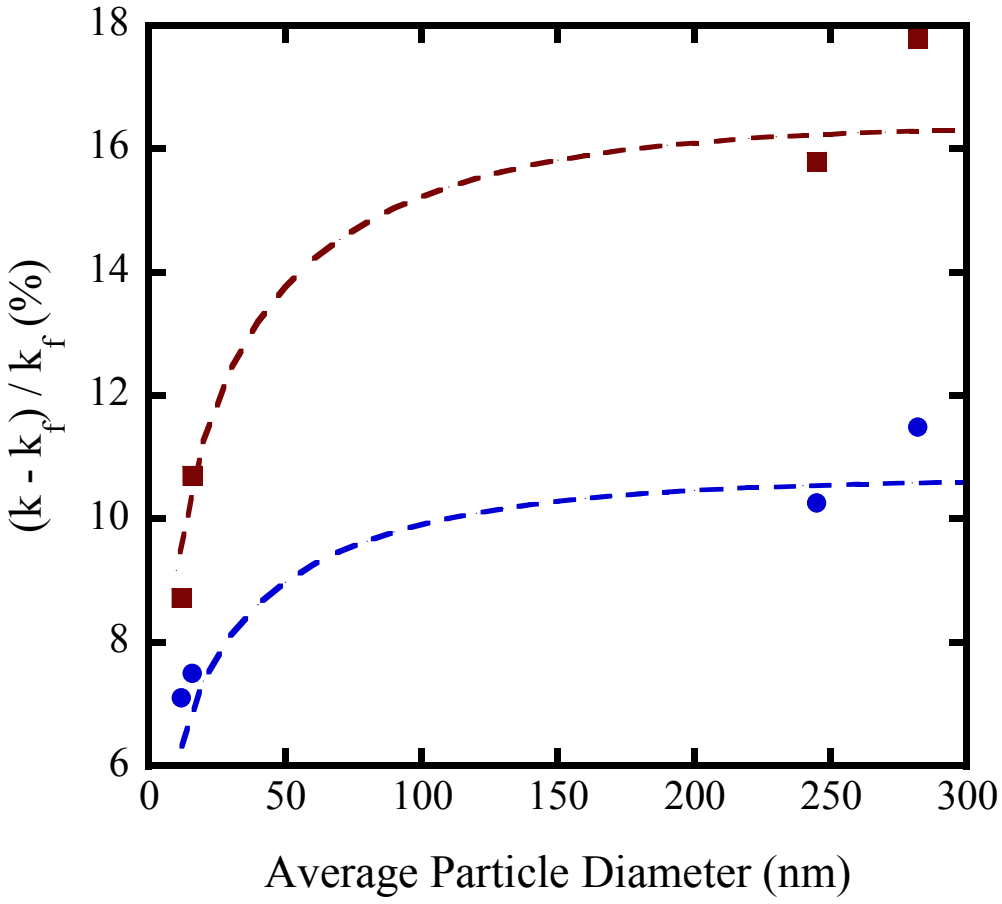

Figure 6.12 Thermal conductivity enhancement of nanofluids consisting of 2 and 3 % (v/v) alumina in ethylene glycol at room temperature. The circles and squares represent experimental data at 2 % and 3 % respectively. The dashed lines represent predictions using Equation 6.5 with the volume fraction weighted geometric mean.

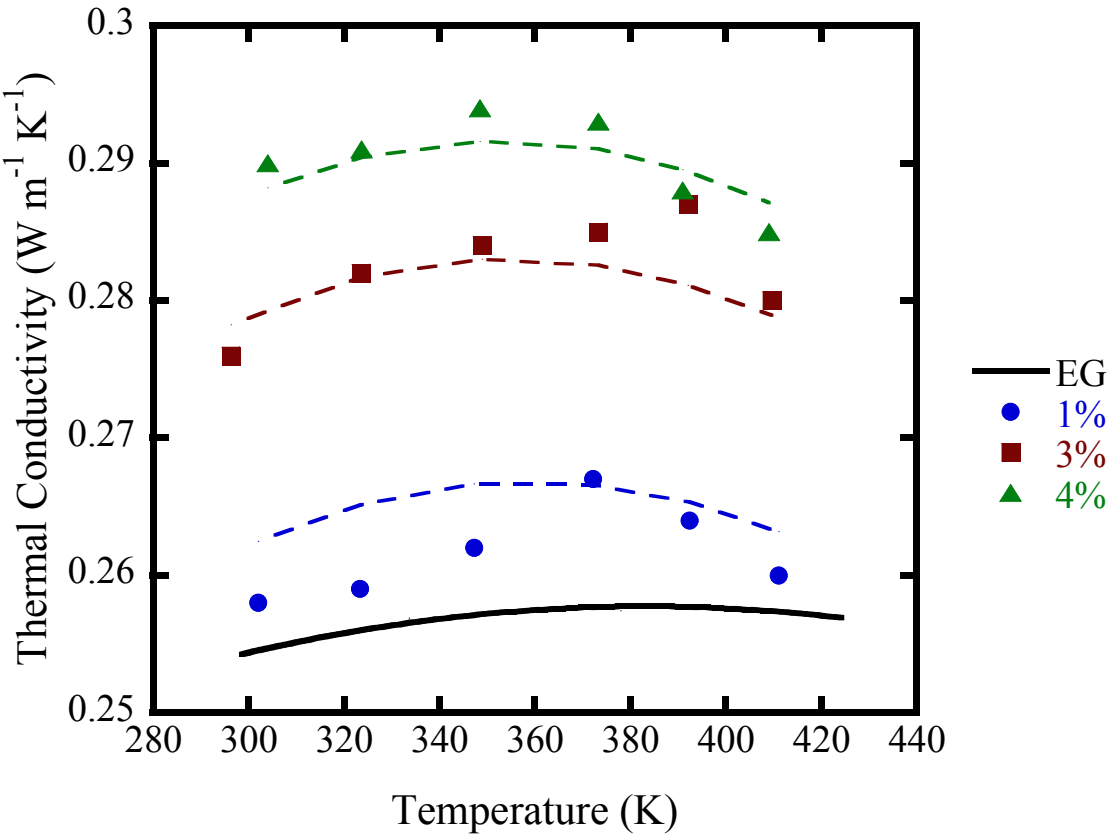

Figure 6.13 Thermal conductivity of ethylene glycol and nanofluids consisting of ethylene glycol and alumina nanoparticles (diameter = 12 nm). Each data set represents a different volume fraction of alumina (calculated at room temperature). The dashed lines represent predictions using Equation 6.5 with the volume fraction weighted geometric mean.

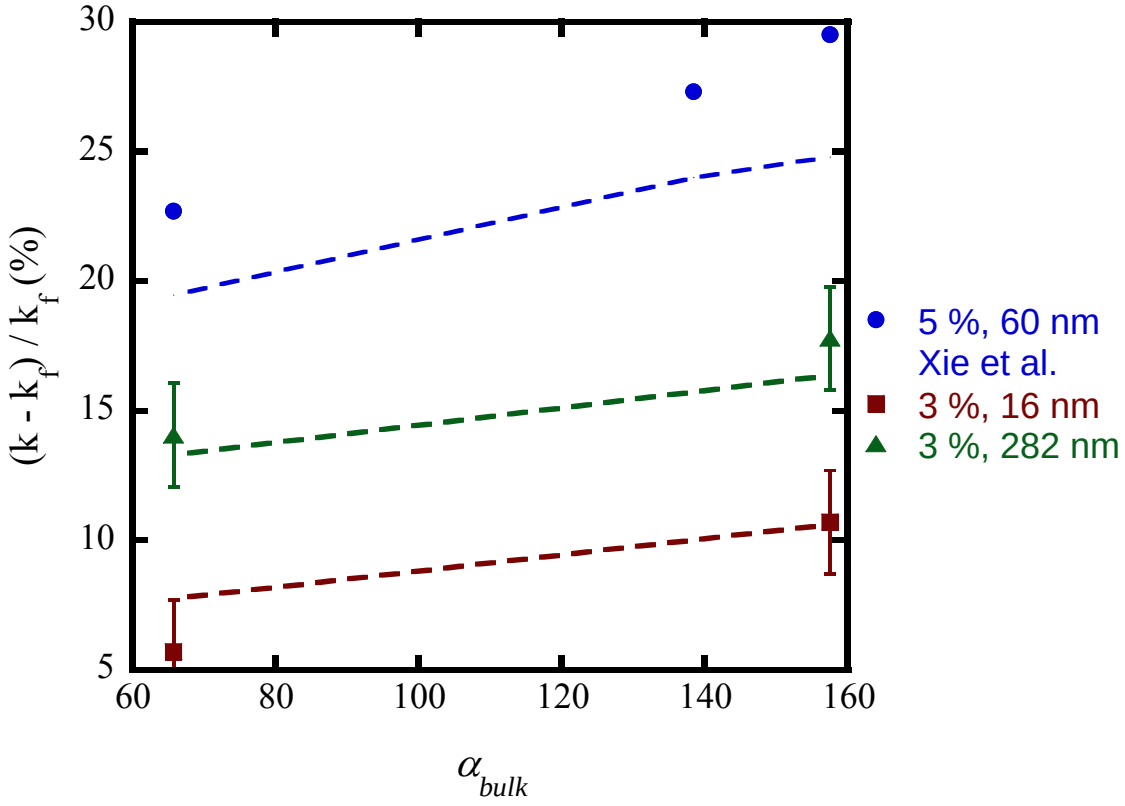

Figure 6.14 Thermal conductivity of alumina nanofluids as a function of α_{bulk} from this work and the work of Xie et al. [59]. The thermal conductivity of the bulk solid was used to determine α_{bulk}. The dashed lines represent predictions using Equation 6.5 with the volume fraction weighted geometric mean.

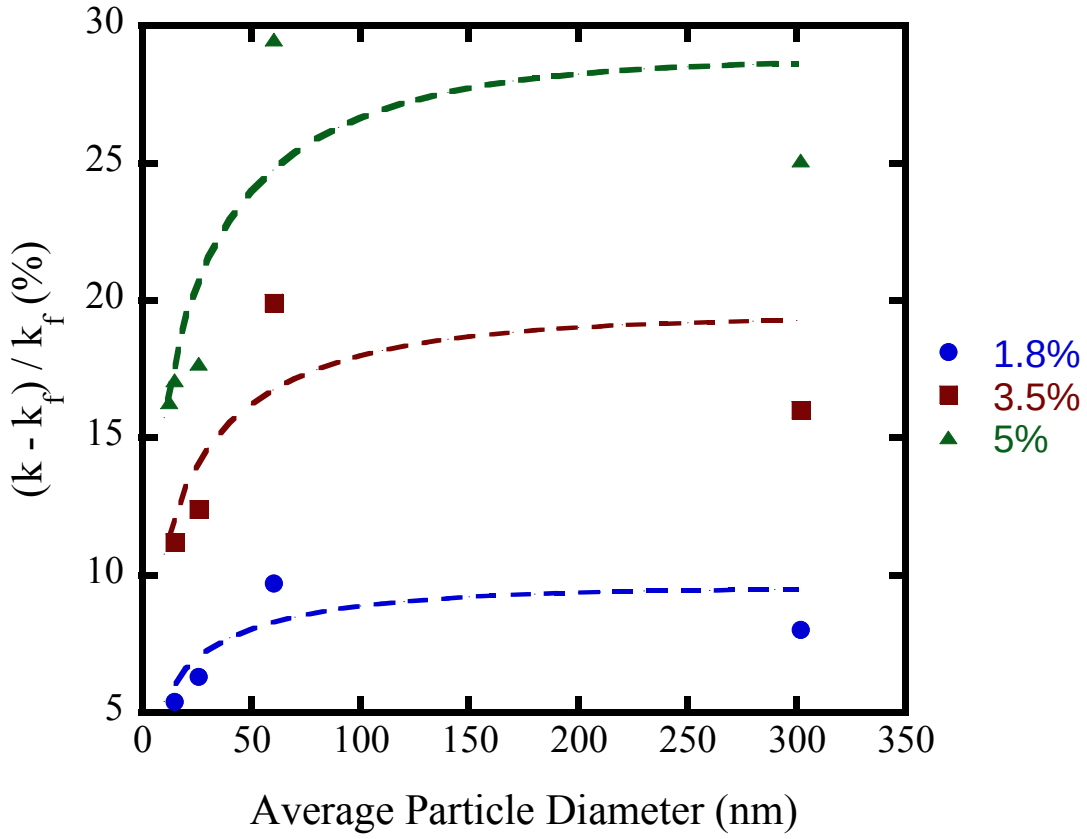

Figure 6.15 Thermal conductivity enhancement of nanofluids consisting of alumina in ethylene glycol at room temperature from Xie et al. [12]. The dashed lines represent predictions using Equation 6.5 with the volume fraction weighted geometric mean.

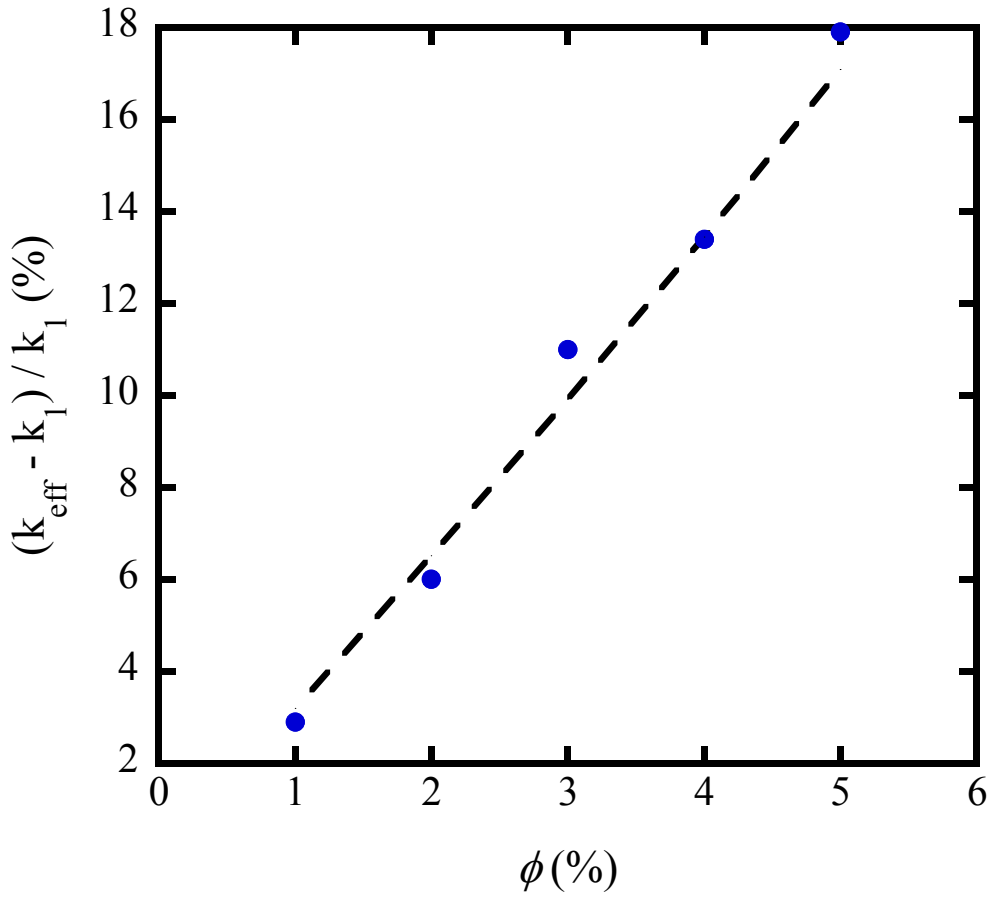

Figure 6.16 Thermal conductivity enhancement of aqueous nanofluids containing alumina (diameter = 35 nm) from Eastman et al. [60]. The dashed line represents a prediction using Equation 6.5 with the volume fraction weighted geometric mean.

Table 6.1 Deviations between thermal conductivity model predictions and experimental values available in the literature

Authors and Reference	Nanofluids	Maximum deviation of data from model*	Comments
Eastman et al. 1997 [49]	Al_2O_3 / Water CuO / Water	10 % 24 %	Data has not been reproduced by others
Eastman et al. 1999 [60]	Al_2O_3 / Water CuO / Water	1 % 5 %	
	Cu / Ethylene Glycol	Maximum > geometric mean	
Lee et al. 1999 [57]	Al_2O_3 / Water Al_2O_3 / Ethylene Glycol CuO / Water CuO / Ethylene Glycol	5 % 4 % 5.4 % 2 %	
Wang et al. 1999 [53]	Al_2O_3 / Water Al_2O_3 / Ethylene Glycol Al_2O_3 / Engine Oil Al_2O_3 / Pump Fluid CuO / Water CuO / Ethylene Glycol	2.3 % 7.5 % 8 % 16 % 13 % 23 %	
Xie et al. 2002 [12, 59]	Al_2O_3 / Water Al_2O_3 / Ethylene Glycol Al_2O_3 / Pump Oil	4.4 % 4 % 7.3 %	
Xie et al. 2002 [70]	SiC / Water SiC / Ethylene Glycol	22 % 28 %	
Das et al. 2003 [8]	Al_2O_3 / Water CuO / Water	Temperature dependence of data is apparently erroneous	
Chon et al. 2005 [50]	Al_2O_3 / Water	Temperature dependence of data is apparently erroneous	
Kwak and Kim 2005 [64]	CuO / Ethylene Glycol	1.2 %	
Murshed et al. 2005	TiO_2 / Water	20 %	> maximum model predictions
Hwang et al. 2006, 2007 [18, 62]	CuO / Water CuO / Ethylene Glycol SiO_2 / Water CNT / Water CNT / Mineral Oil	1.3 % 4.1 % 4.3 % NA NA	 not spherical not spherical
Lee et al. 2006 [63]	CuO / Water	10 %	
Li and Peterson 2006, 2007 [9]	Al_2O_3 / Water CuO / Water	Temperature and particle size dependence are apparently erroneous	
Liu et al. 2006 [65]	CuO / Ethylene Glycol	2.5 %	

Table 6.1 (continued)

Zhang et al. 2006, 2007 [11, 51, 54]	Al_2O_3 / Water CuO / Water TiO_2 / Water CNT / Water Au / Toluene	7 % 24 % 4 % 2 % NA NA	when $\phi < 6$ % when $\phi > 6$ % not spherical no enhancement ($\phi = 0.003$ %)
Kim et al. 2007 [13]	Al_2O_3 / Water Al_2O_3 / Ethylene Glycol	2 % 2.2 %	
	ZnO / Water ZnO / Ethylene Glycol TiO_2 / Water TiO_2 / Ethylene Glycol	Particle size dependence of data are apparently erroneous	
Yoo et al. 2007 [55, 56]	Al_2O_3 / Water TiO_2 / Water WO_3 / Ethylene Glycol Fe / Ethylene Glycol	2 % 12 % NA 14 %	
Timofeeva et al. 2007 [58]	Al_2O_3 / Water Al_2O_3 / Ethylene Glycol	Particle size dependence of data are apparently erroneous	
Wang et al. 2007 [67]	TiO_2 / Water SiO_2 / Water SiO_2 / Ethylene Glycol SiO_2 / Ethanol	6.1 % 3.3 % 3.4 % 3.7 %	

* Maximum deviation of data from model is defined as $\left(k_{measured} - k_{predicted}\right)/k_{predicted}$

Model predictions were obtained using $k_2(d) = k_{bulk}\left(1 - e^{-\left(0.0126\,nm^{-1}\right)d}\right)$.
Note that the exponent is the same as that for alumina.

6.4 Particle Size Polydispersity

The relationship between the thermal conductivity of the solid and particle size raises a concern about the use of mean particle size to characterize the samples. Some of the particle samples in this study have more polydisperse distributions than others. Specifically, the alumina nanoparticles with an average size of 46 nm and 71 nm have a much greater standard deviation than the other samples as observed in the TEM images (see Table 4.3). The range of particle diameters observed in TEM images was 14 – 260 nm for the 71 nm average diameter particles (Figure 6.17). Similarly, the range was 8 – 370 nm for the 46 nm average diameter particles (Figures 4.2 and 6.18). When studying the thermal conductivity of the solid particles, the primary size distribution would be a more appropriate characterization than the average particle size. However, the size distribution is quite difficult to measure in aggregated particles. The use of average particle size to characterize polydisperse particle samples is especially poor when the thermal conductivity versus particle size relationship is not linear over the entire size distribution. Thus, the polydisperse size distribution creates some uncertainty when examining the relationship between size and thermal conductivity. Consequently, the experimental data points representing nanofluids containing polydisperse particles (d = 46 nm and 71 nm) display the largest deviation from the model.

A possible method to incorporate the particle size distribution into the model would be to treat each size of particles separately. For example, for a binodal distribution with particle sizes d_A and d_B, the geometric mean would be written,

$$\frac{k_{eff}}{k_1} = \left(\frac{k_2(d_A)}{k_1} \right)^{\phi_A} \left(\frac{k_2(d_B)}{k_1} \right)^{\phi_B} \tag{6.6}$$

where ϕ_A and ϕ_B are the volume fractions of each size of particle, and the sum of ϕ_A and ϕ_B is the volume fraction of particles in the dispersion. Thus, for a distribution of *n* sizes of particles, the model would be,

$$\prod_i^n \left(\frac{k_2(d_i)}{k_1} \right)^{\phi_i} \tag{6.7}$$

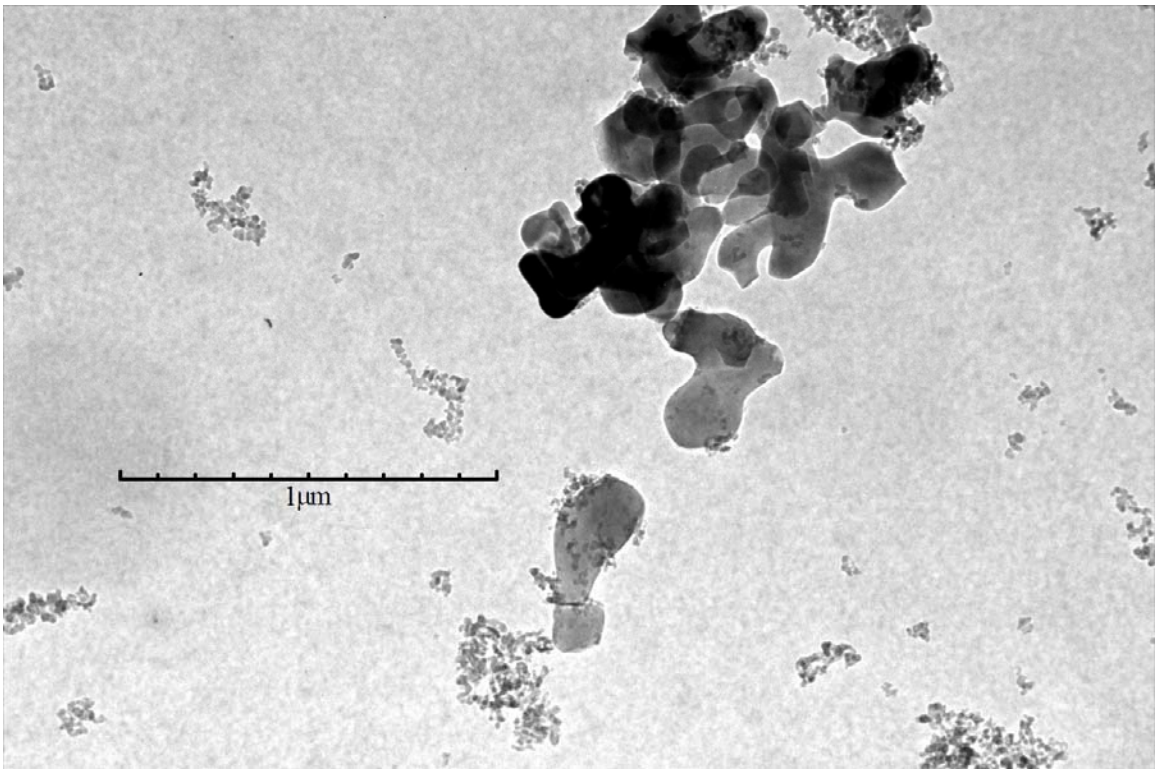

Figure 6.17 Transmission electron microscopy image of alumina particles with a nominal size of 300 nm from Electron Microscopy Sciences. The average diameter of these particles is 99 nm and 71 nm as determined by TEM and BET, respectively. Magnification = 20,000

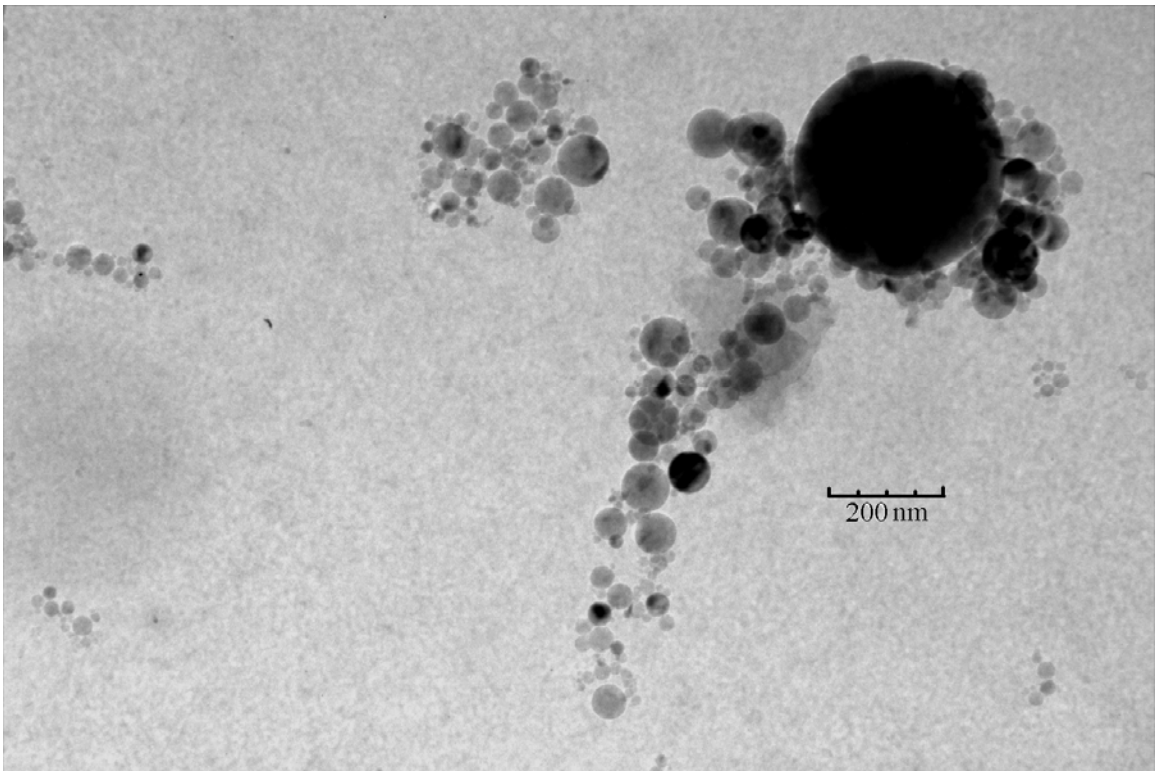

Figure 6.18 Transmission electron microscopy image of alumina particles with a nominal size of 47 nm from Nanophase Technologies The average diameter of these particles is 77 nm and 46 nm as determined by TEM and BET, respectively. Magnification = 30,000

CHAPTER 7

CONCLUSIONS AND RECOMMENDATIONS

7.1 Conclusions

The thermal conductivities of dispersions containing alumina in water, alumina in ethylene glycol, alumina in ethylene glycol + water, and ceria in water were measured with the transient hot wire apparatus at temperatures ranging from 296 K to 422 K and average particle diameters ranging from 8 nm to 282 nm. To date, these measurements cover the largest number of particle sizes in a single study and the widest temperature range considered for any nanofluid.

The effects of temperature and particle size on the thermal conductivity of these nanofluids have been discovered. The temperature dependence arises mostly from the temperature dependence of the thermal conductivity of the liquid. Thus, a maximum was observed in the thermal conductivity versus temperature relationship of nanofluids with water and ethylene glycol as the base fluids. This maximum occurred at approximately the same temperature as the maximum for the base liquid. The thermal conductivity of the nanofluids with smaller particles ($d < 50$ nm) exhibited a lower thermal conductivity than the dispersions containing larger particles.

A semi-empirical predictive model containing a single adjustable parameter was developed based on the experimental thermal conductivity data from aqueous nanofluids containing alumina. The model consists of the volume fraction – weighted geometric mean with a size dependent solid thermal conductivity. Turian et al. [48] demonstrated that the geometric mean provides the most accurate predictions compared with other

models for a wide range of solid-liquid systems. The size dependence of solid thermal conductivity was demonstrated previously for ultrathin films [40] and nanowires [44]. In the present work, the effect of this phenomenon was observed in measurements of nanofluids containing different sizes of nanoparticles. Nanofluids containing smaller nanoparticles (< 50 nm) exhibited an increasing thermal conductivity with increasing particle diameter, and as the particle size increased the thermal conductivity reached a plateau. This plateau is equivalent to the thermal conductivity predictions from the volume fraction – weighted geometric mean using the bulk thermal conductivity of alumina. Thus, the thermal conductivities of each size of alumina particles was estimated from the nanofluid thermal conductivity data by using the geometric mean, and a semi-empirical equation with a single adjustable parameter was fit to this data. The new predictive model yielded values that were within 5 % for several sets of experimental thermal conductivity data for nanofluids containing alumina.

The model presented here is the only available model that reflects observed relationships between the thermal conductivity of nanofluids and the volume fraction (ϕ), temperature (T), particle diameter (d), and the ratio of the individual phase thermal conductivies (α). Specifically, the model is approximately linear at low volume fractions (ϕ < 5 %), which has been demonstrated throughout the literature and in these experiments. Additionally, this model exhibits a temperature dependence similar to the base fluid. This behavior was demonstrated in the measurements of the nanofluids containing ethylene glycol and alumina, where both the nanofluids and pure ethylene glycol exhibited maximum thermal conductivity at approximately the same temperature. Additionally, the decrease in thermal conductivity of the nanoparticles with particle size

predicted by Fang et al. [45] was observed in the thermal conductivity measurements for nanofluids containing alumina and for those containing ceria. Lastly, Xie et al. [59] and Turian et al. [48] observed increasing thermal conductivity enhancement as α increased, and this relationship was also evident in this work for the nanofluids containing the same size of particles, but different base fluids (water and ethylene glycol).

7.2 Future Work

Future work should focus on applying the model presented here to other systems. The semi-empirical equation for the particle thermal conductivity was developed specifically for alumina. The available thermal conductivity data for other nanofluid systems are not as comprehensive as for nanofluids containing alumina, and the relationship between the thermal conductivity of nanofluids and the particle size must be determined for those systems. With this information, one could estimate the adjustable parameter in the particle thermal conductivity equation and try to find a relationship between that parameter and certain solid properties, such as the phonon mean free path. For metal oxides and other ceramics, the difficulty in these experiments would be in obtaining particles of various sizes. However, certain nanofluids have exhibited thermal conductivity enhancement beyond the predictions of this model. These nanofluids often consist of highly thermally conductive solid particles such as diamond [32], carbon nanotubes [7], and metals [74]. There are no studies that focus on the effects of parameters such as temperature and particle size for these systems. A further difficulty is that these systems often require a dispersant to create a stable nanofluid, which makes these ternary systems. Thus, the model would have to be extended to include the effect of the dispersant.

Other work could focus on the spatial arrangement of the particles in the nanofluids. The volume fraction weighted geometric mean represents a spatial arrangement where clusters of particles form small networks of low thermal resistance whereas the Maxwell equation is a theoretical solution for a dispersion where there is no particle interaction [48]. Such an experiment would require fine control over the degree of aggregation of the suspended particles, possibly by adjusting pH and/or the ionic strength. Aggregation appears to enhance conduction in these dispersions to some extent, but extensive aggregation would lead to particle settling. Thus, there may be an optimal degree of aggregation that yields the greatest thermal conductivity enhancement. This experiment may provide greater insight into the specific effect aggregation has on the thermal conductivity of the dispersion.

APPENDIX A

CALIBRATION OF THERMOCOUPLE

A type E thermocouple was used to measure the initial temperature of the fluid before each thermal conductivity measurement. A second junction was held at 0 C in a ice bath during measurements. To calibrate the thermocouple between 25 and 50 ºC, the thermocouple and a RTD probe (ASL Inc. B463712) were placed in a recirculating heater (Thermo NESLAB RTE 740). At each temperature, the voltage of the thermocouple was recorded from a Fluke 8840A multimeter, and the temperature was recorded from an Omega DP251 precision digital thermometer. Above 50 ºC, the thermocouple was calibrated with the same RTD probe in an Omega hot point® dry block probe calibrator.

Table A.1 Calibration of type E thermocouple

Temperature (ºC)	Voltage (mV)
24.99	1.483
30.00	1.792
34.95	2.097
39.93	2.407
44.94	2.722
49.95	3.041
70.06	4.260
90.16	5.56
110.23	6.898
130.12	8.2215

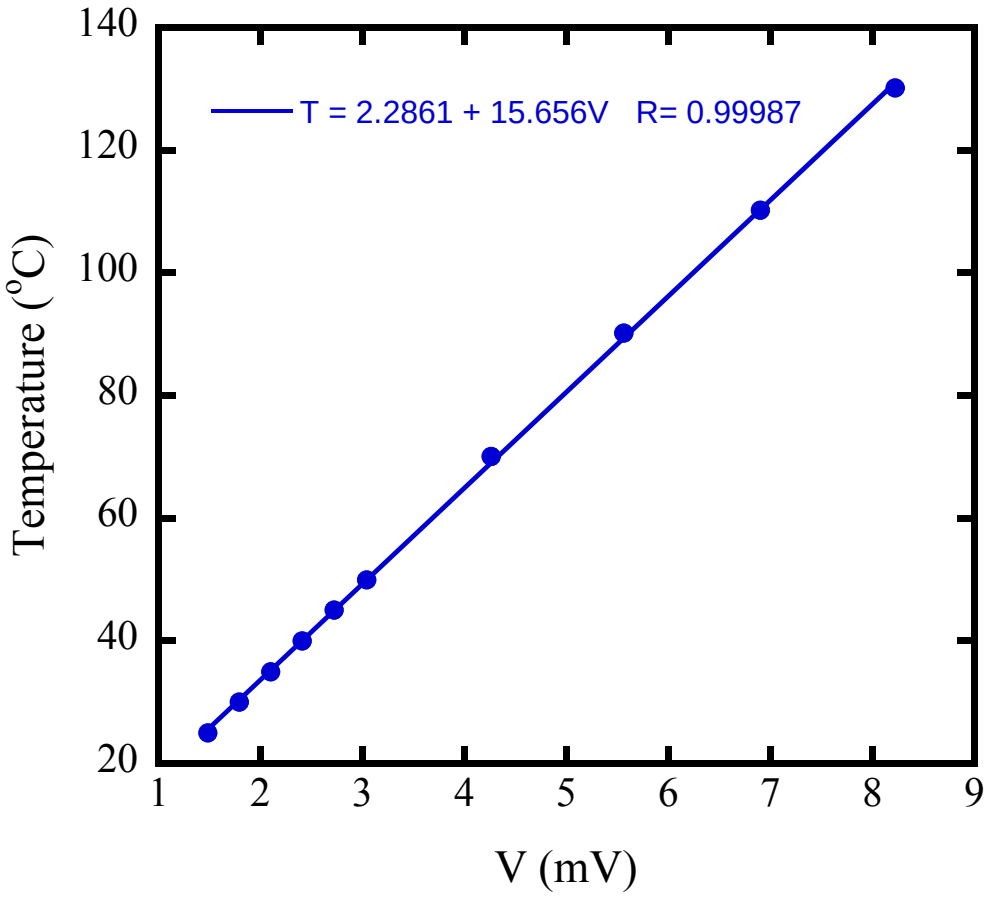

Figure A.1 Calibration of type E thermocouple

APPENDIX B

DATA ACQUISITION AND ANALYSIS PROGRAMS

B.1 LabVIEW Code

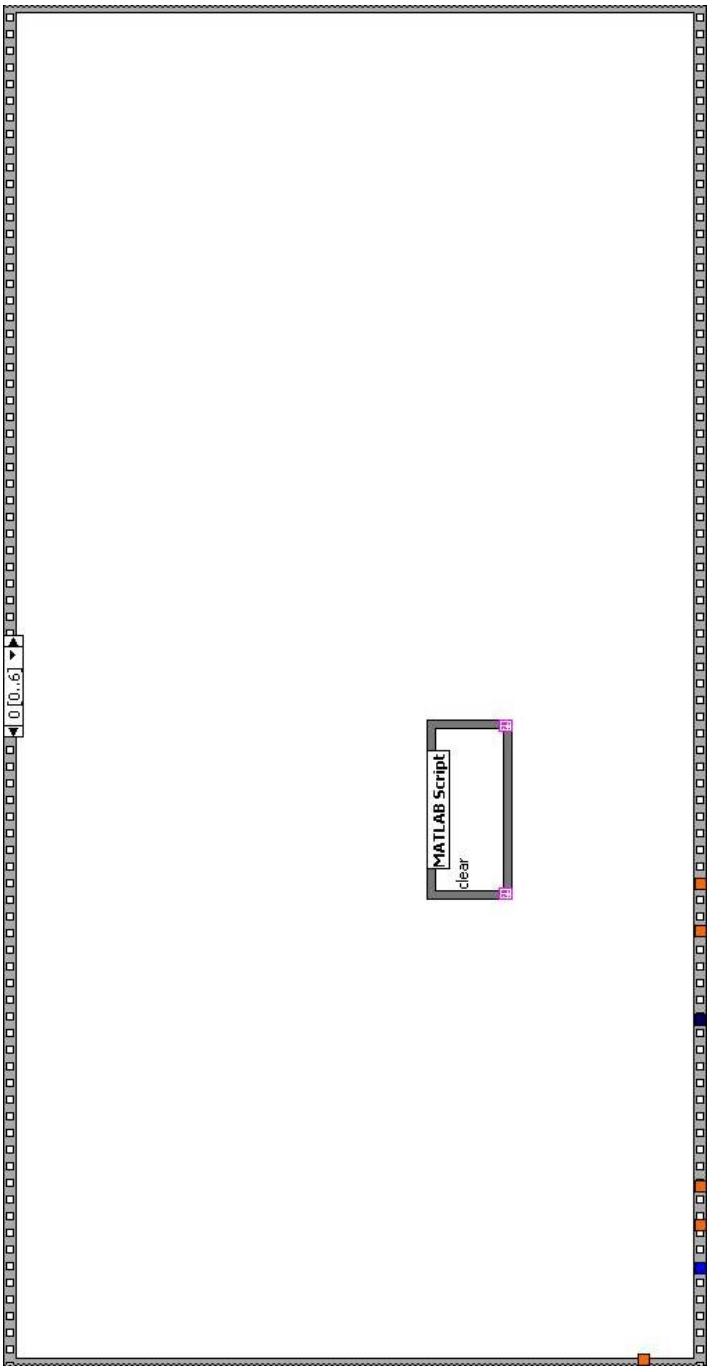

Figure B.1 LabVIEW Code: Case 0 of Nested Sequence Structure

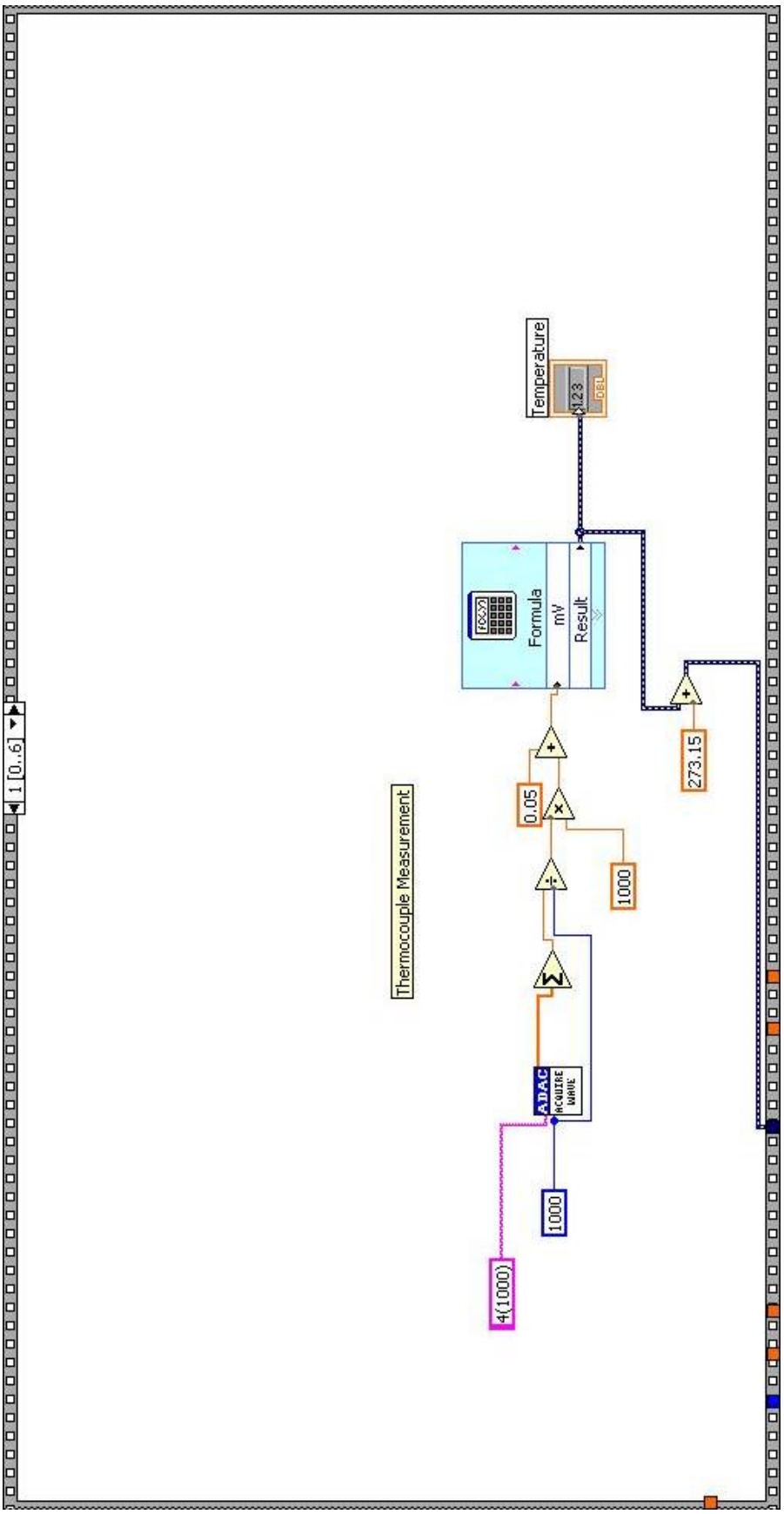

Figure B.2 LabVIEW Code: Case 1 of Nested Sequence Structure

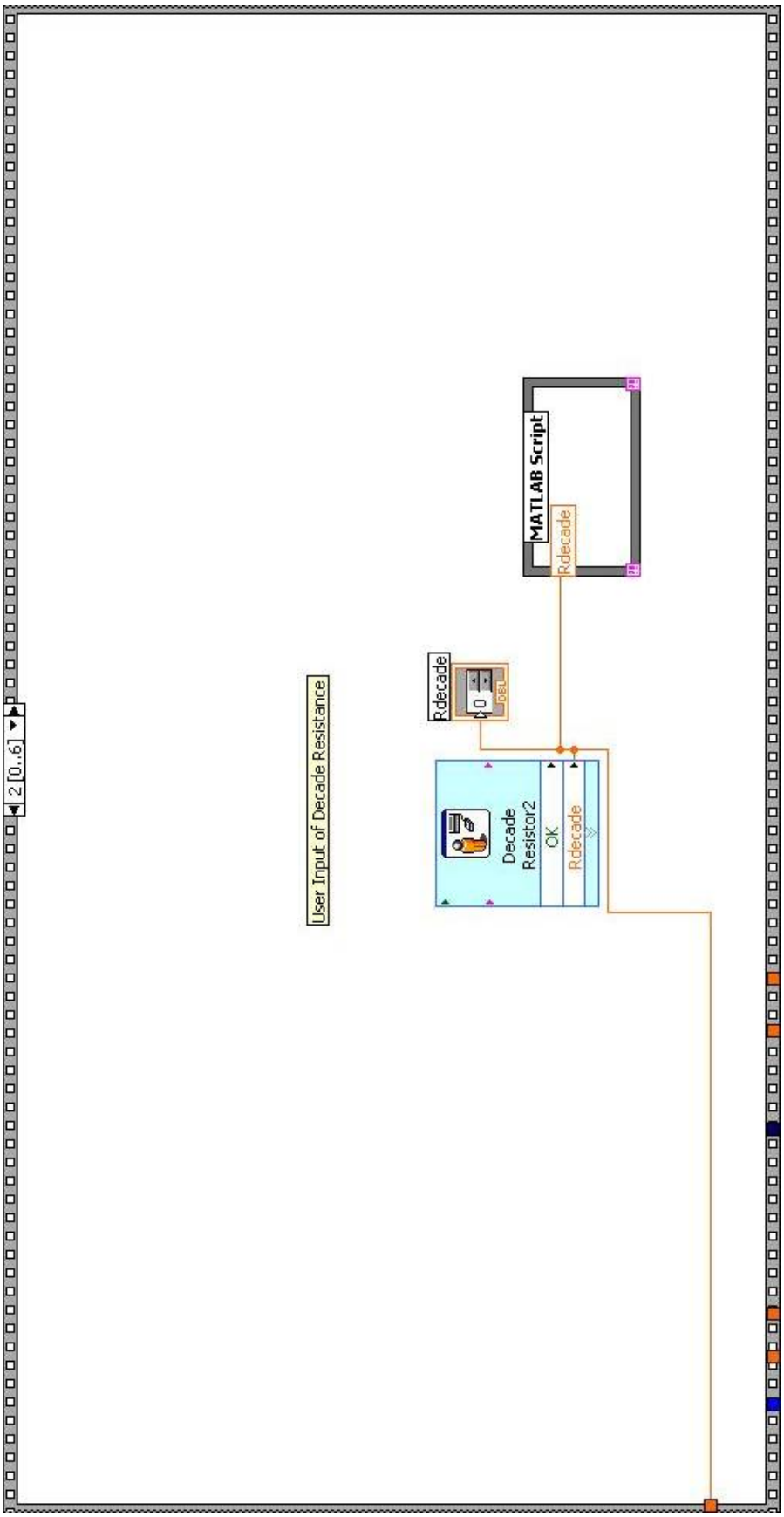

Figure B.3 LabVIEW Code: Case 2 of Nested Sequence Structure

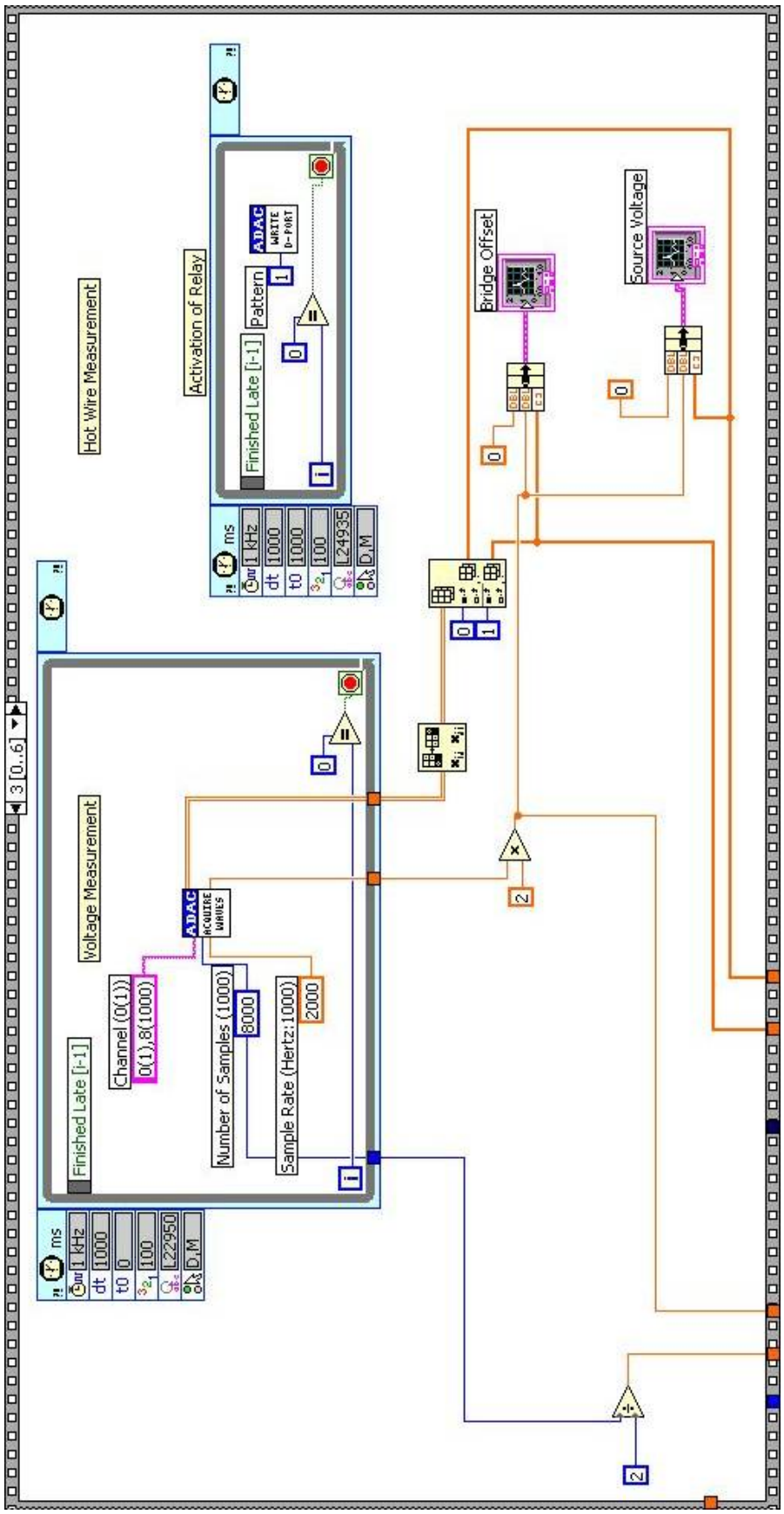

Figure B.4 LabVIEW Code: Case 3 of Nested Sequence Structure

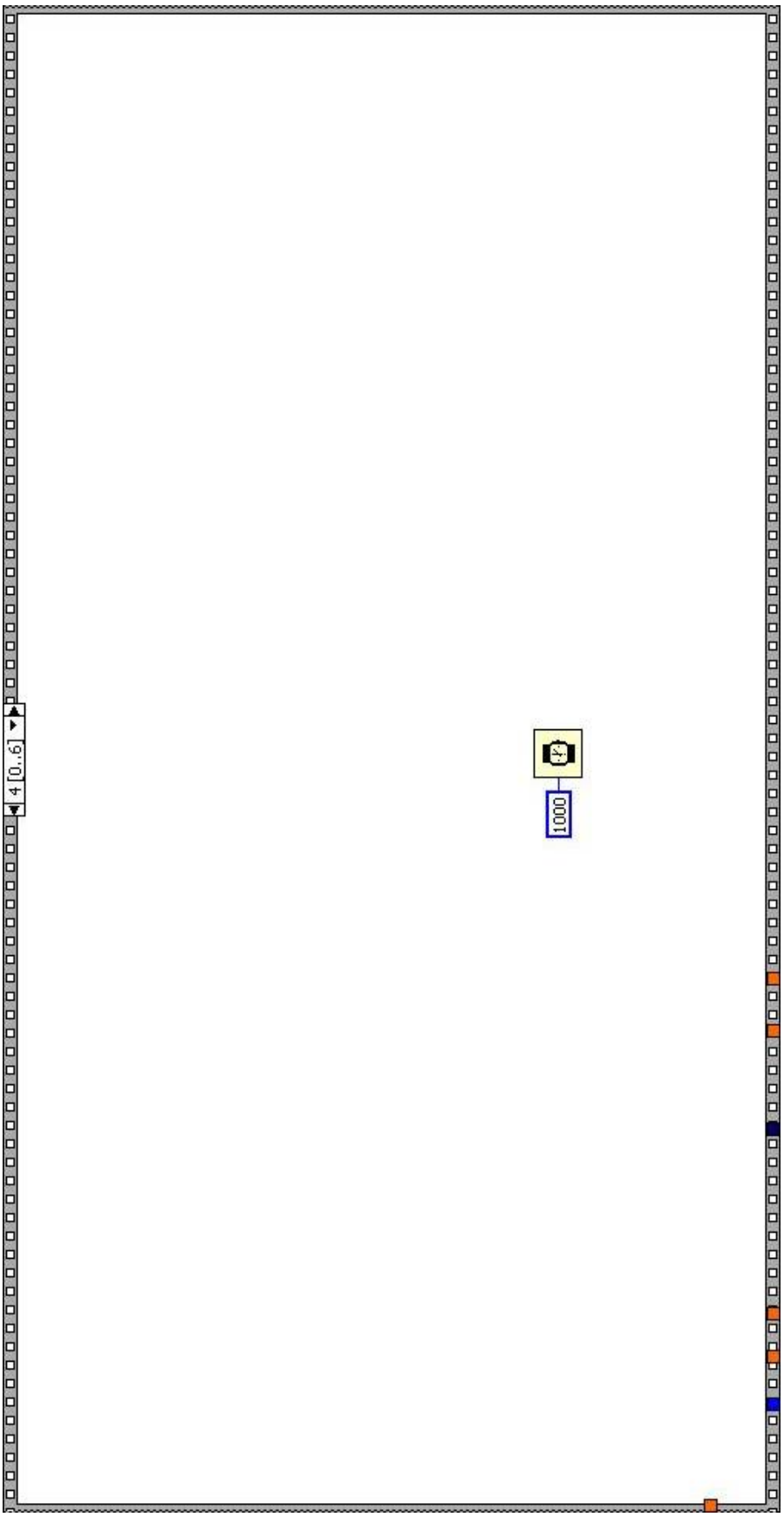

Figure B.5 LabVIEW Code: Case 4 of Nested Sequence Structure

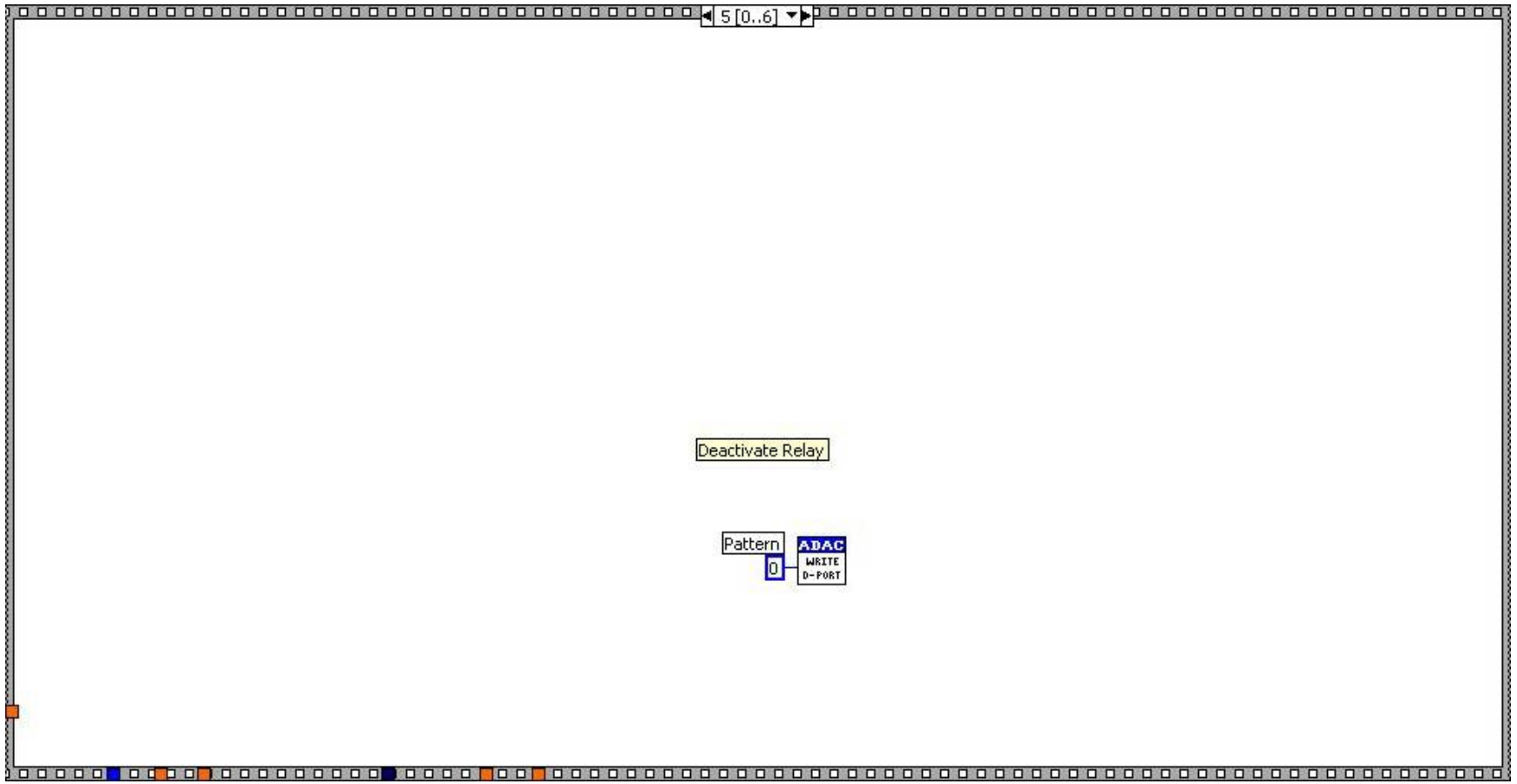

Figure B.6 LabVIEW Code: Case 5 of Nested Sequence Structure

Figure B.7 LabVIEW Code: Case 6 of Nested Sequence Structure

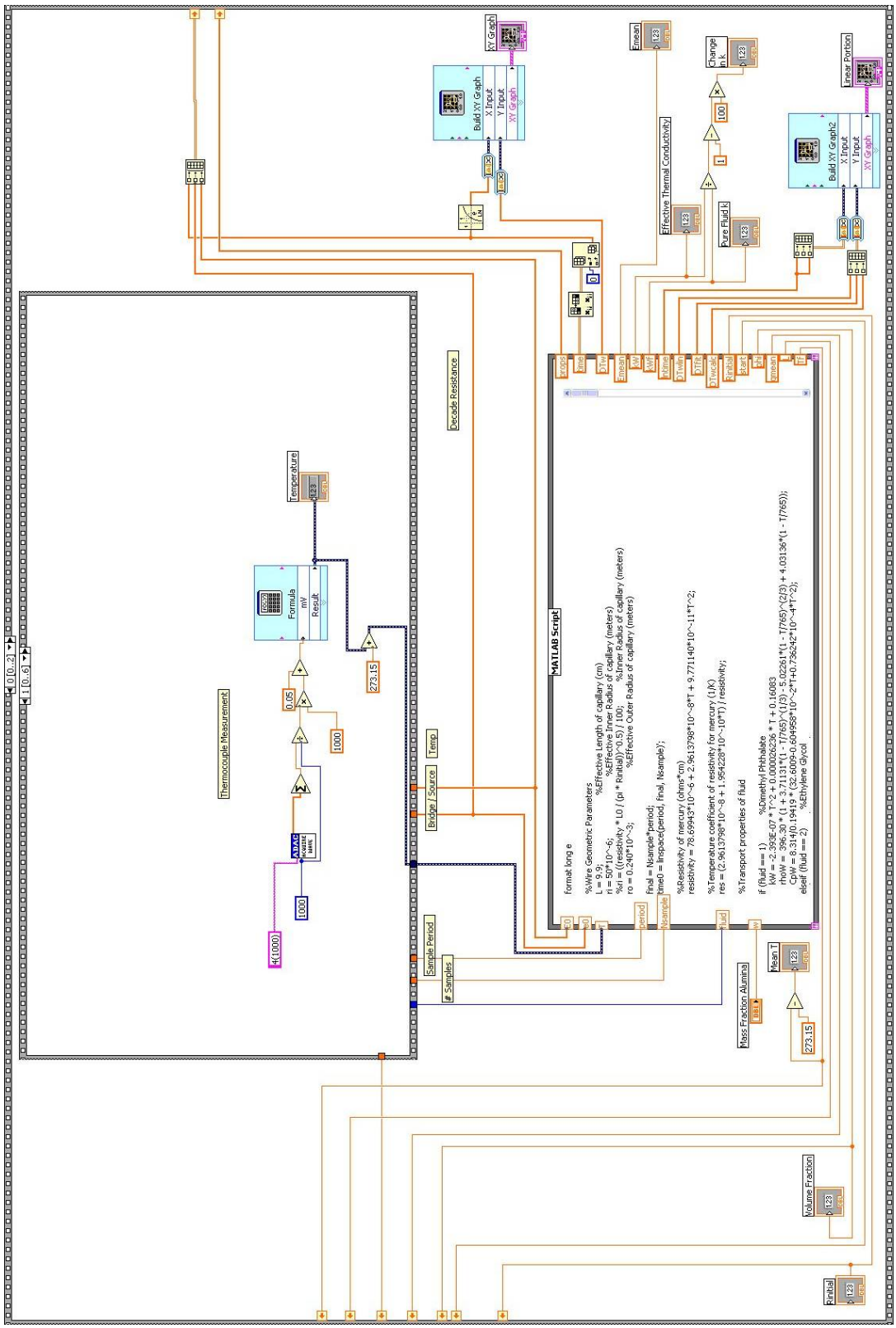

Figure B.8 LabVIEW Code: Case 0 of Sequence Structure

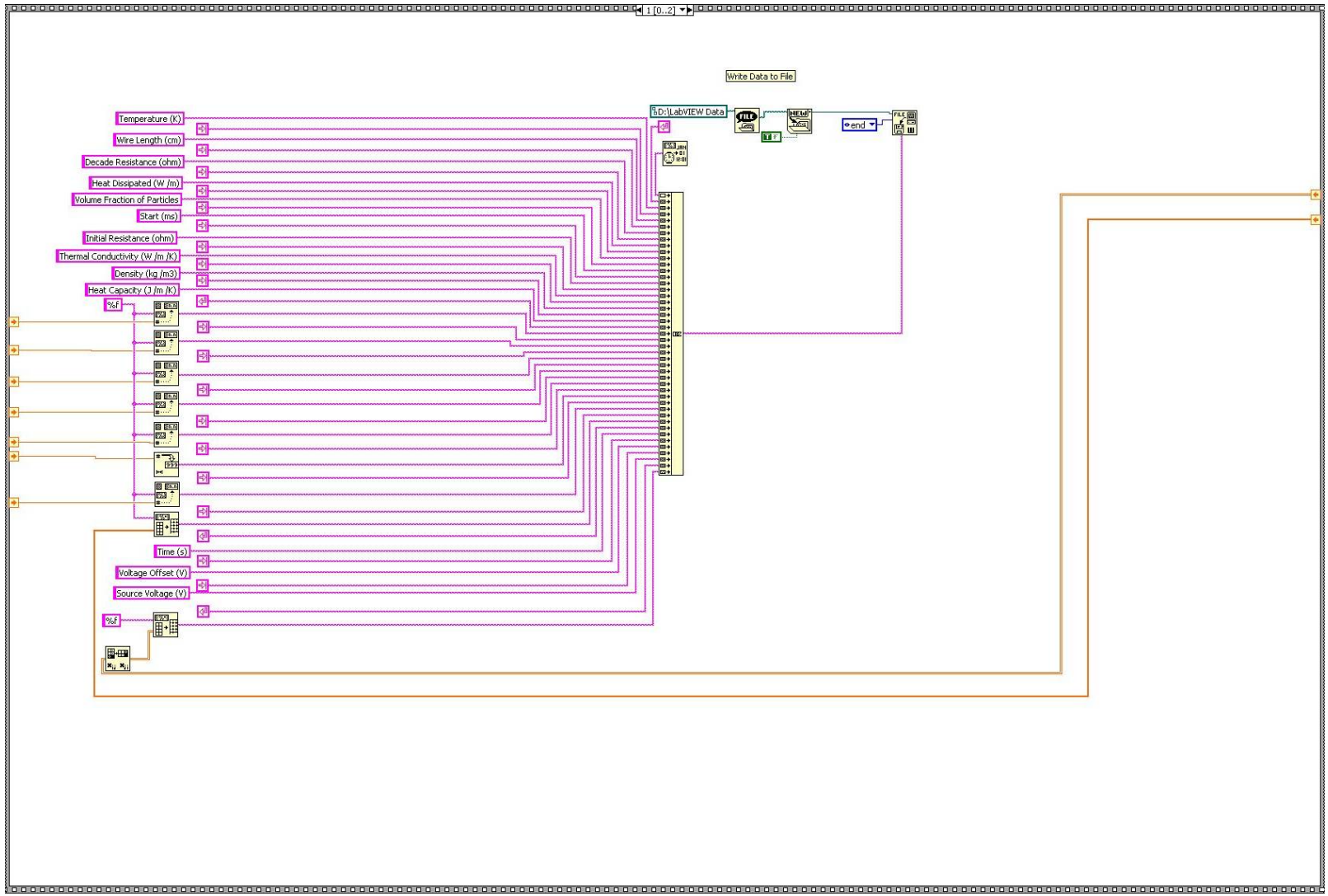

Figure B.9 LabVIEW Code: Case 1 of Sequence Structure

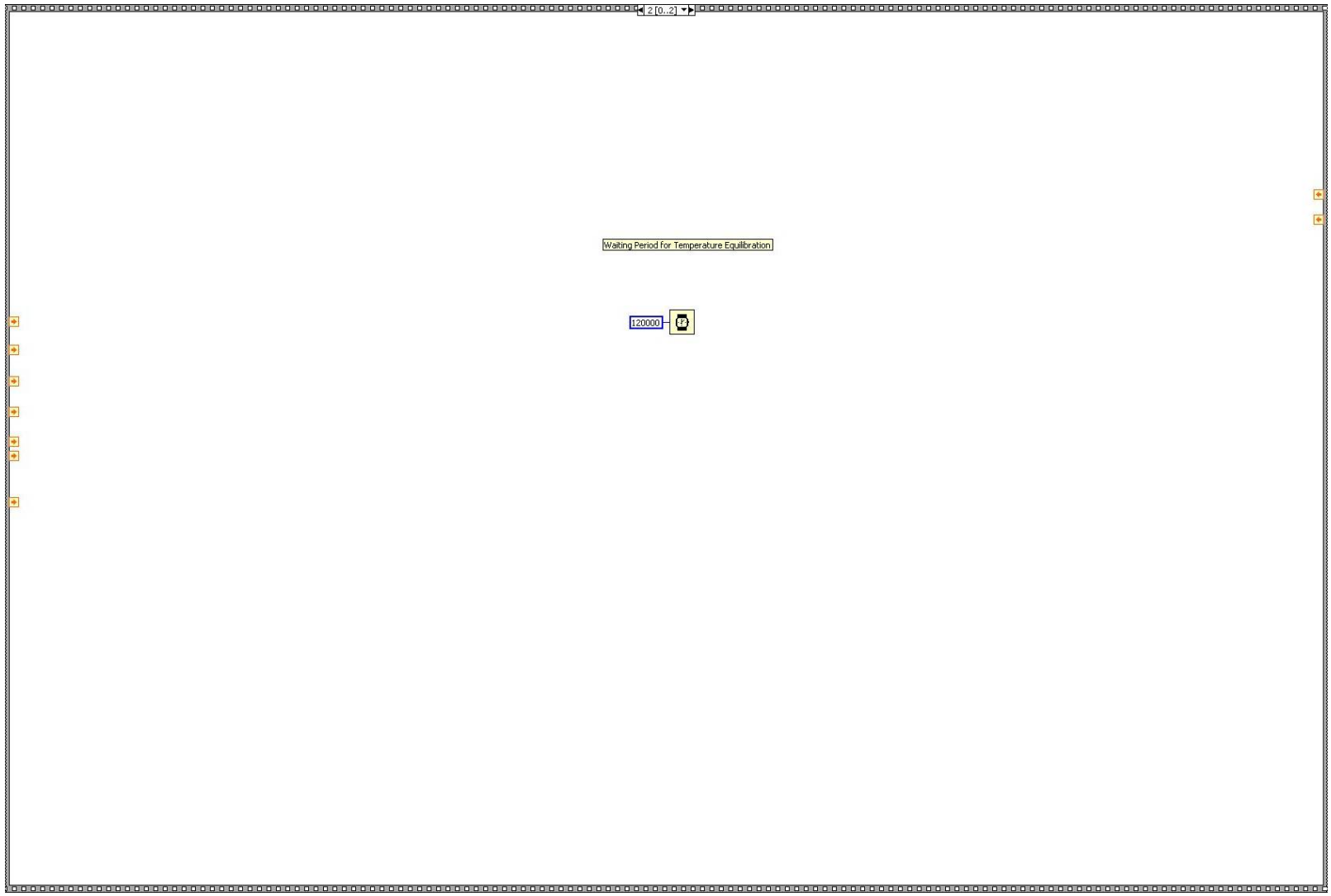

Figure B.10 LabVIEW Code: Case 2 of Nested Sequence Structure

B.2 MATLAB Code

```
format long e

%Wire Geometric Parameters
L = 9.9;                    %Effective Length of capillary (cm)
ri = 50*10^-6;              %Effective Inner Radius of capillary (meters)
ro = 0.240*10^-3;           %Effective Outer Radius of capillary (meters)

final = Nsample*period;
time0 = linspace(period, final, Nsample)';

%Resistivity of mercury (ohms*cm)
resistivity = 78.69943*10^-6 + 2.9613798*10^-8*T + 9.771140*10^-11*T^2;

%Temperature coefficient of resistivity for mercury (1/K)
res = (2.9613798*10^-8 + 1.954228*10^-10*T) / resistivity;

%Transport properties of fluid

if (fluid == 1)             %Dimethyl Phthalate
   kW = -2.393E-07 * T^2 + 0.000026236 * T + 0.16083
   rhoW =  396.30 * (1 + 3.71131*(1 - T/765)^(1/3) - 5.02261*(1 - T/765)^(2/3) +
4.03136*(1 - T/765));
   CpW = 8.314/0.19419 * (32.6009-0.604958*10^-2*T+0.736242*10^-4*T^2);
elseif (fluid == 2)                 %Ethylene Glycol
   kW = -4.8687E-07*T^2 + 3.7311E-04*T + 1.8625E-01
   rhoW = 62.068*(1.3151 / 0.25125^(1+ (1 - T/719.7)^0.2187));              %from Table
2-30 of Perry's 7th ed.
   CpW = 6.4884E-04*T^2 + 3.8644E+00*T + 1.0450E+03;
elseif (fluid == 3)                 %Toluene
   kW = 0.1311*(1.68182-0.682022*T/298.15)
   rhoW = 92.141*(0.8488 / 0.26655^(1+(1-T/591.8)^0.2878));                 %from Table
2-30 of Perry's 7th ed.
   CpW = 0.010606*T^2 - 3.5303*T + 1816.9;                  %from fit of data taken from
NIST Chemistry WebBook
elseif (fluid == 4)                 %Methanol
   kW = 9.790E-07*T^2 - 9.309E-04*T + 3.909E-01                    %from fit from Table
2-370 of Perry's 7th ed.
   rhoW = 32.042*(2.288 / 0.2685^(1+ (1 - T/512.64)^0.2453));     %from Table 2-30 of
Perry's 7th ed.
   CpW = (1.0580e5 - 3.6223e2*T+.93790*T^2)/32.042;               %from Table 2-196 of
Perry's 7th ed.
elseif (fluid == 5)                 %Hexane
   kW = -2.972E-04*T + 0.2143                       %from fit of data taken from NIST
Chemistry WebBook
```

```
   rhoW = 86.177 * 0.70824 / 0.26411^(1 + (1 - T/507.6)^0.27537);          %from Table
2-30 of Perry's 7th ed.
   CpW = (434.6*T + 63741) / 86.18;                    %from fit of data taken from NIST
Chemistry WebBook
elseif (fluid == 6)                %PDMS
   kW = 0.155           %from Manufacturer (3M)
   rhoW = 960;          %from Manufacturer (3M)
   CpW = 1460;          %from Manufacturer (3M)
else                               %Water
   kW = 1.8822E-08*T^3 - 2.7872E-05*T^2 + 1.3274E-02*T - 1.3710      % from fit of
data from IAPWS between 275 and 420 K
   rhoW = -0.0025803*T^2 + 1.2333*T + 857.81;              % from fit of data from
IAPWS between 275 and 420 K
   CpW = 0.013564*T^2 - 8.7637*T + 5594.7;                 % from fit of data from
IAPWS between 275 and 420 K
end

rhof = rhoW;

%Transport Properties of Mercury
CpHg = 152.039 - 0.0598907*T + 5.34676*10^-5*T^2;      %Heat Capacity for 273 K <
T < 473 K (CRC Handbook of Chemistry and Physics, 71st ed., 1990-1991, p. 6-102)
rhoHg = 14291 - 2.6325*T +3.0946*10^-4*T^2;      %Density for 273 K < T < 473 K
(CRC Handbook of Chemistry and Physics, 71st ed., 1990-1991, p. 15-18)
kHg = 1.1097794 + 3.064102*10^-2*T - 2.195573*10^-5*T^2;      %Thermal
Conductivity from Bleazard Thesis
alphaHg = kHg / (CpHg * rhoHg);              %Thermal Diffusivity at T

%Transport Properties of Pyrex Insulating Layer
CpIns = -0.001927*T^2 + 2.98*T + 14.72;   %Heat Capacity (J /kg /K) from
Thermophysical Properties of Matter, Vol. 5, 1970
rhoIns = 2230;           %Density (kg /m3) from Corning website (Pyrex brand 7740
Borosilicate type 1 glass)
kIns = 0.81039 + 1.0914*10^-3*T;             %Thermal Conductivity from Bleazard
Thesis
alphaIns = kIns / (CpIns * rhoIns);              %Thermal Diffusivity at T

%Transport Properties of Gamma - Alumina
CpAl = (108.683 + 37.2263*(T/1000) - 14.2065*(T/1000)^2 + 2.193601*(T/1000)^3 -
3.20988*(1000/T)^2) / 0.10196;                %Heat Capacity from NIST (J /kg /K)
rhoAl = 3700;           %from Manufacturer

%Transport Properties of Nanofluid
CpW = w*CpAl + (1-w)*CpW;
rhoW = 1/(w/rhoAl + (1-w)/rhoW);
```

```
eEuler = exp(0.577215665);              %exponent of Euler's constant

R1 = 100;                   %Resistance of fixed resistor 1 (ohms)
R2 = 100;                   %Resistance of fixed resistor 2 (ohms)
X = R2 / (R1 + R2);
Y = length(find(E0 > 0.05));
Z = Nsample + 1 - Y;

e = e0(Z:Nsample);
E = E0(Z:Nsample);
Eavg = mean(E(2:Y));
time = time0(1:Y);
Rwire = (Rdecade)*(e + Eavg*X) ./ (Eavg - Eavg*X - e);              %Resistance of
capillary (ohms)
aa = polyfit(time(2:4)', Rwire(2:4), 1);
Rinitial = aa(2);                   %Initial Wire Resistance
DTw = (Rwire - Rinitial) ./ (res*Rinitial);              %Temperature change of wire (K)

T1 = T + DTw;
resistivity1 =  78.69943*10^-6 + 2.9613798*10^-8*T1 + 9.771140*10^-11*T1.^2;
res1 =  (2.9613798*10^-8 + 1.954228*10^-10*T1) ./ resistivity1;
DTw = (Rwire - Rinitial) ./ (res1*Rinitial);

start =880;
stop = start + 1500;

Emean = mean(E(start:stop));
Rmean = mean(Rwire(start:stop));

timelin = time(start:stop)';
lntime = log(timelin); %Linear part of curve
DTwlin = DTw(start:stop);
fit0 = polyfit(lntime, DTwlin, 1);       %Linear fit of Temp vs ln Time
slope = fit0(1);
DTfit = slope * lntime + fit0(2);

qmean = Emean^2*Rmean / ( L * (Rdecade + Rmean)^2)*100;              %Power
dissipated (W /m)
kW = qmean / (4 * pi * slope)
kW0 = kW;

gv = [2.40482, 5.52008, 8.65373, 11.79153, 14.93092, 18.07106, 21.21164, 24.35247,
27.49348, 30.63461]';
index = linspace(11, 100, 90)';
CN = index * pi - pi/4;
```

```
gv(11:100) = CN + 1 ./ (8*CN) - 31 ./ (394*CN.^3) + 3779 ./ (15360*CN.^5);      % roots of the zero-order Bessel function of the first kind
Yo = bessely(0,gv);              %zero-order Bessel function of the second kind
b = 0.0219;
gv2 = gv.^2;
[dim2, dim] = size(timelin);

p = 1;
count = 0;

while p > 0.01

   count = count +1;

   alphaW = kW / (CpW * rhoW);              %Thermal Diffusivity at T

   %Finite physical properties of the wire and correction for insulating layer
   C1 = ri^2 / 8 * ((kW - kIns) / kHg * (1/alphaHg - 1/alphaIns) + 4 / alphaIns - 2 / alphaHg);
   C2 = ro^2 / 2 * (1/alphaW - 1/alphaIns) + ri^2 / kIns * (kIns / alphaIns - kHg / alphaHg) * log(ro / ri);
   C3 = ri^2 / (2 * kW) * (kIns / alphaIns - kHg / alphaHg) + ro^2 / (2 * kW) * (kW / alphaW - kIns / alphaIns);

   dT1 =  -qmean / (4 * pi * kW) * (2 * log(ri / ro) + 2 * kW / kIns * log(ro / ri) + kW / (2 *  kHg) + ( C1 + C2 + C3 * log(4 * alphaW * timelin / (ro^2 * eEuler))) ./timelin);

   AA = exp((-alphaW/b^2)*gv2*timelin);
   BB = (pi*Yo*ones(1,dim)).^2;
   dT2 = qmean / (4 * pi *kW) * (log (4 * alphaW * timelin / (b^2 * eEuler)) + sum (AA .* BB));

   DTw12 = DTwlin + dT1 + dT2;
   fit2 =  polyfit(lntime, DTw12, 1);   %Linear fit of Corrected Temp vs ln Time
   M2 = fit2(1);
   B2 = fit2(2);
   ebm = exp(B2 / M2);
   B = fminsearch(@(B) LLSQ(B, DTw12, timelin, M2, ebm, eEuler), -0.1);
   dT3 = - M2 * B * (log (ebm * timelin) / (ebm * eEuler) + 1 / (ebm * eEuler) - timelin);

   DTid = DTw12 + dT3;
   fitf = polyfit(lntime, DTid, 1);
   Mf = fitf(1);
   bf = fitf(2);
   kWnew = qmean / (4 * pi * Mf);
```

```
   p = abs(kWnew - kW)/kW*100;
   kW = kWnew

end

alphaW = kW / (CpW * rhoW);        %Thermal Diffusivity at T

DTw1 = DTwlin + dT1;
fit1 = polyfit(lntime, DTw1, 1);
M1 = fit1(1);
kW1 = qmean / (4 * pi * M1);
error1 = (kW1 - kW0) / kW1 * 100;

kW2 = qmean / (4 * pi * M2);
error2 = (kW2 - kW1) / kW2 * 100;

error3 = (kW - kW2) / kW * 100;

phi = w*rhof/(w*rhof+(1-w)*rhoAl)*100

P1 = ri^2/4 * (1/alphaIns - 1/(2*alphaHg)) + ro^2/4 * (2 / alphaW - 1 / alphaIns);
P2 = ri^2/(2*kIns) * (kIns / alphaIns - kHg / alphaHg) * log(ro/ri);
dTf = qmean / (4*pi*kW) * (log(4*alphaW*timelin/(ro^2*eEuler)) + (P1 + P2 + C3 *
log(4*alphaW*timelin/(ro^2*eEuler))) ./timelin);
Tf = T + mean(dTf);

if (fluid == 1)            %Dimethyl Phthalate
   kWf = -2.393E-07 * Tf^2 + 0.000026236 * Tf + 0.16083;
elseif (fluid == 2)        %Ethylene Glycol
   kWf = -4.8687E-07*Tf^2 + 3.7311E-04*Tf + 1.8625E-01;
elseif (fluid == 3)        %Toluene
   kWf = 0.1311*(1.68182-0.682022*Tf/298.15);
elseif (fluid == 4)        %Methanol
   kWf = 9.790E-07*Tf^2 - 9.309E-04*Tf + 3.909E-01;                %from fit from
Table 2-370 of Perry's 7th ed.
elseif (fluid == 5)        %Hexane
   kWf = -2.972E-04*Tf + 0.2143;                                   %from fit of data taken from
NIST Chemistry WebBook
elseif (fluid == 6)        %PDMS
   kWf = 0.155;
else                       %Water
   kWf = 1.8822E-08*Tf^3 - 2.7872E-05*Tf^2 + 1.3274E-02*Tf - 1.3710    % from fit of
data from IAPWS between 275 and 420 K
end

props = [kW rhoW CpW];
```

```
DTwcalc = qmean / (4 * pi * kW) * (log (4 * alphaW * timelin / (ro^2 * eEuler)) + 2 *
kW / kIns * log (ro / ri) + kW / (2 * kHg) +  ( C1 + C2 + C3 * log(4 * alphaW * timelin /
(ro^2 * eEuler))) ./timelin);
```

APPENDIX C

IMAGING OF NANOPARTICLES

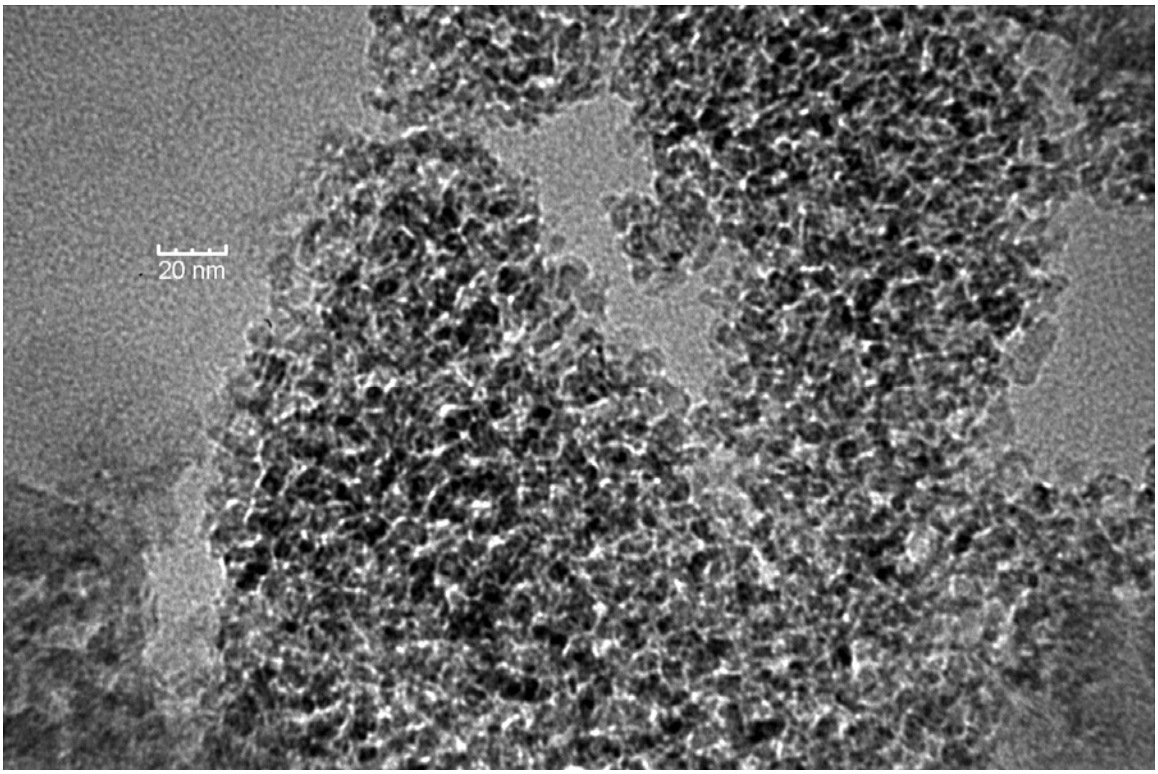

Figure C.1 Transmission electron microscopy image of alumina particles with a nominal size of 11 nm from Nanostructure and Amorphous Materials. The average diameter of these particles is 6 nm and 8 nm as determined by TEM and BET, respectively. Magnification = 200,000

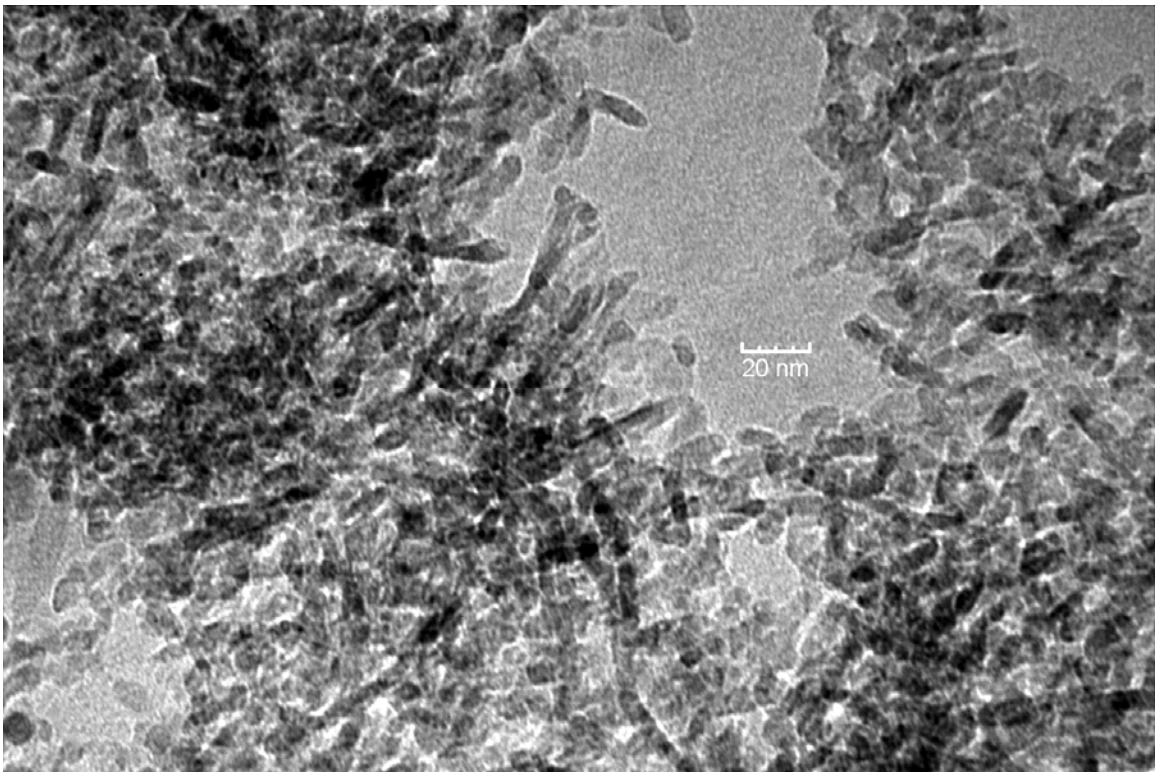

Figure C.2 Transmission electron microscopy image of alumina particles with a nominal size of 20 nm from Nanostructure and Amorphous Materials. The average diameter of these particles is 10 nm and 12 nm as determined by TEM and BET, respectively. Magnification = 200,000

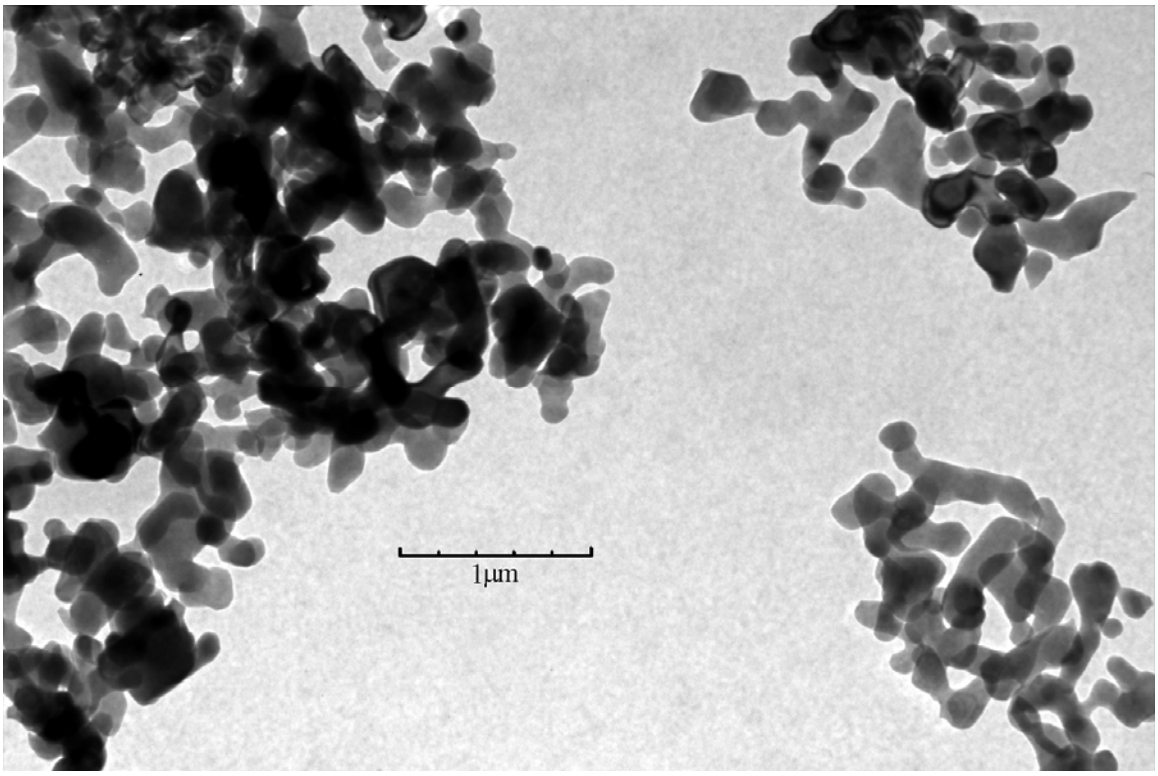

Figure C.3 Transmission electron microscopy image of alumina particles with a nominal size of 150 nm from Nanostructure and Amorphous Materials. The average diameter of these particles is 180 nm and 245 nm as determined by TEM and BET, respectively Magnification = 10,000

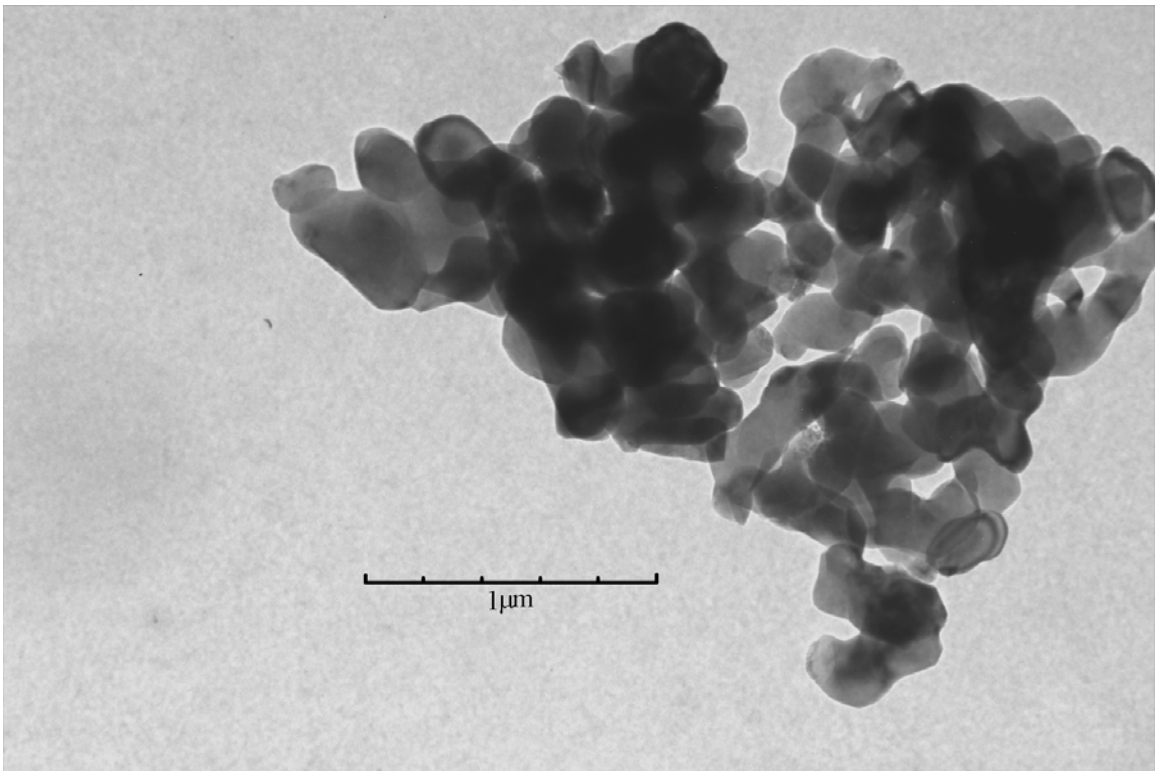

Figure C.4 Transmission electron microscopy image of alumina particles with a nominal size of 1000 nm from Electron Microscopy Sciences. The average diameter of these particles is 290 nm and 282 nm as determined by TEM and BET, respectively. Magnification = 15,000

REFERENCES

1. Bird, R.B., W.E. Stewart, and E.N. Lightfoot, *Transport Phenomena*. 2nd ed. 2002, New York: John Wiley & Sons, Inc. 895.

2. Perry, R.H. and D.W. Green, eds. *Perry's Chemical Engineers' Handbook*. 7th ed. 1997, McGraw-Hill, Inc.: New York.

3. Choi, S.U.S., *Enhancing thermal conductivity of fluids with nanoparticles.* FED, 1995. **231**(Developments and Applications of Non-Newtonian Flows): p. 99-105.

4. Xuan, Y.M. and Q. Li, *Investigation on convective heat transfer and flow features of nanofluids.* Journal of Heat Transfer-Transactions of the Asme, 2003. **125**(1): p. 151-155.

5. Wen, D.S. and Y.L. Ding, *Experimental investigation into the pool boiling heat transfer of aqueous based gamma-alumina nanofluids.* Journal of Nanoparticle Research, 2005. **7**(2): p. 265-274.

6. Wang, X.Q. and A.S. Mujumdar, *Heat transfer characteristics of nanofluids: a review.* International Journal of Thermal Sciences, 2007. **46**(1): p. 1-19.

7. Choi, S.U.S., Z.G. Zhang, W. Yu, F.E. Lockwood, and E.A. Grulke, *Anomalous thermal conductivity enhancement in nanotube suspensions.* Applied Physics Letters, 2001. **79**(14): p. 2252-2254.

8. Das, S.K., N. Putra, P. Thiesen, and W. Roetzel, *Temperature dependence of thermal conductivity enhancement for nanofluids.* Journal of Heat Transfer-Transactions of the Asme, 2003. **125**(4): p. 567-574.

9. Li, C.H. and G.P. Peterson, *Experimental investigation of temperature and volume fraction variations on the effective thermal conductivity of nanoparticle suspensions (nanofluids).* Journal of Applied Physics, 2006. **99**(8).

10. Yang, B. and Z.H. Han, *Temperature-dependent thermal conductivity of nanorod-based nanofluids.* Applied Physics Letters, 2006. **89**(8).

11. Zhang, X., H. Gu, and M. Fujii, *Effective thermal conductivity and thermal diffusivity of nanofluids containing spherical and cylindrical nanoparticles.* Experimental Thermal and Fluid Science, 2007. **31**(6): p. 593-599.

12. Xie, H.Q., J.C. Wang, T.G. Xi, Y. Liu, F. Ai, and Q.R. Wu, *Thermal conductivity enhancement of suspensions containing nanosized alumina particles.* Journal of Applied Physics, 2002. **91**(7): p. 4568-4572.

13. Kim, S.H., S.R. Choi, and D. Kim, *Thermal conductivity of metal-oxide nanofluids: Particle size dependence and effect of laser irradiation.* Journal of Heat Transfer-Transactions of the ASME, 2007. **129**(3): p. 298-307.

14. Keblinski, P., S.R. Phillpot, S.U.S. Choi, and J.A. Eastman, *Mechanisms of heat flow in suspensions of nano-sized particles (nanofluids).* International Journal of Heat and Mass Transfer, 2002. **45**(4): p. 855-863.

15. Tsederberg, N.V., *Thermal Conductivity of Gases and Liquids*. 1965, Cambridge, Massachusetts: THE M.I.T. Press. 246.

16. Poling, B.E., J.M. Prausnitz, and J.P. O'Connell, *The Properties of Gases and Liquids*. 5th ed. 2001, Boston: The McGraw-Hill Companies.

17. Dean, J.A., *Lange's Handbook of Chemistry*. 14th ed. 1992, New York: McGraw-Hill, Inc.

18. Hwang, Y., J.K. Lee, C.H. Lee, Y.M. Jung, S.I. Cheong, C.G. Lee, B.C. Ku, and S.P. Jang, *Stability and thermal conductivity characteristics of nanofluids.* Thermochimica Acta, 2007. **455**(1-2): p. 70-74.

19. Shackelford, J.F. and W. Alexander, eds. *CRC Materials Science and Engineering Handbook*. 3rd ed. 2001, CRC Press: Boca Raton, FL. 1949.

20. Yu, C.H., S. Saha, J.H. Zhou, L. Shi, A.M. Cassell, B.A. Cruden, Q. Ngo, and J. Li, *Thermal contact resistance and thermal conductivity of a carbon nanofiber.* Journal of Heat Transfer-Transactions of the Asme, 2006. **128**(3): p. 234-239.

21. Slack, G.A., *THERMAL CONDUCTIVITY OF MGO, AL2O3, MGAL2O4, AND FE3O4 CRYSTALS FROM 3 DEGREES TO 300 DEGREES K.* Physical Review, 1962. **126**(2): p. 427-&.

22. Zhitinskaya, M.K., S.A. Nemov, T.E. Svechnikova, L.N. Luk'yanova, P.P. Konstantinov, and V.A. Kutasov, *Thermal conductivity of Bi2Te3 : Sn and the effect of codoping by Pb and I atoms.* Physics of the Solid State, 2003. **45**(7): p. 1251-1253.

23. Meyer, C.A., ed. *ASME Steam Tables: Thermodynamic and Transport Properties of Steam*. 6th ed. 1993, American Society of Mechanical Engineers: New York. 436.

24. Xie, H.Q., H. Lee, W. Youn, and M. Choi, *Nanofluids containing multiwalled carbon nanotubes and their enhanced thermal conductivities.* Journal of Applied Physics, 2003. **94**(8): p. 4967-4971.

25. Li, Q. and Y.M. Xuan, *Enhanced heat transfer behaviors of new heat carrier for spacecraft thermal management.* Journal of Spacecraft and Rockets, 2006. **43**(3): p. 687-690.

26. *NIST Reference Fluid Thermodynamic and Transport Properties Database version 7*. 2005.

27. Shaikh, S., K. Lafdi, and R. Ponnappan, *Thermal conductivity improvement in carbon nanoparticle doped PAO oil: An experimental study.* Journal of Applied Physics, 2007. **101**(6): p. 7.

28. McLaughlin, E., *THERMAL CONDUCTIVITY OF LIQUIDS + DENSE GASES.* Chemical Reviews, 1964. **64**(4): p. 389-428.

29. Diguilio, R. and A.S. Teja, *THERMAL-CONDUCTIVITY OF POLY(ETHYLENE GLYCOLS) AND THEIR BINARY-MIXTURES.* Journal of Chemical and Engineering Data, 1990. **35**(2): p. 117-121.

30. Doye, J.P.K. and D.J. Wales, *Polytetrahedral Clusters.* Physical Review Letters, 2001. **86**(25): p. 5719 - 5722.

31. Kutz, M., ed. *Handbook of Materials Selection*. 2002, John Wiley and Sons: New York. 1497.

32. Kang, H.U., S.H. Kim, and J.M. Oh, *Estimation of thermal conductivity of nanofluid using experimental effective particle volume.* Experimental Heat Transfer, 2006. **19**(3): p. 181-191.

33. Tritt, T., ed. *Thermal conductivity: theory, properties, and applications*. 2004, Kluwer Academic/Plenum Publishers: New York. 290.

34. Tien, C.-L., A. Majumdar, and F.M. Gerner, eds. *Microscale Energy Transport*. 1998, Taylor & Francis: Washington D.C. 395.

35. Tien, C.-L., ed. *Annual Review of Heat Transfer*. Vol. 7. 1996, Begell House, Inc: New York. 444.

36. Marquardt, F. *Sound wave traveling through crystal lattice*. 2007 [cited 2008]; Available from: http://en.wikipedia.org/wiki/Image:Lattice_wave.svg.

37. Bansal, N.P. and D. Zhu, *Thermal Conductivity of Alumina-Toughened Ziconia Composites*. 2003, NASA: Cleveland. p. 15.

38. Ju, Y.S., *Phonon heat transport in silicon nanostructures.* Applied Physics Letters, 2005. **87**(15): p. 3.

39. Behkam, B., Y.Z. Yang, and M. Asheghi, *Thermal property measurement of thin aluminum oxide layers for giant magnetoresistive (GMR) head applications.* International Journal of Heat and Mass Transfer, 2005. **48**(10): p. 2023-2031.

40. Liu, W. and M. Asheghi, *Phonon-boundary scattering in ultrathin single-crystal silicon layers.* Applied Physics Letters, 2004. **84**(19): p. 3819-3821.

41. Yu, X.Y., G. Chen, A. Verma, and J.S. Smith, *TEMPERATURE-DEPENDENCE OF THERMOPHYSICAL PROPERTIES OF GAAS/ALAS PERIODIC STRUCTURE.* Applied Physics Letters, 1995. **67**(24): p. 3554-3556.

42. Cahill, D.G., W.K. Ford, K.E. Goodson, G.D. Mahan, A. Majumdar, H.J. Maris, R. Merlin, and S.R. Phillpot, *Nanoscale thermal transport.* Journal of Applied Physics, 2003. **93**(2): p. 793-818.

43. Ziambaras, E. and P. Hyldgaard, *Phonon Knudsen flow in nanostructured semiconductor systems.* Journal of Applied Physics, 2006. **99**(5): p. 054303.

44. Li, D.Y., Y.Y. Wu, P. Kim, L. Shi, P.D. Yang, and A. Majumdar, *Thermal conductivity of individual silicon nanowires.* Applied Physics Letters, 2003. **83**(14): p. 2934-2936.

45. Fang, K.C., C.I. Weng, and S.P. Ju, *An investigation into the structural features and thermal conductivity of silicon nanoparticles using molecular dynamics simulations.* Nanotechnology, 2006. **17**(15): p. 3909-3914.

46. Shin, S. and S.H. Lee, *Thermal conductivity of suspensions in shear flow fields.* International Journal of Heat and Mass Transfer, 2000. **43**(23): p. 4275-4284.

47. Bjorneklett, A., L. Halbo, and H. Kristiansen, *THERMAL-CONDUCTIVITY OF EPOXY ADHESIVES FILLED WITH SILVER PARTICLES.* International Journal of Adhesion and Adhesives, 1992. **12**(2): p. 99-104.

48. Turian, R.M., D.J. Sung, and F.L. Hsu, *Thermal conductivity of granular coals, coal-water mixtures and multi-solid/liquid suspensions.* Fuel, 1991. **70**(10): p. 1157-1172.

49. Eastman, J.A., U.S. Choi, S. Li, L.J. Thompson, and S. Lee, *Enhanced thermal conductivity through the development of nanofluids.* Materials Research Society Symposium Proceedings, 1997. **457**(Nanophase and Nanocomposite Materials II): p. 3-11.

50. Chon, C.H., K.D. Kihm, S.P. Lee, and S.U.S. Choi, *Empirical correlation finding the role of temperature and particle size for nanofluid (Al2O3) thermal conductivity enhancement.* Applied Physics Letters, 2005. **87**(15).

51. Zhang, X., H. Gu, and M. Fujii, *Experimental study on the effective thermal conductivity and thermal diffusivity of nanofluids.* International Journal of Thermophysics, 2006. **27**(2): p. 569-580.

52. Li, C.H. and G.P. Peterson, *The effect of particle size on the effective thermal conductivity of Al2O3-water nanofluids.* Journal of Applied Physics, 2007. **101**(4): p. 044312.

53. Wang, X.W., X.F. Xu, and S.U.S. Choi, *Thermal conductivity of nanoparticle-fluid mixture.* Journal of Thermophysics and Heat Transfer, 1999. **13**(4): p. 474-480.

54. Zhang, X., H. Gu, and M. Fujii, *Effective thermal conductivity and thermal diffusivity of nanofluids containing spherical and cylindrical nanoparticles.* Journal of Applied Physics, 2006. **100**(4): p. 044325.

55. Yoo, D.H., K.S. Hong, T.E. Hong, J.A. Eastman, and H.S. Yang, *Thermal conductivity of Al2O3/water nanofluids.* Journal of the Korean Physical Society, 2007. **51**: p. S84-S87.

56. Yoo, D.H., K.S. Hong, and H.S. Yang, *Study of thermal conductivity of nanofluids for the application of heat transfer fluids.* Thermochimica Acta, 2007. **455**(1-2): p. 66-69.

57. Lee, S., S.U.S. Choi, S. Li, and J.A. Eastman, *Measuring thermal conductivity of fluids containing oxide nanoparticles.* Journal of Heat Transfer-Transactions of the Asme, 1999. **121**(2): p. 280-289.

58. Timofeeva, E.V., A.N. Gavrilov, J.M. McCloskey, Y.V. Tolmachev, S. Sprunt, L.M. Lopatina, and J.V. Selinger, *Thermal conductivity and particle agglomeration in alumina nanofluids: Experiment and theory.* Physical Review E, 2007. **76**(6): p. 16.

59. Xie, H.Q., J.C. Wang, T.G. Xi, Y. Liu, and F. Ai, *Dependence of the thermal conductivity of nanoparticle-fluid mixture on the base fluid.* Journal of Materials Science Letters, 2002. **21**(19): p. 1469-1471.

60. Eastman, J.A., U.S. Choi, G. Soyez, L.J. Thompson, and R.J. DiMelfi, *Novel thermal properties of nanostructured materials.* Materials Science Forum, 1999. **312-314**(Metastable, Mechanically Alloyed and Nanocrystalline Materials): p. 629-634.

61. Venerus, D.C., M.S. Kabadi, S. Lee, and V. Perez-Luna, *Study of thermal transport in nanoparticle suspensions using forced Rayleigh scattering.* Journal of Applied Physics, 2006. **100**(9).

62. Hwang, Y.J., Y.C. Ahn, H.S. Shin, C.G. Lee, G.T. Kim, H.S. Park, and J.K. Lee, *Investigation on characteristics of thermal conductivity enhancement of nanofluids.* Current Applied Physics, 2006. **6**(6): p. 1068-1071.

63. Lee, D., J.W. Kim, and B.G. Kim, *A new parameter to control heat transport in nanofluids: Surface charge state of the particle in suspension.* Journal of Physical Chemistry B, 2006. **110**(9): p. 4323-4328.

64. Kwak, K. and C. Kim, *Viscosity and thermal conductivity of copper oxide nanofluid dispersed in ethylene glycol.* Korea-Australia Rheology Journal, 2005. **17**(2): p. 35-40.

65. Liu, M.S., M.C.C. Lin, I.T. Huang, and C.C. Wang, *Enhancement of thermal conductivity with CuO for nanofluids.* Chemical Engineering & Technology, 2006. **29**(1): p. 72-77.

66. Murshed, S.M.S., K.C. Leong, and C. Yang, *Enhanced thermal conductivity of TiO2 - water based nanofluids.* International Journal of Thermal Sciences, 2005. **44**(4): p. 367-373.

67. Wang, Z.L., D.W. Tang, S. Liu, X.H. Zheng, and N. Araki, *Thermal-conductivity and thermal-diffusivity measurements of nanofluids by 3 omega method and mechanism analysis of heat transport.* International Journal of Thermophysics, 2007. **28**(4): p. 1255-1268.

68. Hong, T.K. and H.S. Yang, *Nanoparticle-dispersion-dependent thermal conductivity in nanofluids.* Journal of the Korean Physical Society, 2005. **47**: p. S321-S324.

69. Zhu, H.T., C.Y. Zhang, S.Q. Liu, Y.M. Tang, and Y.S. Yin, *Effects of nanoparticle clustering and alignment on thermal conductivities of Fe3O4 aqueous nanofluids.* Applied Physics Letters, 2006. **89**(2).

70. Xie, H.Q., J.C. Wang, T.G. Xi, Y. Liu, and F. Ai, *Thermal conductivity of suspension containing SiC particles.* Journal of Materials Science Letters, 2002. **21**(3): p. 193-195.

71. Xuan, Y.M. and Q. Li, *Heat transfer enhancement of nanofluids.* International Journal of Heat and Fluid Flow, 2000. **21**(1): p. 58-64.

72. Liu, M.S., M.C.C. Lin, C.Y. Tsai, and C.C. Wang, *Enhancement of thermal conductivity with Cu for nanofluids using chemical reduction method.* International Journal of Heat and Mass Transfer, 2006. **49**(17-18): p. 3028-3033.

73. Jana, S., A. Salehi-Khojin, and W.H. Zhong, *Enhancement of fluid thermal conductivity by the addition of single and hybrid nano-additives.* Thermochimica Acta, 2007. **462**(1-2): p. 45-55.

74. Eastman, J.A., S.U.S. Choi, S. Li, W. Yu, and L.J. Thompson, *Anomalously increased effective thermal conductivities of ethylene glycol-based nanofluids containing copper nanoparticles.* Applied Physics Letters, 2001. **78**(6): p. 718-720.

75. Assael, M.J., I.N. Metaxa, K. Kakosimos, and D. Constantinou, *Thermal conductivity of nanofluids - Experimental and theoretical.* International Journal of Thermophysics, 2006. **27**(4): p. 999-1017.

76. Jwo, C.S. and T.P. Teng, *Experimental study on thermal properties of brines containing nanoparticles.* Reviews on Advanced Materials Science, 2005. **10**(1): p. 79-83.

77. Lee, C.H., S.W. Kang, and S.H. Kim, *Effects of nano-sized ag particles on heat transfer of nanofluids.* Journal of Industrial and Engineering Chemistry, 2005. **11**(1): p. 152-158.

78. Putnam, S.A., D.G. Cahill, P.V. Braun, Z.B. Ge, and R.G. Shimmin, *Thermal conductivity of nanoparticle suspensions.* Journal of Applied Physics, 2006. **99**(8).

79. Hong, T.K., H.S. Yang, and C.J. Choi, *Study of the enhanced thermal conductivity of Fe nanofluids.* Journal of Applied Physics, 2005. **97**(6).

80. Hong, K.S., T.K. Hong, and H.S. Yang, *Thermal conductivity of Fe nanofluids depending on the cluster size of nanoparticles.* Applied Physics Letters, 2006. **88**(3).

81. Manna, I., M. Chopkar, and P.K. Das, *Nanofluid - A new concept in heat transfer and thermal management.* Transactions of the Indian Institute of Metals, 2005. **58**(6): p. 1045-1055.

82. Chopkar, M., S. Kumar, D.R. Bhandari, P.K. Das, and I. Manna, *Development and characterization of Al2Cu and Ag2Al nanoparticle dispersed water and ethylene glycol based nanofluid.* Materials Science and Engineering B-Solid State Materials for Advanced Technology, 2007. **139**(2-3): p. 141-148.

83. Ceylan, A., K. Jastrzembski, and S.I. Shah, *Enhanced solubility Ag-Cu nanoparticles and their thermal transport properties.* Metallurgical and Materials Transactions a-Physical Metallurgy and Materials Science, 2006. **37A**(7): p. 2033-2038.

84. Wen, D.S. and Y.L. Ding, *Effective thermal conductivity of aqueous suspensions of carbon nanotubes (carbon nanotubes nanofluids).* Journal of Thermophysics and Heat Transfer, 2004. **18**(4): p. 481-485.

85. Assael, M.J., C.F. Chen, I. Metaxa, and W.A. Wakeham, *Thermal conductivity of suspensions of carbon nanotubes in water.* International Journal of Thermophysics, 2004. **25**(4): p. 971-985.

86. Assael, M.J., I.N. Metaxa, J. Arvanitidis, D. Christofilos, and C. Lioutas, *Thermal conductivity enhancement in aqueous suspensions of carbon multi-walled and double-walled nanotubes in the presence of two different dispersants.* International Journal of Thermophysics, 2005. **26**(3): p. 647-664.

87. Hong, H.P., J. Wensel, F. Liang, W.E. Billups, and W. Roy, *Heat transfer nanofluids based on carbon nanotubes.* Journal of Thermophysics and Heat Transfer, 2007. **21**(1): p. 234-236.

88. Wright, B., D. Thomas, H. Hong, L. Groven, J. Puszynski, E. Duke, X. Ye, and S. Jin, *Magnetic field enhanced thermal conductivity in heat transfer nanofluids containing Ni coated single wall carbon nanotubes.* Applied Physics Letters, 2007. **91**(17): p. 3.

89. Wensel, J., B. Wright, D. Thomas, W. Douglas, B. Mannhalter, W. Cross, H.P. Hong, J. Kellar, P. Smith, and W. Roy, *Enhanced thermal conductivity by aggregation in heat transfer nanofluids containing metal oxide nanoparticles and carbon nanotubes.* Applied Physics Letters, 2008. **92**(2): p. 3.

90. Liu, M.S., M.C.C. Lin, I.T. Huang, and C.C. Wang, *Enhancement of thermal conductivity with carbon nanotube for nanofluids.* International Communications in Heat and Mass Transfer, 2005. **32**(9): p. 1202-1210.

91. Casquillas, G.V., M. Le Berre, C. Peroz, Y. Chen, and J.J. Greffet, *Microlitre hot strip devices for thermal characterization of nanofluids.* Microelectronic Engineering, 2007. **84**(5-8): p. 1194-1197.

92. Marquis, F.D.S. and L.P.F. Chibante, *Improving the heat transfer of nanofluids and nanolubricants with carbon nanotubes.* JOM, 2005. **57**(12): p. 32-43.

93. Yang, Y., E.A. Grulke, Z.G. Zhang, and G.F. Wu, *Thermal and rheological properties of carbon nanotube-in-oil dispersions.* Journal of Applied Physics, 2006. **99**(11).

94. Zhu, H.T., C.Y. Zhang, Y.M. Tang, J.X. Wang, B. Ren, and Y.S. Yin, *Preparation and thermal conductivity of suspensions of graphite nanoparticles.* Carbon, 2007. **45**(1): p. 226-228.

95. Hong, H.P., B. Wright, J. Wensel, S.H. Jin, X.R. Ye, and W. Roy, *Enhanced thermal conductivity by the magnetic field in heat transfer nanofluids containing carbon nanotube.* Synthetic Metals, 2007. **157**(10-12): p. 437-440.

96. Wakeham, W.A., A. Nagashima, and J.V. Sengers, eds. *Measurement of the Transport Properties of Fluids*. Experimental Thermodynamics. 1991, Blackwell Scientific Publications: Oxford. 459.

97. Murshed, S.M.S., K.C. Leong, and C. Yang, *Determination of the effective thermal diffusivity of nanofluids by the double hot-wire technique.* Journal of Physics D-Applied Physics, 2006. **39**(24): p. 5316-5322.

98. Carslaw, H.S. and J.C. Jaeger, *Conduction of Heat in Solids*. 2nd ed. 1959, Oxford: Clarendon Press. 510.

99. Degroot, J.J., J. Kestin, and Sookiazi.H, *INSTRUMENT TO MEASURE THERMAL-CONDUCTIVITY OF GASES.* Physica, 1974. **75**(3): p. 454-482.

100. Healy, J.J., J.J. de Groot, and J. Kestin, *THEORY OF TRANSIENT HOT-WIRE METHOD FOR MEASURING THERMAL-CONDUCTIVITY.* Physica B & C, 1976. **82**(2): p. 392-408.

101. Nagasaka, Y. and A. Nagashima, *ABSOLUTE MEASUREMENT OF THE THERMAL-CONDUCTIVITY OF ELECTRICALLY CONDUCTING LIQUIDS BY*

THE TRANSIENT HOT-WIRE METHOD. Journal of Physics E-Scientific Instruments, 1981. **14**(12): p. 1435-1440.

102. Hoshi, M., T. Omotani, and A. Nagashima, *TRANSIENT METHOD TO MEASURE THE THERMAL-CONDUCTIVITY OF HIGH-TEMPERATURE MELTS USING A LIQUID-METAL PROBE.* Review of Scientific Instruments, 1981. **52**(5): p. 755-758.

103. Diguilio, R.M. and A.S. Teja, *THERMAL-CONDUCTIVITY OF AQUEOUS SALT-SOLUTIONS AT HIGH-TEMPERATURES AND HIGH-CONCENTRATIONS.* Industrial & Engineering Chemistry Research, 1992. **31**(4): p. 1081-1085.

104. Bleazard, J.G. and A.S. Teja, *Thermal-Conductivity of Electrically Conducting Liquids by the Transient Hot-Wire Method.* Journal of Chemical and Engineering Data, 1995. **40**(4): p. 732-737.

105. Bleazard, J.G., T.F. Sun, R.D. Johnson, R.M. DiGuilio, and A.S. Teja, *The transport properties of seven alkanediols.* Fluid Phase Equilibria, 1996. **117**(1-2): p. 386-393.

106. Bleazard, J.G., T.F. Sun, and A.S. Teja, *The thermal conductivity and viscosity of acetic acid-water mixtures.* International Journal of Thermophysics, 1996. **17**(1): p. 111-125.

107. Sun, T.F. and A.S. Teja, *Density, viscosity and thermal conductivity of aqueous solutions of propylene glycol, dipropylene glycol, and tripropylene glycol between 290 K and 460 K.* Journal of Chemical and Engineering Data, 2004. **49**(5): p. 1311-1317.

108. Sun, T.F. and A.S. Teja, *Density, viscosity, and thermal conductivity of aqueous ethylene, diethylene, and triethylene glycol mixtures between 290 K and 450 K.* Journal of Chemical and Engineering Data, 2003. **48**(1): p. 198-202.

109. Sun, T. and A.S. Teja, *Density, viscosity, and thermal conductivity of aqueous benzoic acid mixtures between 375 K and 465 K.* Journal of Chemical and Engineering Data, 2004. **49**(6): p. 1843-1846.

110. Diguilio, R.M. and A.S. Teja, *THE THERMAL-CONDUCTIVITY OF THE MOLTEN NANO3-KNO3 EUTECTIC BETWEEN 525-K AND 590-K.* International Journal of Thermophysics, 1992. **13**(4): p. 575-592.

111. Omotani, T., Y. Nagasaka, and A. Nagashima, *Measurement of the thermal conductivity of KNO_3-$NaNO_3$ mixtures with liquid metal in a capillary probe.* International Journal of Thermophysics, 1982. **3**(1): p. 17-26.

112. Nieto de Castro, C.A., S.F.Y. Li, C. Maitland, and W.A. Wakeham, *Thermal conductivity of toluene in the temperature range 35-90 ^oC at pressures up to 600 MPa.* International Journal of Thermophysics, 1983. **4**(4): p. 311-327.

113. de Groot, J.J., J. Kestin, and Sookiazi.H, *INSTRUMENT TO MEASURE THERMAL-CONDUCTIVITY OF GASES.* Physica, 1974. **75**(3): p. 454-482.

114. Marsh, K.N., ed. *Recommended Reference Materials for the Realization of Physicochemical Properties*. 1987, Blackwell Scientific Publications: Boston. 500.

115. DIPPR, *DIPPR Project 801*. 2007, Design Institute for Physical Properties / AIChE.

116. Drelich, J., J.S. Laskowski, and K.L. Mittal, eds. *Apparent and Microscopic Contact Angles*. 2000, Utrecht: Boston. 524.

117. Kosmulski, M., *Chemical Properties and Material Surfaces*. 2001, New York: Marcel Dekker. 753.

118. Maxwell, J.C., *A Treatise on Electricity and Magnetism*. 3rd ed. Vol. II. 1892, London: Oxford University Press.

119. Carson, J.K., *Review of effective thermal conductivity models for foods.* International Journal of Refrigeration-Revue Internationale Du Froid, 2006. **29**(6): p. 958-967.

120. Tsotsas, E. and H. Martin, *THERMAL-CONDUCTIVITY OF PACKED-BEDS - A REVIEW.* Chemical Engineering and Processing, 1987. **22**(1): p. 19-37.

121. Progelhof, R.C., J.L. Throne, and R.R. Ruetsch, *METHODS FOR PREDICTING THERMAL-CONDUCTIVITY OF COMPOSITE SYSTEMS.* Polymer Engineering and Science, 1976. **16**(9): p. 615-625.

122. Rayleigh, L., *On the Influence of Obstacles arranged in Rectangular Order upon the Properties of a Medium.* Philosophical Magazine and Journal of Science, 1892. **34**: p. 481-502.

123. Hamilton, R.L. and O.K. Crosser, *Thermal Conductivity of Heterogeneous 2-Component Systems.* Industrial & Engineering Chemistry Fundamentals, 1962. **1**(3): p. 187.

124. Jeffrey, D.J., *CONDUCTION THROUGH A RANDOM SUSPENSION OF SPHERES.* Proceedings of the Royal Society of London Series a-Mathematical Physical and Engineering Sciences, 1973. **335**(1602): p. 355-367.

125. Bruggeman, D.A.G., *Calculation of various physics constants in heterogenous substances I Dielectricity constants and conductivity of mixed bodies from isotropic substances.* Annalen Der Physik, 1935. **24**(7): p. 636-664.

126. Landauer, R., *THE ELECTRICAL RESISTANCE OF BINARY METALLIC MIXTURES.* Journal of Applied Physics, 1952. **23**(7): p. 779-784.

127. Keey, R.B., *Drying of Loose and Particulate Materials*. 1992, New York: Hemisphere Publishing Corporation. 504.

128. Krischer, O., *Die wissenschaftlichen Grundlagen der Trocknungstechnik (The Scientific Fundamentals of Drying Technology)*. 2nd ed. 1963, Berlin: Springer-Verlag.

129. Tsao, G.T.N., *THERMAL CONDUCTIVITY OF 2-PHASE MATERIALS.* Industrial and Engineering Chemistry, 1961. **53**(5): p. 395-397.

130. Hashin, Z. and S. Shtrikman, *A Variational Approach to the Theory of the Effective Magnetic Permeability of Multiphase Materials.* Journal of Applied Physics, 1962. **33**(10): p. 3125.

131. Jang, S.P. and S.U.S. Choi, *Role of Brownian motion in the enhanced thermal conductivity of nanofluids.* Applied Physics Letters, 2004. **84**(21): p. 4316-4318.

132. Kumar, D.H., H.E. Patel, V.R.R. Kumar, T. Sundararajan, T. Pradeep, and S.K. Das, *Model for heat conduction in nanofluids.* Physical Review Letters, 2004. **93**(14): p. 144301.

133. Patel, H.E., T. Sundararajan, T. Pradeep, A. Dasgupta, N. Dasgupta, and S.K. Das, *A micro-convection model for thermal conductivity of nanofluids.* Pramana-Journal of Physics, 2005. **65**(5): p. 863-869.

134. Patel, H.E., T. Sundararajan, and S.K. Das, *A cell model approach for thermal conductivity of nanofluids.* Journal of Nanoparticle Research, 2008. **10**(1): p. 87-97.

135. Koo, J. and C. Kleinstreuer, *A new thermal conductivity model for nanofluids.* Journal of Nanoparticle Research, 2004. **6**(6): p. 577-588.

136. Prasher, R., P. Bhattacharya, and P.E. Phelan, *Thermal conductivity of nanoscale colloidal solutions (nanofluids).* Physical Review Letters, 2005. **94**(2): p. 025901.

137. Ren, Y., H. Xie, and A. Cai, *Effective thermal conductivity of nanofluids containing spherical nanoparticles.* Journal of Physics D-Applied Physics, 2005. **38**(21): p. 3958-3961.

138. Xuan, Y.M., Q. Li, X. Zhang, and M. Fujii, *Stochastic thermal transport of nanoparticle suspensions.* Journal of Applied Physics, 2006. **100**(4).

139. Prakash, M. and E.P. Giannelis, *Mechanism of heat transport in nanofluids.* Journal of Computer-Aided Materials Design, 2007. **14**(1): p. 109-117.

140. Yu, W. and S.U.S. Choi, *The role of interfacial layers in the enhanced thermal conductivity of nanofluids: A renovated Maxwell model.* Journal of Nanoparticle Research, 2003. **5**(1-2): p. 167-171.

141. Yu, W. and S.U.S. Choi, *The role of interfacial layers in the enhanced thermal conductivity of nanofluids: A renovated Hamilton-Crosser model.* Journal of Nanoparticle Research, 2004. **6**(4): p. 355-361.

142. Xie, H.Q., M. Fujii, and X. Zhang, *Effect of interfacial nanolayer on the effective thermal conductivity of nanoparticle-fluid mixture.* International Journal of Heat and Mass Transfer, 2005. **48**(14): p. 2926-2932.

143. Xue, Q.Z., *Model for thermal conductivity of carbon nanotube-based composites.* Physica B-Condensed Matter, 2005. **368**(1-4): p. 302-307.

144. Leong, K.C., C. Yang, and S.M.S. Murshed, *A model for the thermal conductivity of nanofluids - the effect of interfacial layer.* Journal of Nanoparticle Research, 2006. **8**(2): p. 245-254.

145. Feng, Y.J., B.M. Yu, P. Xu, and M.Q. Zou, *The effective thermal conductivity of nanofluids based on the nanolayer and the aggregation of nanoparticles.* Journal of Physics D-Applied Physics, 2007. **40**(10): p. 3164-3171.

146. Lee, D., *Thermophysical properties of interfacial layer in nanofluids.* Langmuir, 2007. **23**(11): p. 6011-6018.

147. Evans, W., J. Fish, and P. Keblinski, *Thermal conductivity of ordered molecular water.* Journal of Chemical Physics, 2007. **126**(15).

148. Wang, B.X., L.P. Zhou, and X.F. Peng, *A fractal model for predicting the effective thermal conductivity of liquid with suspension of nanoparticles.* International Journal of Heat and Mass Transfer, 2003. **46**(14): p. 2665-2672.

149. Xuan, Y.M., Q. Li, and W.F. Hu, *Aggregation structure and thermal conductivity of nanofluids.* Aiche Journal, 2003. **49**(4): p. 1038-1043.

150. Prasher, R., W. Evans, P. Meakin, J. Fish, P. Phelan, and P. Keblinski, *Effect of aggregation on thermal conduction in colloidal nanofluids.* Applied Physics Letters, 2006. **89**(14): p. 143119.

151. Kumar, S. and J.Y. Murthy, *A numerical technique for computing effective thermal conductivity of fluid-particle mixtures.* Numerical Heat Transfer Part B-Fundamentals, 2005. **47**(6): p. 555-572.

152. Gao, L. and X.F. Zhou, *Differential effective medium theory for thermal conductivity in nanofluids.* Physics Letters A, 2006. **348**(3-6): p. 355-360.

153. Eapen, J., J. Li, and S. Yip, *Beyond the Maxwell limit: Thermal conduction in nanofluids with percolating fluid structures.* Physical Review E, 2007. **76**(6): p. 4.

154. Swartz, E.T. and R.O. Pohl, *Thermal boundary resistance.* Reviews of Modern Physics, 1989. **61**(3): p. 605-668.

155. Nan, C.W., R. Birringer, D.R. Clarke, and H. Gleiter, *Effective thermal conductivity of particulate composites with interfacial thermal resistance.* Journal of Applied Physics, 1997. **81**(10): p. 6692-6699.

156. Huxtable, S.T., D.G. Cahill, S. Shenogin, L.P. Xue, R. Ozisik, P. Barone, M. Usrey, M.S. Strano, G. Siddons, M. Shim, and P. Keblinski, *Interfacial heat flow in carbon nanotube suspensions.* Nature Materials, 2003. **2**(11): p. 731-734.

157. Wilson, O.M., X.Y. Hu, D.G. Cahill, and P.V. Braun, *Colloidal metal particles as probes of nanoscale thermal transport in fluids.* Physical Review B, 2002. **66**(22): p. 6.

VITA

MICHAEL P. BECK

Michael P. Beck was born in Evanston, Illinois on October 27, 1975 to Donald P. Beck and Linda S. Beck. He grew up with three brothers and attended Beloit Catholic High School in Beloit, Wisconsin. He received his Bachelor of Science degrees in Chemical Engineering and in Biochemistry from the University of Wisconsin in Madison in 1999. From 1999 until 2002, he worked for Abbott Laboratories in North Chicago, Illinois in the Corporate Engineering Division and the Abbott Diagnostics Division before coming to Georgia Tech in 2002 to pursue a doctorate in chemical engineering. On June 4, 2005, he married Kanrakot (Nan) Thamanavat in Atlanta, GA. Following his graduation from Georgia Tech, he will work at Nalco Company in Naperville, IL as a senior engineer.